Equilibrium and transport properties of constrained systems

Debasish Chaudhuri

S. N. Bose National Centre for Basic Sciences

Block - JD, Sector-III, Salt Lake

Kolkata - 700 098, India

May 2006

CERTIFICATE FROM THE SUPERVISOR

This is to certify that the thesis entitled "**Equilibrium and transport properties of constrained systems**" submitted by **Sri Debasish Chaudhuri**, who got his name registered on **11th May, 2004** for the award of **Ph.D.(Science) degree of Jadavpur University** , is absolutely based upon his own work under the supervision of **Dr. Surajit Sengupta** and that neither this thesis nor any part of its has been submitted for any degree / diploma or any other academic award anywhere before.

Date:

Surajit Sengupta
Reader
S. N. Bose National Centre for Basic Sciences
Block-JD, Sector-III, Salt Lake, Kolkata - 700098, India

Acknowlegements

This thesis is a result of almost five years of work. During this period I have been accompanied and supported by many people. It is my pleasure that I have now the opportunity to express my gratitude to all of them.

First and foremost, I would like to thank Dr. Surajit Sengupta, my thesis supervisor, for being a continuous source of support, enthusiasm, many new ideas, constructive criticisms, for giving me independence to pursue research on the few ideas that ever came across my mind. His simplicity, knowledge, open mind, simple and critical outlook towards science always remain an inspiration. It helped me a lot, that I could always discuss with him on any topic without any hesitation. I admire his ability of concentrating in his work even in very disturbing situations.

It is a pleasure to thank Dr. Abhishek Dhar, Raman Research Institute, Bangalore. I found his support at a time I needed it most. His interests and clear understanding in a wide spectrum of physics, his simple and clean reasonings and his dedication in research has always been an inspiration. I gained a lot from the opportunity of working with him, his teaching, his criticism, his friendship and many many discussions that I had with him.

I thank Dr. Madan Rao and Dr. Yashodhan Hatwalne of Raman Research Institute, Bangalore, for introducing me to the fascinating field of soft condensed matter physics. Madan remains a source of inspiration with his enthusiasm, non- stop flow of new ideas, knowledge, critical outlook, his views towards science, many useful discussions and all his encouragements.

Two of my teachers in Kalyani University, Prof. Padmanabha Dasgupta and Dr. Somenath Chakraborty inspired with their teaching and encouragements. I thank Dr. Srikanth Sastry (Jawaharlal Nehru Centre for Advanced Scientific Research, Bangalore) from whom I have learnt computational techniques, that remains very useful in my research. A very special thanks to Dr. P. A. Sreeram for all the time that he gave to maintain a very good computational facility at S. N. Bose National Centre for Basic Sciences (SNBNCBS). I thank Sreeram also for a lot of useful discussions.

I would like to acknowledge helpful discussions with V. B. Shenoy (Indian Institute of Science, Bangalore), Y. Kantor (Tel Aviv University, Israel), M. Barma (Tata Institute of Fundamental Research, Mumbai), E. Frey (Ludwig- Maximilians- Universität München, Germany) and A. M. Jayannavar (Institute of Physics, Bhubaneswar). I also thank Raman Research Institute, Bangalore, where a significant part of my work on semi- flexible polymers and heat conduction was

List of Publications

Publications: in refereed journals

[1] "Heat conduction in confined solid strip: response to external strain", **Debasish Chaud-huri** and Abhishek Dhar, communicated to *Physical Review E* (cond-mat/0601310).

[2] "Electrical transport in deformed nanostrips: electrical signature of reversible mechanical failure", Soumendu Datta, **Debasish Chaudhuri**, Tanusri Saha-Dasgupta, Surajit Sengupta, *EuroPhysics Letters* **73**, 765 (2006); (cond-mat/0511457); [not included in this thesis].

[3] "Direct test of defect mediated laser induced melting theory for two dimensional solids", **Debasish Chaudhuri** and Surajit Sengupta, *Physical Review E* **73**, 011507 (2006); (cond-mat/0508514).

[4] "Constrained Deformation of a Confined Solid: Anomalous Failure by Nucleation of Smectic Bands", **Debasish Chaudhuri** and Surajit Sengupta, *Physical Review Letters*, **93**, 115702 (2004); (cond-mat/0401121).

[5] "A numerical renormalization group study of laser-induced freezing", **Debasish Chaudhuri** and Surajit Sengupta, *EuroPhysics Letters*, **67**, 814- 819 (2004); also see "*Erratum* A numerical renormalization group study of laser-induced freezing", **Debasish Chaudhuri** and Surajit Sengupta, *EuroPhysics Letters*, **68**, 160 (2004); (cond-mat/0403319).

[6] "Triple Minima in the Free Energy of Semiflexible Polymers", Abhishek Dhar and **Debasish Chaudhuri**, *Physical Review Letters*, **89**, 065502 (2002); (cond-mat/0203482).

Publications: in proceedings

[1] "Mechanical Failure of a Small and Confined Solid", **Debasish Chaudhuri** and Surajit Sengupta, *Indian Journal of Physics*, **79**, 941-945 (2005); (cond-mat/0508513).

[2] "Induced interfaces at nano-scales: structure and dynamics", Abhishek Chaudhuri, **Debasish Chaudhuri** and Surajit Sengupta, *International Journal of Nanoscience*, 4, 995 (2005).

[3] "Elastic properties, structures and phase transitions in model colloids", P. Nielaba, K. Binder, **D. Chaudhuri**, K. Franzrahe, P. Henseler, M. Lohrer, A. Ricci, S. Sengupta, and W.Strepp, *J. Phys.: Condens. Matter*, **16**, S4115- S4136 (2004).

Abstract

Systems under external confinement and constraints often show interesting properties. In this thesis, we study some systems under external confinement. We begin by finding out the probability distribution of end-to-end separation of a semiflexible polymer within the Worm Like Chain model using Monte- Carlo simulations (MC). In the constant extension ensemble, where the two ends of the polymer are placed in stiff potential traps created by laser tweezers, the probability distribution shows triple maxima indicating a non-monotonic force- extension in some intermediate regime of polymer stiffness. Whereas this feature is absent in constant force ensemble. Our study on this system revealed the ensemble dependence of physical properties for finite sized systems.Then, we fix the orientations at the ends of a polymer and find that the orientation, as well as the ensemble, control the statistics and mechanical properties of a semi- flexible polymer. We present an exact theory to calculate the partition functions in both the Helmholtz and Gibbs ensembles and this theory takes care of the orientations at the ends of the polymer. We find multimodality in Helmholtz ensemble as a generic signature of semi- flexibility.

Secondly, we study Laser Induced Freezing (LIF) where a colloidal liquid is constrained by an external laser field periodic in one direction. Using a Kosterlitz- Thouless type renormalization group calculation and a restricted MC simulation we calculate the phase diagrams for model colloids interacting via Hard Disk, Soft Disk and DLVO potentials. The phase diagrams match exactly with the corresponding phase diagrams simulated by other groups, thereby proving that LIF is indeed a dislocation mediated transition.

Lastly, we study the phase behaviors and failure mechanism of a two- dimensional solid confined within a hard wall channel using MC and Molecular dynamics simulations. This system fails by nucleation of smectic phase within the solid. We have shown that thinner strips are stronger! The failure is ductile showing reversible plasticity. Density functional arguments can capture some of these features qualitatively. We have used a mean field calculation to find out the phase diagram of this system in density- channel width plane. We show that fluctuations in quasi one dimension lead to very strange behavior, namely a system that looks solid considering its structure factor shows vanishingly small shear modulus like a liquid! We study the impact of this reversible failure on transport properties. We find that the heat current in response to tensile strain varies differently depending on whether the strain is imposed in the confining direction or the other. We propose a simple free volume calculation that captures the strain response of heat current, exactly, within small strains.

Contents

1 Introduction

Every year during the month of March a family of ragged gypsies would set up their tents near the village, and with a great uproar of pipes and kettledrums they would display new innovations.   *– G. G. Márquez*

Traditionally, the science of thermodynamics and statistical mechanics were concerned with determining the properties of materials in the so-called *thermodynamic limit* [1]. In this limit, relevant for most materials and experimental situations, the number of particles $N \rightarrow \infty$ and all statistical mechanical ensembles e.g. Helmholtz (constant number, volume, strain, etc.) and Gibbs (constant chemical potential, pressure, stress, etc.) are rigorously equivalent. Also, in this limit, for most systems with short ranged interactions and compact shape, the nature of the boundaries and boundary fields have no impact on bulk properties.

Historically, the need for examining systems far removed from the thermodynamic limit arose first with the advent of computers and computer simulation techniques in the early 1950s and 60s. Early computers were not very powerful and the largest system sizes that could be handled were small. The need for extrapolating results obtained from small system sizes used in computer simulations for predicting phase boundaries, susceptibilities, critical exponents etc. as measured in the laboratory spawned the discipline of finite size scaling [2–4]. The early works of Binder [5, 6] and Fisher[7–10] are significant in this context. The emerging ideas of the renormalization group [11, 12] had a direct impact on this endeavor and aided immensely our understanding of the thermodynamics of small systems.

Simultaneously, technological breakthroughs in semiconductors, magnetic recording devices and experiments on surfaces, thin films and adsorbtion pointed out the importance of boundaries and surfaces in determining materials properties [13, 14]. Surface phases, wetting, the physics of interfaces and surface phase transformations became topics of intense study using computer simulations, renormalization group theory and experiments. In the later part of the last century rapid advances in primarily two areas of science and technology were responsible for a further spurt of activity in trying to understand the role of finite size in determining the properties of materials. Firstly, new techniques like the use of lasers in manipulating objects and novel microscopic techniques meant that one could measure properties of systems down to the size of a large molecule e.g. biologically important polymers like proteins and DNA [15–17]. Rapid

advances in biotechnology made it possible for us to ultimately measure forces involved, say, in the replication of DNA or in protein synthesis [18, 19]. Nanotechnology on the other hand [20], using techniques like laser trapping, atomic force and scanning tunneling microscopy could finally make the study of finite systems useful and imperative for its own sake, rather than a precursor to taking the thermodynamic limit.

It is this general context which provides the backdrop of this thesis. In this thesis we have focussed on a number of such systems which are either "small" in the sense of being far from the thermodynamic limit and/or are acted upon by external fields which produce severe constraints that leads to significant change in their behaviour which may be strongly ensemble dependent. We study their statistical and mechanical properties, phase behaviors etc. We also study transport properties of one such system as it undergoes structural transformations that are controlled by external confinement and strains. The structure of this thesis is as follows.

In the next two chapters we study the properties of a semiflexible polymer. We work within a coarse grained model – the worm like chain model – of such a polymer. This model has been successful in predicting mechanical properties obtained from single molecule experiments on real biological polymers like, DNA, microtubules, actin filaments etc. In chapter-2, we show that in the Helmholtz ensemble these polymers can show a non- monotonic force versus extension which is an impossibility if the experiment on this finite chain is made in the Gibbs ensemble or in the thermodynamic limit. This behavior is obtained in a certain range of stiffness of a semiflexible polymer and gives a qualitative signature of semiflexibility vis-a-vis a flexible polymer. In this chapter the non- monotonic force- extension curve was obtained for a polymer whose boundaries were free to rotate. In chapter-3, we present an exact theory to calculate the properties of a semi- flexible polymer for all possible bending rigidities taking into account the orientations of ends of a polymer. Using this theory and simulations we establish that imposing constraints in boundary orientations vary the statistics and mechanical properties of the polymer. Thus in these two chapters we establish that for semi- flexible polymers, both ensembles and boundary orientations leave important impact on the system properties.

In chapter-3, we study the phenomenon of laser induced freezing and reentrant melting. This comes about due to constraining a two dimensional system by imposing an external potential that is constant in one direction and periodically modulated in the other. We take the simplest case where the periodicity of the external potential is commensurate with spacings between the lattice planes of the system. Thus the external constraint permeates the whole system. With change in the strength of this potential phase transitions occur between a modulated liquid and a locked floating solid phase. We use a constrained Monte- Carlo simulation to obtain input parameters which are used in a numerical renormalization group scheme to test a recently proposed defect mediated melting theory for this system.

In the following chapter, we study the impact of a different kind of external potential on a two

dimensional solid. We confine the solid in a quasi one dimensional hard channel such that, in the direction of confinement the solid is only a few atomic layers thick and study its mechanical and phase behavior. Study of this system is important due to the recent interest in nano- technology. This confinement is a boundary effect and drastically changes the properties of the solid and introduces many layering transitions, which are absent in the thermodynamic limit. We also study the anomalous and reversible failure of this system under tensile strain. We present mean field calculations to substantiate our simulation data. We end this chapter with a discussion on enhanced flcutuations in this system due to the reduced dimensionality.

In chapter-6, we find out the impact of reversible failure on the heat transport properties of this system. We use molecular dynamics simulation to calculate the change in heat current as the system undergoes tensile strain. The change in heat current in response to strain imposed in the confining direction is very different from the case when the strain is imposed in the perpendicular direction. We introduce a free volume like theory to calculate the heat current and obtain exact match with simulation results up to small strains.

In summary, in this thesis we have taken up a set of independent problems which are however connected by the theme of finite size effects and the effect of boundaries and constraints on the determination of overall behavior. Each of the chapters in the thesis are fairly self-contained and more or less independent of each other.

2 Nonmonotonic Force-extension in Semi-flexible Polymer

"Things have a life of there own", the gypsy proclaimed with a harsh accent.
"It's simply a matter of waking up their souls". — *G. G. Márquez*

The simplest model for describing semiflexible polymers without self-avoidance is the so called Worm-Like-Chain (WLC) model [21–23]. In this model the polymer is modeled as a continuous curve that can be specified by a $d-$dimensional ($d > 1$) vector $\bar{x}(s)$, s being the distance, measured along the length of the curve, from one fixed end. The energy of the WLC model is just the bending energy due to curvature and is given by

$$\frac{H}{k_B T} = \frac{\kappa}{2} \int_0^L (\frac{\partial \hat{u}(s)}{\partial s})^2 ds, \tag{2.1}$$

where $\hat{u}(s) = \partial \bar{x}/\partial s$ is the tangent vector and satisfies $\hat{u}^2 = 1$. The parameter κ specifies the stiffness of the chain and is related to the persistence length λ defined through $\langle \hat{u}(s).\hat{u}(s') \rangle = e^{-|s-s'|/\lambda}$. It can be shown that $\kappa = (d-1)\lambda/2$.

The thermodynamic properties of such a chain can be obtained from the free energy which can be either the Helmholtz (F) free energy or the Gibbs (G) energy. In the former case one considers a polymer whose ends are kept at a fixed distance r [one end fixed at the origin and the other end at $\vec{r} = (0, ...0, r)$] by an average force $\langle f \rangle = \partial F(r, L)/\partial r$, while in the latter case one fixes the force and the average extension is given by $\langle r \rangle = -\partial G(f, L)/\partial f$. It can be shown that in the thermodynamic limit $L \to \infty$ the two ensembles are equivalent and related by the usual Legendre transform $G = F - fr$. For a system with finite L/λ, the equivalence of the two ensembles is not guaranteed, especially when fluctuations become large. We note that real polymers come with a wide range of values of the parameter $t = L/\lambda$ [e.g. $\lambda \approx 0.1\mu m$ for DNA while $\lambda \approx 1\mu m$ for Actin and their lengths can be varied] and fluctuations in r (or f) can be very large. Then the choice of the ensemble depends on the experimental conditions. Experiments on stretching polymers are usually performed by fixing one end of the polymer and attaching the other end to a bead which is then pulled by various means (magnetic, optical, mechanical, etc.). In such experiments one can either fix the force on the bead and measure the average

polymer extension, or, one could constrain the bead's position and look at the average force on the polymer. In the former case, the Gibbs free energy is relevant while it is the Helmholtz in the second case. This point has been carefully analyzed by Kreuzer and Payne in the context of atomic force microscope experiments [24].

Theoretically, the constant-force ensemble is easier to treat, and infact an exact numerical solution has been obtained [25] (though only for $t >> 1$). In two extreme limits of small force and large force WLC model can be solved to obtain force extension relations. In 3D this relation in the small force limit is $\langle z \rangle / L = 2\lambda f / 3 k_B T$ and in the high force limit is $\langle z \rangle / L = 1 - \sqrt{k_B T / 4\lambda f}$. Data on force-extension experiments on DNA [26] have been explained using this ensemble [25]. The case of constant-extension ensemble turns out to be much harder and no exact solution is available. The $t \to 0$ and $t \to \infty$ cases correspond to the solvable limits of the hard rod and the Gaussian chain. The small and large t cases have been treated analytically by perturbation theory about these two limits [27–29]. Numerical simulations for different values of t have been reported by Wilhelm and Frey [30], who have also obtained series expansions valid in the small t limit. A mean-field treatment has also recently been reported [31].

In this chapter we probe the nature of the transition from the Gaussian to the rigid rod with change of stiffness as shown by the form of the Helmholtz free energy of the WLC model (or equivalently the distribution of end-to-end distance). Extensive simulations are performed in two and three dimensions using the equivalence of the WLC model to a random walk with one-step memory. We find the surprising result that, over a range of values of t, the free energy has three minima. This is verified in a one-dimensional version of the model which is exactly solvable.

We first note that the WLC model describes a particle in $d-$dimensions moving with a constant speed (set to unity) and with a random acceleration. It is thus described by the propagator

$$Z(\vec{x}, \hat{u}, L | \vec{x}', \hat{u}', 0) = \frac{\int_{(\vec{x}', \hat{u}')}^{(\vec{x}, \hat{u})} \mathcal{D}[\vec{x}(s)] e^{-H/k_B T}}{\int \mathcal{D}[\vec{x}(s)] e^{-H/k_B T}} \tag{2.2}$$

where in the numerator only paths $\vec{x}(s)$, satisfying $\vec{x}(0) = \vec{x}', \vec{x}(L) = \vec{x}, \hat{u}(0) = \hat{u}'$ and $\hat{u}(L) = \hat{u}$ are considered. It can be shown that the corresponding probability distribution $W(\vec{x}, \hat{u}, L)$ satisfies the following Fokker-Planck equation [27, 28]:

$$\frac{\partial W}{\partial L} + \hat{u}.\nabla_{\vec{x}} W - \frac{1}{2\kappa} \nabla_{\hat{u}}^2 W = 0 \tag{2.3}$$

where $\nabla_{\hat{u}}^2$ is the diffusion operator on the surface of the unit sphere in $d-$dimensions. The discretized version of this model is the freely rotating chain model (FRC) of semiflexible polymers [21]. In the FRC one considers a polymer with N segments, each of length $b = L/N$. Successive segments are constrained to be at a fixed angle, θ, with each other. The WLC model is obtained, in the limit $\theta, b \to 0$, $N \to \infty$ keeping $\lambda = 2b/\theta^2$ and $L = Nb$ finite. In this chapter we report

FIGURE 2.1: Monte-Carlo data for $p(v,t)$ for the $3-$dimensional WLC for values of $t = 10(\circ), 5, 3.33, 2$ and $1(\nabla)$. The inset is a blowup of curves in the transition region ($t = 4, 3.85, 3.7$) and shows the presence of the two maxima.

the simulation results of this FRC model. In the next chapter we shall see how WLC can also be discretized to a Heisenberg spin model with nearest neighbour coupling.

Here we will consider the situation where the ends are kept at a fixed separation r [with $\vec{x}'$ at the origin and $\vec{x} = \vec{r} = (0, ...0, r)$] but there is no constraint on $\hat{u}$ and $\hat{u}'$ and they are taken as uniformly distributed. Thus we will be interested in the distribution $P(r, L) = \langle \delta(\vec{x} - \vec{r}) \rangle = \int d\hat{u} W(\vec{r}, \hat{u}, L)$: this gives the Helmholtz free energy $F(r, L) = -Log[P(r, L)]$. For the spherically symmetric situation we are considering, $P(r, L)$ is simply related to the radial probability distribution $S(r, L)$ through $S(r, L) = C_d r^{d-1} P(r, L)$, C_d being a constant equal to the area of the $d-$dimensional unit sphere. It may be noted that the WLC Hamiltonian is equivalent to spin $O(d)$ models in one dimension in the limit of the exchange constant $J \rightarrow \infty$ (with $Jb = \kappa$ finite) and all results can be translated into spin language. However, for spin systems, the present free energy is not very relevant since it corresponds to putting unnatural constraints on the magnetization vector.

2.1 Numerical Simulations

The simulations were performed by generating random configurations of the FRC model and computing the distribution of end-to-end distances. To obtain equivalence with the WLC model the appropriate limits were taken. We note that because these simulations do not require equilibration, they are much faster than simulations on equivalent spin models and give better statistics.
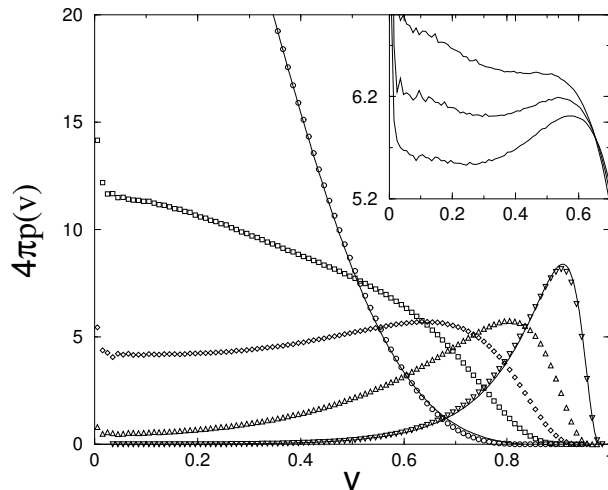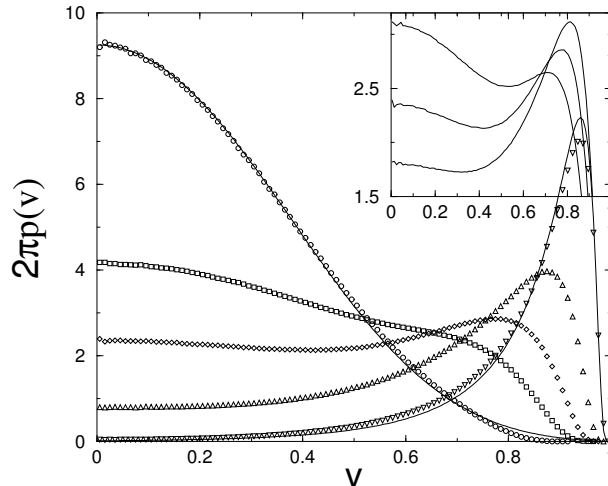
FIGURE 2.2: Monte-Carlo data for $p(v, t)$ for the 2−dimensional WLC for values of $t = 10(\circ), 5, 3.33, 2$ and $1(\nabla)$. The inset is a blowup of curves in the transition region ($t = 4, 3.33, 2.86$) and clearly shows the presence of the two maxima. Note that because of $\pm v$ symmetry, we have plotted data for positive u values only. For the fits at large and small t see text.

The number of configurations generated was around 10^8 for chains of size $N = 10^3$. We verified that increasing N did not change the data significantly. As a check on our numerics we evaluated $\langle r^2 \rangle$ and $\langle r^4 \rangle$. Using Eq. (2.3) and following [32] we can compute these (in all dimensions):

$$\langle r^2 \rangle = \frac{4\kappa L}{d-1} - \frac{8\kappa^2(1 - e^{-\frac{(d-1)L}{2\kappa}})}{(d-1)^2}$$

$$\langle r^4 \rangle = \frac{64\kappa^4(d-1)}{d^3(d+1)^2}e^{-\frac{dL}{\kappa}} - \frac{128\kappa^4(d+5)^2}{(d-1)^4(d+1)^2}e^{-\frac{(d-1)L}{2\kappa}} + \frac{64\kappa^3 L(d^2 - 8d + 7)}{(d-1)^4(d+1)}e^{-\frac{(d-1)L}{2\kappa}}$$

$$+ \frac{64\kappa^4(d^3 + 23d^2 - 7d + 1)}{(d-1)^4 d^3} - \frac{64\kappa^3 L(d^3 + 5d^2 - 7d + 1)}{(d-1)^4 d^2} + \frac{16\kappa^2 L^2(d^3 - 3d + 2)}{d(d-1)^4}. (2.4)$$

Infact it is straightforward to compute all even moments, though it becomes increasingly tedious to get the higher moments. Our numerics agrees with the exact results to around 0.1% for $\langle r^2 \rangle$ and 0.5% for $\langle r^4 \rangle$.

The function P has the scaling form $P(r, L) = \frac{1}{L^d}p(r/L, L/\lambda)$ and we will focus on determining the function $p(v, t)$ [1] In Fig. (2.2) and Fig. (2.1), we show the results of our simulations in two and three dimensions. At large values of t there is a single maximum at $v = r/L = 0$ corresponding to a Gaussian distribution while at small t, the maximum is close to the fully extended value of $v = \pm 1$. The transition is *first-order-like*: as we decrease t, at some critical value, p develops

---

[1]Wilhelm and Frey [30] have looked at the radial distribution $S(r, L)$ which however misses the interesting
   details of the transition. We note that the relevant distribution here is indeed $p(v, t)$ since this gives the
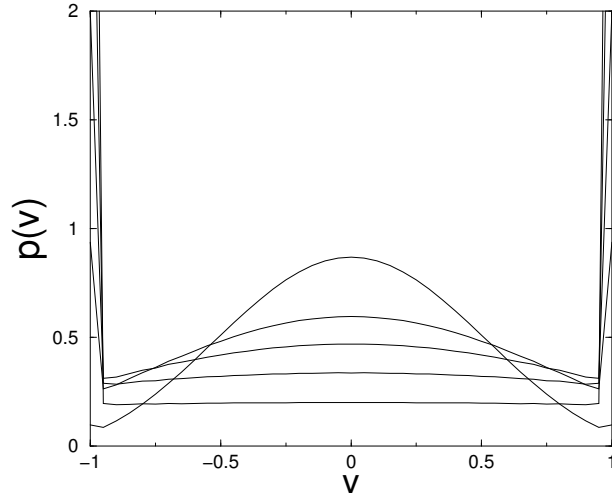   Helmholtz free energy

FIGURE 2.3: The exact distribution $p(v, t)$ of the $1-$dimensional WLC [Eq. (2.6)] for different values of t $(10, 5, 3.33, 2, 1)$. Even for the most stiff chain considered here $(t = 1)$, the distribution has a peak at the centre (in addition to the $\delta-$function peaks at ends) though it looks flat.

two additional maxima at non-zero values of v. Further decreasing t weakens the maximum at $v = 0$ until it finally disappears and there are just two maxima which correspond to the rigid chain.

For the limiting cases of small and large values of t there are analytic results for the distribution function and as can be seen in Fig. (2.2,2.1) our data agrees with them. For large t we find that Daniels approximation [27], which is a perturbation about the Gaussian, fits the data quite well. In the other limit of small t the series solutions provided in [30] fits our data. For intermediate values of t neither of the two forms are able to capture, even qualitatively, the features of the free energy. Specifically, we note that all the analytic theories(perturbative, series expansions and mean-field) predict a second-order-like transition and do not give triple minima of the free energy for any parameter value.

2.2 Exact Calculation in 1D

It is instructive to study the following one-dimensional version of the WLC which shows the same qualitative features (the equivalent spin problem is the Ising model). We consider a N step random walk, with step-size b which, with probability ϵ, reverses its direction of motion and with $1 - \epsilon$, continues to move in the same direction.

The appropriate scaling limit is: $b \to 0$, $\epsilon \to 0$, $N \to \infty$ keeping $L = Nb$, $t = L/\lambda = 2N\epsilon$ finite. Defining $Z_{\pm}(x, L)$ as the probability of the walker to be at x with either positive or

negative velocity, we have the following Fokker-Planck equation:

$$\frac{\partial Z_\pm}{\partial L} = \mp \frac{\partial Z_\pm}{\partial x} \mp \frac{1}{2\lambda}(Z_+ - Z_-) \tag{2.5}$$

This can be solved for $P(x, L) = Z_+ + Z_- = \frac{1}{L}p(x/L, L/\lambda)$. We get

$$p(v, t) = \frac{te^{-t/2}}{4}[\frac{I_1(\frac{t}{2}\sqrt{1 - v^2})}{\sqrt{1 - v^2}} + I_0(\frac{t}{2}\sqrt{1 - v^2})]$$
$$+ \frac{e^{-t/2}}{2}[\delta(v - 1) + \delta(v + 1)], \tag{2.6}$$

where I_0 and I_1 are modified Bessel functions. In Fig. 2.3 we have plotted $p(v, t)$ for different values of stiffness. We find that the probability distribution has three peaks for all values of t. Unlike in 2 and 3 dimensions, the $\delta-$function peaks at $v = \pm 1$ (which corresponds to fully extended chains) persist at all values of stiffness though their weight decays exponentially. Similarly the peak at $v = 0$ is always present.

2.3 Discussion

The most interesting result of this chapter is the triple minima seen in the Helmholtz free energy of the WLC. Physically, this results from the competing effects of entropy, which tries to pull in the polymer and the bending energy, which tries to extend it. This form of the free energy leads to a highly *counterintuitive force-extension curve*, very different from what one obtains from the constant force ensemble or from approximate theories. In Fig. (2.4) we show the force-extension curve for a two dimensional chain with $t = 3.33$. We see that there are two stable positions for which the force is zero. In the constant-force ensemble, it is easy to show that $\partial\langle r\rangle/\partial f = \langle r^2\rangle - \langle r\rangle^2$ and so the force-extension is always monotonic. However, in the constant-extension ensemble, there is no analogous result (*for finite systems*), and consequently monotonicity is not guaranteed.

Most of the recent experiments on stretching DNA have $t \geq 100$. The distribution is then sharply peaked at zero and one expects the equivalence of different ensembles. Experimentally the value of t can be tuned by various means, for example, by changing the length of the polymer or the temperature. Polymer-stretching experiments can thus be performed for intermediate t values. Since we consider the tangent vectors at the polymer-ends to be unconstrained an accurate experimental realization of our set-up would be one in which both ends are attached to beads [see Fig. (2.5)]. The beads are put in optical traps and so are free to rotate (this setup is identical to the one used in refn. [33]). Making the traps stiff corresponds to working in the constant-extension ensemble [24] and one can measure the average force. Our predictions can then be experimentally verified.
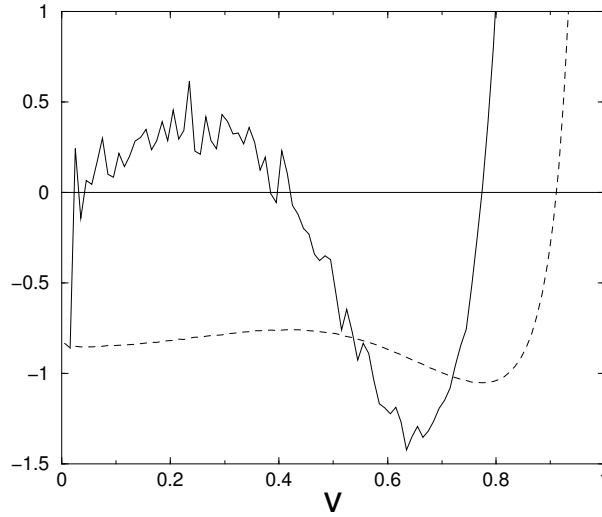
FIGURE 2.4: The free energy (dotted line) and the corresponding force-extension curve (solid line) for a 2−dimensional chain with $t = 3.33$.

We make some estimates on the experimental requirements (for a 3-d polymer with stiffness $t = 3.85$). Assume that at one end, the origin, the trap is so stiff that the bead can only rotate. We make measurements at the other end. The trap-center is placed at $\vec{r}_0 = (0, 0, z_0)$ and the mean bead displacement $\Delta z = \langle (z - z_0) \rangle$ gives the mean force $\langle f \rangle$ on the polymer. We then consider the problem of the polymer in the presence of a trap potential $V = [k_t(x^2 + y^2) + k(z - z_0)^2]/2$. Assume $k_t >> k$ so we can neglect fluctuations in the transverse directions. The distribution of the bead's position in the presence of the potential is given by $Q(\vec{r}) = e^{-\beta[F(\vec{r})+V(\vec{r})]} / \int d^3\vec{r} e^{-\beta[F(\vec{r})+V(\vec{r})]}$. For a stiff trap, we can expand F about $\vec{r} = \vec{r}_0$ and find the average displacement of the bead.

$$F(\vec{r}) = F(\vec{r}_0) + \frac{\partial F}{\partial x_i}|_{\vec{r}_0}(x_i - x_{0_i}) + \frac{1}{2}\frac{\partial^2 F}{\partial x_i \partial x_j}|_{\vec{r}_0}(x_i - x_{0_i})(x_j - x_{0_j}).$$

Due to spherical symmetry $F(\vec{r}) = F(r)$. The operator identity $\frac{\partial}{\partial x_i} = \frac{\partial}{\partial r}\frac{\partial r}{\partial x_i} = \frac{x_i}{r}\frac{\partial}{\partial r}$ leads to $\frac{\partial F}{\partial x_i} = \frac{x_i}{r}\frac{\partial F}{\partial r}$ and

$$\frac{\partial^2 F}{\partial x_i \partial x_j} = \frac{1}{r}\frac{\partial F}{\partial r}\delta_{ij} + \frac{x_i x_j}{r^2}\left(\frac{\partial^2 F}{\partial r^2} - \frac{1}{r}\frac{\partial F}{\partial r}\right)$$

At the point of measurement, $\vec{r}_0 = (0, 0, z_0)$, $\frac{\partial F}{\partial x} = \frac{\partial F}{\partial y} = 0$, $\frac{\partial F}{\partial z} = F_0'$, $\frac{\partial^2 F}{\partial x_i \partial x_j} = 0$ for $i \neq j$, $\frac{\partial^2 F}{\partial x^2} = \frac{\partial^2 F}{\partial y^2} = F_0'/z_0 \equiv G_0$ and $\frac{\partial^2 F}{\partial x^2} = F_0''$. Therefore,

$$F(\vec{r}) + V(\vec{r}) = F_0 + F_0'(z - z_0) + \frac{1}{2}(G_0 + k_t)(x^2 + y^2) + \frac{1}{2}(F_0'' + k)(z - z_0)^2$$
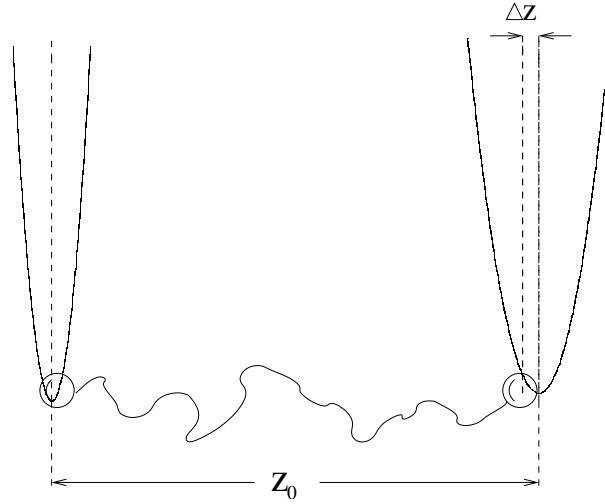
FIGURE 2.5: A schematic of the experimental set-up required to realize the constant-extension ensemble discussed in this chapter. For a stiff trap the average displacement of the bead $\langle \Delta z \rangle$ from the trap center is small and the average force on the polymer is: $\langle f \rangle = -k \langle \Delta z \rangle$.

writing $F(r_0) = F_0$. Then the average displacement can be written as,

$$
\begin{aligned}
\Delta z &= \frac{\int d^3 \vec{r}(z - z_0)e^{-\beta(F+V)}}{\int d^3 \vec{r} e^{-\beta(F+V)}} \\
&= \frac{\int dz(z - z_0)e^{-\beta \frac{1}{2} k'(z - z_0 + F_0'/k')^2}}{\int dz e^{-\beta \frac{1}{2} k'(z - z_0 + F_0'/k')^2}} = -\frac{F_0'}{k'}
\end{aligned}
$$

where $k' = k + F''(z_0)$. In short, we have shown that $\Delta z = \int d^3 \vec{r}(z - z_0)Q(\vec{r}) = -\langle f \rangle / k'$, where $k' = k + F''(z_0) \approx k$ (valid except when $z_0 \approx L$) and $\langle f \rangle = F_0' = F'(z_0)$. The rms fluctuation of the bead about the trap center is given by $z_{rms}^2 = k_B T/k$. Hence we get $\Delta z = -\langle f \rangle z_{rms}^2/(k_B T) = -(\langle f \rangle L/k_B T)(z_{rms}^2/L)$. The scaled force $\langle f \rangle L/(k_B T)$ is of order 0.1. The different minima are separated by distances $\approx 0.2L$, hence to see the effect we need to have $z_{rms}/L \leq 0.1$. Thus finally we find that the typical displacement of the bead Δz is about $0.01 z_{rms}$. This is quite small and means that it is necessary to collect data on the bead position over long periods of time.

As suggested in [30], a more direct way of measuring the Helmholtz free energy would be to attach marker molecules at the ends of the polymer and determine the distribution of end-to-end distances. Fluorescence microscopy as in [15] could be another possible method. It is to be remembered of course that real polymers are well-modeled by the WLC model provided we can neglect monomer-monomer interactions (steric, electrolytic etc.). Thus the experiments would really test the relevance of the WLC model in describing real semiflexible polymers in different stiffness regimes.

2.4 Conclusion

In conclusion we have presented some new and interesting properties of the WLC model and have pointed out that polymer properties are ensemble-dependent. This is a finite size effect. In this chapter we have given one example of qualitative differences in force-extension measurements in different ensembles. Other quantitative differences will occur even in more flexible chains and should be easier to observe experimentally. If the ends of the polymer are free to rotate but the end to end separation is constrained to be at a constant distance, such that the system is in constant extension ensemble, then the free energy of the polymer is shown to have a triple minima structure for some intermediate values of stiffness. In the next chapter we shall investigate the robustness of this triple minima structure as some fixed orientations.

3 Semiflexibile Polymer: Ensemble and End- Orientation

The children would remember for the rest of their lives the august solemnity with which their father, devastated by his prolonged vigil and by the wrath of his imagination, revealed his discovery to them: "The earth is round like an orange".

– G. G. Márquez

In the last chapter we have studied the statistical and mechanical properties of a semiflexible finite polymer with its ends left free to rotate. The bending rigidity coupled with the finite size of the polymer gave rise to inequivalence of ensemble and a very interesting triple minima in free energy in the Helmholtz ensemble and consequently non- monotonic force extension which is absent in Gibbs ensemble. In this chapter, we shall discuss an exact theory that gives results which match exactly with the simulations. Further, we shall go over to different boundary conditions by fixing the orientations at the ends of a polymer and study its impact, which is very non- trivial, on the end to end probability distributions and mechanical properties.

Microtubules and actin polymers constitute the structure of cytoskeleton that gives shape, strength and motility to most of the living cells. They are semiflexible polymers in the sense that their persistence lengths λ are of the order of their chain lengths L such that $t = L/\lambda$ is small and finite. For example, Actin has $\lambda = 16.7 \ \mu m$, $L \sim 30 \ \mu m$[15, 16], Microtubule has $\lambda = 5.2 \ mm$ and statistical contour length $L \sim 10 \ \mu m$[16], double stranded DNA has $\lambda = 50 \ nm$ and contour length $L \sim 300 \ nm$[18]. While it is obvious that in the thermodynamic limit of $t \to \infty$, Gibbs (constant force) and Helmholtz (constant extension) ensemble predict identical properties, the same is not true for real semi- flexible polymers which are far away from this limit. In biological cells actin filaments remain dispersed throughout the cytoplasm with higher concentration in the cortex region, just beneath the plasma membrane. Microtubules, on the other hand, have one end attached to a microtubule- organizing centre, centrosome in animal cells. Another polymer, microtubule- associated proteins (MAP) attach one or both their ends to microtubules to arrange them in microtubule bundles [17]. Thus, end point orientation of polymers play a crucial role in many important phenomena. For instance, gene- regulation in the cell is controlled by DNA-binding proteins, many of which loop DNA with fixed end orientations [34–36]. Thus it becomes important to understand the statistics and the mechanical properties of semi- flexible polymers with different possibilities of end orientations and ensembles.
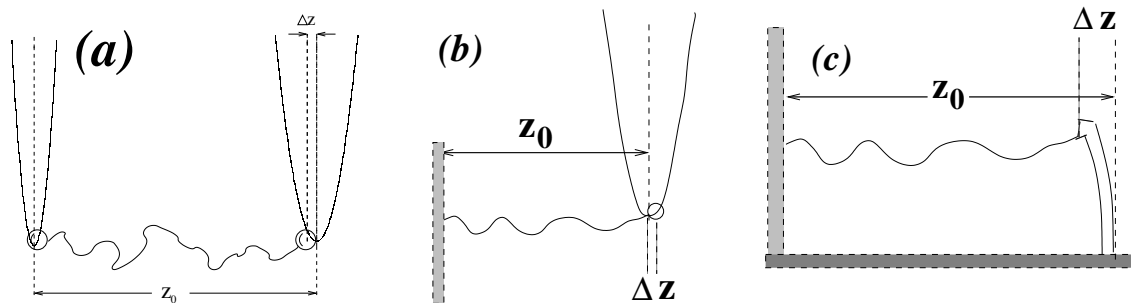
FIGURE 3.1: Three possible experimental set- up for force- extension measurements. (a) left and right ends are held by optical traps, (b) left end is anchored to a surface and the right end is held by optical trap, (c) left end is anchored to a surface and the right end is held by the functionalized tip of an AFM cantilever. z_0 denote the position of the free dielectric bead (for optical trap) or the free cantilever tip in absence of the polymer, Δz denote the displacement associated with the force exerted by the polymer.

During the last decade many single molecule experiments have been performed on semi- flexible polymers[18, 19, 26, 37]. This has been done by using optical tweezers[37], magnetic tweezers[38], AFMs[39] etc. In optical tweezer experiments one end of a polymer is attached to a dielectric bead which is, in turn, trapped by the light intensity profile of a laser tweezer. In this case the dielectric bead is free to rotate within the optical trap. On the other hand, attaching an end of a polymer to a super-paramagnetic bead, one can use magnetic field gradients to trap the polymer using a magnetic tweezer setup. In this case one can rotate the bead while holding it fixed in position by changing the direction of the external magnetic field. In AFM experiments on the other hand one end of polymer is trapped by a functionalized tip of an AFM cantilever. In Fig.3.1 we have shown cartoons of three possible experimental setups. The two distinct procedures which can be followed to measure force- extension are: (a) Both the ends of the polymer are held via laser or magnetic tweezers. (b) One end of the polymer is attached to a substrate such that the position and orientation of this end is fixed while the other end is trapped via laser tweezer or magnetic tweezer or AFM cantilever.

While optical tweezers allow free rotation of dielectric beads within the trap thereby allowing free orientations of the polymer end, magnetic tweezers fix the orientation of the ends and one can study the dependence of polymer properties on orientation of its ends by controlled change of the direction of external magnetic field . In this chapter, we call this fixing of orientation of an end of a polymer as grafting. By changing the trapping potential from stiff to soft trap one can go from Helmholtz to Gibbs ensemble[40]. Before we proceed, let us first elaborate on how to fix the ensemble of a mechanical measurement. In a simplest case we can assume that one

end of the polymer is trapped in a harmonic well,

$$\beta V(z) = C\frac{(z - z_0)^2}{2} \tag{3.1}$$

with $(0, 0, z_0)$ being the position of potential- minimum. The polymer end will undergo continuous thermal motion. One can use a feedback circuit to shift z_0 to force back the fluctuating polymer end to its original position. This will ensure a Helmholtz ensemble. This can also be achieved by taking $C \to \infty$. On the other hand one can use a feedback circuit to fix the force $-C(z - z_0)$ by varying C depending on the position z of the polymer end. This will ensure a Gibbs ensemble. This can also be achieved by taking a vanishingly soft ($C \to 0$) trap to infinitely large distance ($z_0 \to \infty$) such that within the length scale of fluctuation the polymer end feels a constant slope of the parabolic potential. Surely, in experiments, using a feedback circuit is easier to implement a particular ensemble. However, the other procedure is mathematically well defined and one can seek recourse of it to show that the partition function of two ensembles are related by a Laplace transform [41]. This does not depend on the choice of Hamiltonian for the polymer. An exact relation between the two ensembles for worm like chain (WLC) model is shown in Sec.3.1.

From the above discussion on possible experiments, it is clear that there can be three possibilities of boundary conditions in terms of orientation. In an experiment the possibilities are, (a) free end: both the ends of a polymer can remain free to rotate[41, 42], (b) one end grafted: one end may be grafted and the other can take all possible orientations[43] and (c) both ends grafted: the orientations of both the ends are kept fixed. Thus, in experiments, we can have two possible ensembles and three possible boundary conditions. We investigate the probabilitiy distribution, free energy profile and force extension relation for each of these cases in this chapter. We shall see that the properties of a semiflexible polymer depend both on the choice of the ensemble and the boundary condition.

WLC model is a simple coarse grained way to capture bending rigidity of an unstretchable polymer [21, 44] embedded in a thermal environment. Recent single molecule experiments in biological physics [18, 19, 26, 37] renewed interest in this old model of polymer physics. It was successfully employed by Bustamante, Marko, Siggia and Smith [25, 45] to model data from force- extension experiment [26] on double stranded DNA molecules. Mechanical properties of giant muscle protein titin [46, 47], polysaccharide dextrane [39, 47] and single molecule of xanthane [48] were also explained using WLC model. Due to the inextensibility constraint WLC model is hard to tract analytically except for in the two limits of flexible chain ($t \to \infty$) and rigid rod ($t \to 0$), about which perturbative calculations have been done [27–29]. A key quantity that describes statistical property of such polymers is the end-to-end distance distribution. Numerical simulations for different values of t have been reported by Wilhelm and Frey [30], who have also obtained series expansions valid in the small t limit. Mean-field treatments by Thirumalai and his collaborators has also been reported [31, 49]. In an earlier study[42] we have investigated

the free energy profile of a semiflexible polymer whose ends were free to rotate in the constant extension ensemble and in the stiffness regime of $1 \leq t \leq 10$. This has been predicted that a clear qualitative signature of semi- flexibility would be a non- monotonic force extension for stiffnesses around $t = 4$ in Helmholtz (constant end to end separation) ensemble. This comes from bimodality of probability distribution of end to end separation. This non- monotonicity must be absent in Gibbs (constant force) ensemble[42]. Multiple maxima in the probability distribution of end to end separation was due to a competition between entropy, that prefers a maximum near zero separation, and energy, that likes an extended polymer. A lot of theoretical works followed to reproduce and understand the probability density at all stiffnesses including the very interesting bimodality using analytic techniques [41, 50–52]. Recently, Frey and his collaborators studied the interesting multimodality in transverse fluctuations of a grafted polymer using simulations [43] and approximate theory [53, 54]. In a separate study Spakowitz and Wang used Greens function technique that takes into account the orientations of the polymer ends [55]. WLC model has been extended to study double stranded to single stranded DNA transition [56] and to incorporate twist degree of freedom [57–59].

The construction of this chapter is as follows. In Sec.3.1 we present a path integral technique for exact calculation of WLC model for all the three boundary conditions and two ensembles. Then in Sec.3.2 we discuss the different discretized versions of WLC model and the Monte- Carlo (MC) simulation procedures followed in this work. In Sec.4.2 we present all the results obtained from theory and simulations. In this section we present statisticl and mechanical properties for all the possible situations. Then we summarise our results and conclude with some discussions in Sec.5.7.

3.1 Theory

In WLC model the polymer is taken as a continuous curve denoted by a d- dimensional vector $\vec{r}(s)$ where s is a distance measured over the contour of the curve from any end of it. This curve has a bending rigidity and thus the Hamiltonian is given by

$$\beta \mathcal{H} \;\; = \;\; \int_0^L ds \; \frac{\kappa}{2} \left(\frac{\partial \hat{t}(s)}{\partial s} \right)^2 , \tag{3.2}$$

where $\hat{t}(s) = \partial \vec{r}(s)/\partial s$ is the tangent vector and the polymer is inextendible i.e. $\hat{t}^2 = 1$, β is the inverse temperature. The bending rigidity κ is related to persistence length λ via $\kappa = (d-1)\lambda/2$. Persistence length is a measure of the distance up to which the consecutive tangent vectors on the contour do not bend appreciably and is defined by $\langle \hat{t}(s).\hat{t}(0) \rangle = \exp(-s/\lambda)$.

In this section we present a theoretical method to solve WLC model to any desired accuracy for both the Helmholtz and Gibbs ensemble and all three possible boundary orientations over

the entire range of stiffness parameter t. We first develop the method for a free polymer. Then we extend it to calculate properties of grafted [one/both end(s)] polymers.

If the tangent vectors of two ends of a polymer are held fixed at $\hat{t}_i$ and $\hat{t}_f$, the probability distribution of end to end vector in constant extension ensemble can be written in path integral notation as

$$P(\vec{r}) = \mathcal{N} \int_{\hat{t}_i}^{\hat{t}_f} \mathcal{D}[\hat{t}(s)] \exp\left(-\beta \mathcal{H}\right) \times \delta^d \left(\vec{r} - \int_0^L \hat{t} ds\right) \tag{3.3}$$

where $\beta \mathcal{H}$ is given by Eq.3.2 and $\mathcal{D}[\hat{t}(s)]$ denotes integration over all possible paths in tangent vector space from tangent at one end $\hat{t}_i$ to tangent vector at the other end $\hat{t}_f$. In d- dimensions $\vec{r} = (r_1, r_2, \ldots, r_d)$. There is no eaxct analytic calculation of this distribution because of the difficulty presented by the inextensibility constraint introduced via the Dirac- delta function, though some mean field way of enforcing this constraint exist[31, 49]. Unfortunately that do not capture the very interesting triple maxima feature of the radial distribution at intermediate stiffness values as obtained in Ref.[42]. Recently, following our earlier work[42], J. Samuel *et. al.* [41] developed a path integral Greens function formulation to evaluate the distribution for a free polymer in 3D. We closely follow that method to generalize that to obtain results for various orientation constraints on polymer ends.

The integrated (projected) probability distribution is given by,

$$P_x(x) = \int d\vec{r} P(\vec{r}) \delta(r_1 - x). \tag{3.4}$$

We define the generating function of $P_x(x)$ via Laplace transform as,

$$\begin{aligned} \tilde{P}(f) &= \int_{-L}^{L} dx \exp(Fx/k_B T) P_x(x) \\ &= \int_{-L}^{L} dx \exp(fx/\lambda) P_x(x) \end{aligned} \tag{3.5}$$

where f is the force in units of $k_B T/\lambda$ i.e. $f = F\lambda/k_B T$ applied along the x- axis. This gives,

$$\begin{aligned} \tilde{P}(f) &= \mathcal{N} \int_{\hat{t}_i}^{\hat{t}_f} \mathcal{D}[\hat{t}(s)] e^{\left(-\frac{(d-1)\lambda}{4} \int_0^L ds \left(\frac{\partial \hat{t}(s)}{\partial s}\right)^2 + \frac{f}{\lambda} \int_0^L \hat{t}_x ds\right)} \\ &= \mathcal{N} \int_{\hat{t}_i}^{\hat{t}_f} \mathcal{D}[\hat{t}(\tau')] e^{\left[-\int_0^t \left\{\frac{(d-1)}{4} \left(\frac{\partial \hat{t}(\tau')}{\partial \tau'}\right)^2 - f\hat{t}_x\right\} d\tau'\right]} \end{aligned} \tag{3.6}$$

The last step is obtained by replacing $\tau' = s/\lambda$, $t = L/\lambda$ and using the identity $\kappa = (d-1)\lambda/2$. Note that, $\tilde{P}(f)$, is the partition function in constant force ensemble where t behaves like an

inverse temperature such that the Gibb's free energy can be written as $G(f) = -1/t \; \ln \tilde{P}(f)$. Now considering τ' as imaginary time and replacing $\tau = -i\tau'$ we get,

$$\tilde{P}(f) \;\; = \;\; \mathcal{N} \int_{\hat{t}_i}^{\hat{t}_f} \mathcal{D}[\hat{t}(\tau)] e^{\left[i \int_0^{-it} \left\{ \frac{(d-1)}{4} \left(\frac{\partial \hat{t}(\tau)}{\partial \tau} \right)^2 + f\hat{t}_x \right\} d\tau \right]}$$

$$= \;\; \mathcal{N} \int_{\hat{t}_i}^{\hat{t}_f} \mathcal{D}[\hat{t}(\tau)] e^{\left[i \int_0^{-it} L d\tau \right]} \tag{3.7}$$

With the identification of $L = \frac{(d-1)}{4} \left(\frac{\partial \hat{t}(\tau)}{\partial \tau} \right)^2 + f\hat{t}_x$ as the Lagrangian, $\tilde{P}(f) \; [= \tilde{Z}(f)/\tilde{Z}(0) \;]$ in the above expression is the path integral representation for the propagator of a *quantum* particle, on the surface of a d- dimensional sphere, that takes a state $|\hat{t}_i\rangle$ to $|\hat{t}_f\rangle$. In Schrödinger picture this can be written as the inner product of a state $|\hat{t}_i\rangle$ and another state $|\hat{t}_f\rangle$ evolved by imaginary time $-it$,

$$\tilde{Z}(f) = \langle \hat{t}_i | \exp(-i\hat{H}(-it)) | \hat{t}_f \rangle = \langle \hat{t}_i | \exp(-t\hat{H}) | \hat{t}_f \rangle. \tag{3.8}$$

Once $\tilde{P}(f) = \tilde{Z}(f)/\tilde{Z}(0)$ is calculated, performing an inverse Laplace transform we can obtain the projected probability density $P_x(x)$. We now describe how to do that. Eq.3.5 can be written as,

$$\tilde{P}(f) \;\; = \;\; \int_{-L}^{L} dx \exp(fx/\lambda) P_x(x)$$

$$= \;\; \int_{-1}^{1} dv_x \exp(tf \; v_x) L P_x(x)$$

$$= \;\; \int_{-1}^{1} dv_x \exp(tf \; v_x) p_x(v_x) \tag{3.9}$$

where $v_x = x/L$ and $p_x(v_x) = L P_x(x)$ is a scaling relation. Note that the Helmholtz free energy is given by $\mathcal{F}_x(v_x) = -(1/t) \ln p_x(v_x)$. Therefore, we can write the above expression as,

$$\exp[-tG(f)] = \int_{-1}^{1} dv_x \exp(tf \; v_x) \exp[-t\mathcal{F}_x(v_x)].$$

This is the relation between free energies of Helmholtz and Gibbs ensemble for a finite chain (finite t). In thermodynamic limit of $t \to \infty$ a steepest descent approximation of the above integral relation gives $G(f) = \mathcal{F}_x(v_x) - f v_x$, the normal Legendre transformation. Let us use the identity,

$$p_x(v_x) = \frac{1}{2\pi} \int_{-\infty}^{\infty} e^{iuv_x} du \int_{-1}^{1} p_x(w) e^{-iuw} dw \tag{3.10}$$

In it we can define $\tilde{p}_x(u) = \int_{-1}^{1} p_x(w) \exp(-iuw) dw$ as the Fourier transform and

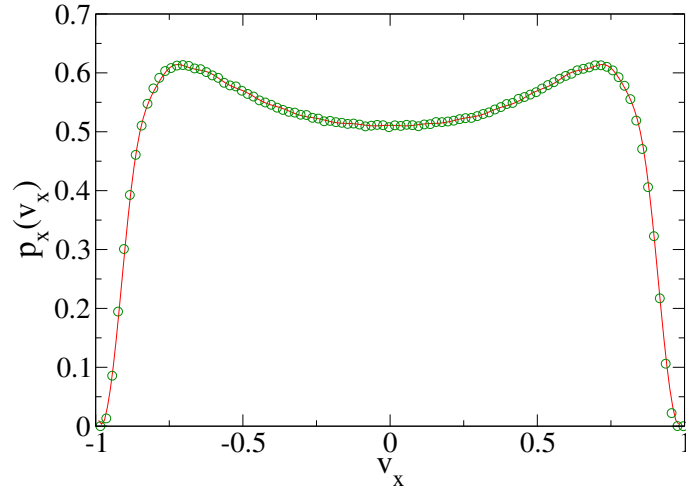$$p_x(v_x) = \frac{1}{2\pi} \int_{-\infty}^{\infty} du \tilde{p}_x(u) \exp(iuv_x) \tag{3.11}$$

FIGURE 3.2: For a semiflexible polymer having its ends free to rotate $p_x(v_x)$ ($= p_y(v_y)$) is plotted at stiffness parameter $t = 2$. The points are collected from Monte- Carlo simulation in freely rotating chain model (see Sec.3.2). The line is calculated from theory (see Sec.3.1). The theory matches exactly with simulation. It clearly shows bistability via two maxima in integrated probability density at the two near complete extensions.

as the inverse Fourier transform. Now, with $-iu = tf$ we get $\tilde{P}(f) = \tilde{p}_x(u = ift)$ and the inverse Fourier transform can be written as an inverse Laplace transform,

$$p_x(v_x) = t\frac{1}{2\pi i} \int_{-i\infty}^{i\infty} df \, \tilde{P}(f) \exp(-tfv_x) \qquad (3.12)$$

This gives the relation between the partition function $\tilde{P}(f)$ in the constant force ensemble and the projected probability density of end to end separation $p_x(v_x)$ along any given direction x in the constant extension ensemble. In numerical evaluation, the simplest way to obtain $p_x(v_x)$ is to replace $f = -iu/t$ in the expression for $\tilde{Z}(f)$ to obtain $\tilde{p}_x(u)$ and evaluate the inverse Fourier transform (Eq.3.11).

Up to this point everything has been treated in d- dimensions. Experiments on single polymer can be performed in 3D as well as in 2D. In 3D polymers are left in a solution whereas one can float the polymer on a liquid film to measure its properties in 2D [16]. Moreover, polymers embedded in 2D are more interesting because of the following reason. It was shown that in Helmholtz ensemble in three dimensions[41],

$$p(v_x) = -\frac{1}{2\pi v_x} \frac{dp_x}{dv_x} \qquad (3.13)$$

where $p(v_x)$ is the scaled radial distribution function $L^2 P(r) = p(v)$ with v replaced by v_x. Since $p(v)$ is a probability density $p(v) \geq 0$ and therefore $dp_x/dv_x \leq 0$ for $v_x > 0$ thus ruling

out multiple peaks in $p_x(v_x)$ [40] and showing that $p_x(v_x)$ will have single maximum at $v_x = 0$ for all stiffness parameter t. No such simple relation exists between $p(v_x)$ and $p_x(v_x)$ in two dimensions. Therefore, the two dimensional WLC polymer having its ends free to rotate may show more than one maximum in $p_x(v_x)$ and therefore non-monotonicity. Indeed our calculation and simulation (see Sec.3.2) does show non-monotonicity (Fig.3.2). This is a curious difference between semiflexible polymers in 2D and 3D. Because of this and the fact that experiments in 2D are possible, in this work we focus on the 2D WLC model.

We have already given a general form of $\tilde{Z}(f)$ (Eq.3.8) which depends on the dimensionality d of the embedding space of the polymer. $d = 3$ formulation of this theory for a polymer with its ends free to rotate has been carried out in detail in Ref.[41]. For $d = 2$, we can assume $\hat{t} = (\cos\theta, \sin\theta)$. Therefore, $L = \{1/4\ \dot{\theta}^2 + f\cos\theta\}$ and angular momentum $p_\theta = \frac{\partial L}{\partial \dot{\theta}} = \dot{\theta}/2$. Then the corresponding Hamiltonian is $H = \dot{\theta}p_\theta - L = p_\theta^2 - f\cos\theta$ and in planar polar coordinates, replacing $p_\theta \to -i\frac{\partial}{\partial \theta}$ we obtain the quantum hamiltonian operator, $\hat{H} = -\frac{\partial^2}{\partial \theta^2} - f\cos\theta$. In this representation of $\hat{t}$ we can write,

$$
\begin{aligned}
\tilde{Z}(f) &= \langle \theta_i | \exp(-t\hat{H}) | \theta_f \rangle \\
&= \sum_{n,n'} \langle \theta_i | n \rangle \langle n | \exp(-t\hat{H}) | n' \rangle \langle n' | \theta_f \rangle \\
&= \sum_{n,n'} \phi_n^*(\theta_i) \phi_{n'}(\theta_f) \langle n | \exp(-t\hat{H}) | n' \rangle
\end{aligned}
\tag{3.14}
$$

This propagator takes a definite tangent vector state $|\theta_i\rangle$ at one end of the polymer to a definite final tangent vector state $|\theta_f\rangle$ at the other end of it.

If external force is applied along x- direction as in Eq.3.5, $\hat{H} = \hat{H}_0 + \hat{H}_I = -\frac{\partial^2}{\partial \theta^2} - f\cos\theta$ where $\hat{H}_0 = -\frac{\partial^2}{\partial \theta^2}$ is the Hamiltonian for a free rigid rotor in 2D and $\hat{H}_I = -f\cos\theta$ is the part of Hamiltonian introduced by an external field. Thus the total Hamiltonian $\hat{H}$ denotes a rigid rotor in presence of a constant external field. The eigenvalues of $\hat{H}_0$, the hamiltonian for a 2D rigid rotor, are $E_n = n^2$ and the complete set of ortho- normalized eigen- functions are given by $\phi_n(\theta) = \exp(in\theta)/\sqrt{2\pi}$ where $n = 0, \pm 1, \pm 2, \ldots$. The orthonormality condition is $\langle n | n' \rangle = (1/2\pi) \int_0^{2\pi} d\theta \exp[i(n - n')\theta] = \delta_{n,n'}$. In this basis $\langle n | \hat{H}_I | n' \rangle = -(f/2)(\delta_{n',n+1} + \delta_{n',n-1})$. Therefore, $\langle n | \hat{H} | n' \rangle = n^2 \delta_{n',n} - (f/2)(\delta_{n',n+1} + \delta_{n',n-1})$. If the external force were applied in y- direction $\hat{H}_I = -f\sin\theta$ and $\langle n | \hat{H} | n' \rangle = n^2 \delta_{n',n} - (f/2i)(\delta_{n',n+1} - \delta_{n',n-1})$. $\langle n | \exp(-t\hat{H}) | n' \rangle$ can be calculated by exponentiating the matrix $\langle n | \hat{H} | n' \rangle$. Thus one can find $\tilde{Z}(f)$.

3.1.1 Free Polymer

For a polymer which has both its ends free to rotate, integrating Eq.3.14 over all possible initial and final tangent vectors in rigid rotor basis we get

$$
\tilde{Z}(f) = 2\pi\ \langle 0 | \exp(-t\hat{H}) | 0 \rangle
\tag{3.15}
$$

This means that $\tilde{Z}(f)$ is given by the $(0,0)$ element of the matrix $\langle n| \exp(-t\hat{H})|n'\rangle$. In this case $\tilde{Z}(0) = 2\pi \langle 0| \exp(-tH_0)|0\rangle = 2\pi \exp(-t \ 0^2) = 2\pi$ and therefore $\tilde{P}(f) = \tilde{Z}(f)/\tilde{Z}(0) = \langle 0| \exp(-t\hat{H})|0\rangle$. To evaluate the matrix element $\langle 0| \exp(-t\hat{H})|0\rangle$ we exponentiate the matrix $-t\langle n|\hat{H}|n'\rangle$ and pick up the $(0,0)$-th element. Thus, if the external force is applied in x- direction, remembering $\tilde{p}_x(u) = \tilde{P}(f = -iu/t)$ we calculate the inverse Fourier transform (Eq.3.11) to obtain $p_x(v_x)$. Here it is useful to note that due to spherical symmetry of a polymer whose ends are free to rotate $p_x(v_x) = p_y(v_y)$.

3.1.2 One End Grafted

This symmetry breaks down immediately if we hold one end of the polymer to a specific direction, namely along the x- direction *i.e.* $\theta_i = 0$. Then on Eq.(3.14) integrating over all possible θ_f and leaving $\theta_i = 0$ we obtain

$$\tilde{Z}(f) = \sum_n \langle n| \exp(-t\hat{H})|0\rangle \tag{3.16}$$

in the rigid- rotor basis. Note for this case $\tilde{Z}(0) = \sum_n \langle n| \exp(-tH_0)|0\rangle = \sum_n \exp(-tn^2)\delta_{n,0} = 1$ and therefore we have $\tilde{P}(f) = \tilde{Z}(f)$. If the external force acts in x- direction, the Laplace transform of $\tilde{Z}(f)$, defined in the way described above, gives the projected probability distribution in x- direction, $p_x(v_x)$. On the other hand, if the external force acts in y- direction, the Laplace transform of $\tilde{Z}(f)$ gives the projected probability distribution in y- direction $p_y(v_y)$, the distribution of transverse fluctuation while one end of the polymer is grafted in x- direction.

3.1.3 Both Ends Grafted

Two ends of a polymer can be grafted in infinitely different ways. Let us fix the orientation of one end along x- direction $(\theta_i = 0)$ and the other end is orientated along any direction θ_f, then Eq.(3.14) gives

$$\tilde{Z}(f) = \frac{1}{2\pi} \sum_{n,n'} e^{in'\theta_f} \langle n| \exp(-t\hat{H})|n'\rangle. \tag{3.17}$$

As above, to obtain $p_x(v_x)$ we use $\langle n|\hat{H}_I|n'\rangle = -(f/2)(\delta_{n',n+1} + \delta_{n',n-1})$, whereas to obtain $p_y(v_y)$ we use $\langle n|\hat{H}_I|n'\rangle = -(f/2i)(\delta_{n',n+1} - \delta_{n',n-1})$ to calculate $\tilde{P}(f)$ and perform inverse Laplace transform. For this case of grafting $2\pi\tilde{Z}(0) = \sum_{n,n'} e^{in'\theta_f} \langle n|e^{-tH_0}|n'\rangle = \sum_n e^{in\theta_f - tn^2}$ and therefore $\tilde{P}(f) = \sum_{n,n'} e^{in'\theta_f} \langle n|e^{-t\hat{H}}|n'\rangle / [\sum_n e^{in\theta_f - tn^2}]$.

Up to this point all the relations are exact. Since an infinite dimensional calculation of $\langle n| \exp(-t\hat{H})|n'\rangle$ is not feasible, we calculate it numerically up to a dimension N_d, that controls the accuracy, limited only by computational power [1]. We use $N_d = 10$ which already gives

---

[1]We use the MatrixExp function of Mathematica[60].

numbers for probability distribution which differs within 1% from that obtained from $N_d = 20$ and gives a fair comparison with simulated data (see Sec.4.2). The inverse Laplace transform to obtain $p_x(v_x)$ etc. from $\tilde{P}(f)$ is also done numerically.

3.2 Simulation

In this section, we introduce two discretized models used to simulate semi- flexible polymers. Both of these are derived from the WLC model which is used for our analytical treatment in Sec.3.1. After introducing the discretized models we have listed the various boundary conditions used. We perform Monte- Carlo (MC) simulations to obtain probability distributions in Helmholtz ensemble.

One discretized version of this model is the freely rotating chain (FRC) model[21]. In the FRC model one considers a polymer as a random walk of N steps each of length $b = L/N$ with one step memory, such that, successive steps are constrained to be at an fixed angle θ with $\lambda = 2b/\theta^2$. The continuum WLC model is obtained in the limit $\theta,\ b \to 0,\ N \to \infty$ keeping λ and L finite. To simulate a polymer with ends free to rotate a large number of configurations are generated with first step taken in any random direction. Whereas if one choses the first step to be in some specific direction, this will simulate a polymer with one end grafted in that direction.

A straight discretization of Eq.3.2 in 3D (2D) is an 1d Heisenberg (classical xy) model:

$$\beta \mathcal{H} \;\; = \;\; \frac{\kappa}{2} \sum_{i=1}^{N} \frac{(\hat{t}_i - \hat{t}_{i-1})^2}{b} = \sum_{i=1}^{N} (-J\ \hat{t}_i.\hat{t}_{i-1}) \tag{3.18}$$

with a nearest neighbour coupling $J = \kappa/b$ between 'spins' $\hat{t}_i$. We have ignored a constant term in energy. The appropriate continuum limit is recovered for $b \to 0,\ J \to \infty$ with $Jb = \kappa$ finite. In this model grafting is simulated by fixing end spins on the 1D chain. If an end is free then the end spin takes up any orientation that are allowed by the energy and entropy. In this model, by fixing the two end- spins, one can easily simulate a polymer with both its ends grafted in some fixed orientations. We follow the normal Metropolis algorithm to perform MC simulation in this model.

We restrict ourselves to two dimensions. The numerics were checked via exact calculation of $\langle r^2 \rangle$ and $\langle r^4 \rangle$ which match within 0.5%. In the FRC model simulations we have used a chain length of $N = 10^3$ and generated around 10^8 configurations. This simulation does not require equilibration run. Therefore all the 10^8 configurations were used for data collection. In xy model we have simulated $N = 50$ spins and equilibrated over 10^6 MC steps. A further 10^6 configurations were generated to collect data. We have averaged over 10^3 initial configurations, each of which were randomly chosen from nearly minimum energy configurations that conforms with the boundary conditions. Increasing the number of spins do not change the averaged data.
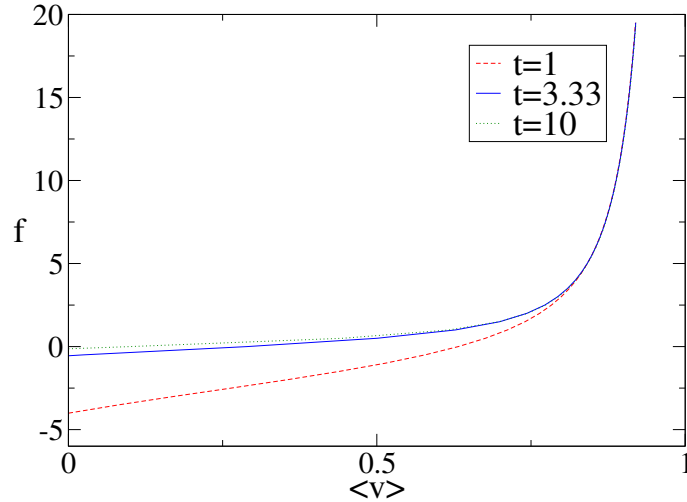
FIGURE 3.3: Compare this force- extension relation with that in Fig.2.4 of previous chapter. None of the curves including that at $t = 3.33$ show non- monotonic behaviour. This shows the force- extension behaviour in constant force ensemble. Forces are expressed in units of $k_B T/\lambda$.

3.3 Results

Once all these theoretical and simulation tools are available, we apply them to bring out statistical and mechanical properties of a semiflexible polymer. We have three different boundary conditions depending on the orientations of polymer ends and two different ensembles. For each case we look at the various probability densities, ensemble dependence of force- extension etc. For the case of a polymer with both ends grafted we find that the properties depend on the relative orientation of the two ends.

3.3.1 Free Polymer:

Helmholtz ensemble: We employ the theory as described in Sec.3.1 to calculate $p_x(v_x)$ and $p_y(v_y)$ for a polymer with both its ends free to rotate. We compare the probability distribution obtained at stiffness parameter $t = 2$ with that obtained from MC simulation (Sec.3.2) using the FRC model (see Fig.3.2). This shows exact agreement between theory and simulation. For a free polymer $p_x(v_x)$ and $p_y(v_y)$ are same due to the spherical symmetry. Note that, $\mathcal{F}(v_x) = -1/t \ln p_x(v_x)$ would give a non- monotonic force- extension via $\langle f_x \rangle = (\partial \mathcal{F}/\partial v_x)$. The force- extension obtained from the projected probability density $p_x(v_x)$ will describe the experimental scenario in which the external potential traps the polymer end only in x- direction and constant in y. In general, if the external potential traps the polymer in d_r dimensions ($d_r \leq d$) then a d_r dimensional projection (($d-d_r$) dimensional integration) of the probability distribution
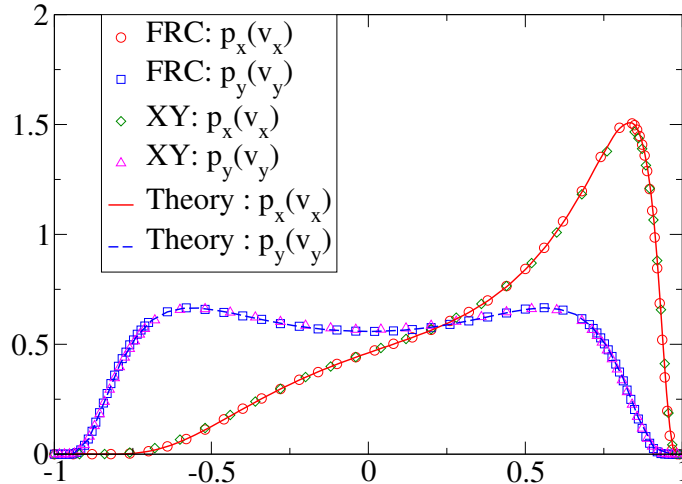
FIGURE 3.4: The simulation data for $p_x(v_x)$ and $p_y(v_y)$ from FRC model and XY- model simulations are compared with their theoretical estimates. Simulations and calculations were done at $t = 2$ for a polymer with one end grafted in x- direction. The data labelled LMF is taken from Ref.[43].

of end to end vector $p(\vec{v})$ gives the free energy and decides the force- extension relation. This understanding is general and do not depend on the orientational boundary conditions at the polymer ends or the dimensionality of embedding space. This is important to keep in mind while analyzing experimental data.

Gibbs ensemble: We have already mentioned that the non- monotonic nature of free energy, a strong qulitative signature of semi- flexibility, is observable only in Helmholtz ensemble not in Gibbs ensemble [42]. The partition function in Gibbs ensemble with force f applied in x- direction gives the Gibb's free energy $G(f) = -(1/t) \ln[\tilde{P}(f)]$. From this the averaged extension comes out to be $\langle v_x \rangle = -(\partial G/\partial f)$. For a polymer with its ends free to rotate, this force extension relations, that have been calculated from theory, at various t are shown in Fig.3.3. Notice that $\partial \langle v_x \rangle / \partial f = t[\langle v_x^2 \rangle - \langle v_x \rangle^2] \geq 0$. Similar relation for response function does not exist in Helmholtz ensemble. Therefore, the force- extension in Gibbs ensemble has to be monotonic (Fig.3.3) in contrast to Helmholtz ensemble. Note that, for any non-zero stiffness, negative force is required to bring the end to end separation to zero. The amount of this force is larger for larger stiffness (smaller t). At large and positive force polymer goes to fully extended limit whichafter inextensibility constraint stops the polymer to extend any more.

3.3.2 Grafted Polymer: One End

Helmholtz ensemble: Next, we use our thery to plot $p_x(v_x)$ and $p_y(v_y)$ at $t = 2$ (Fig.3.4) for a semiflexible polymer with one end grafted in x- direction. In Fig.3.4 we have also plotted MC
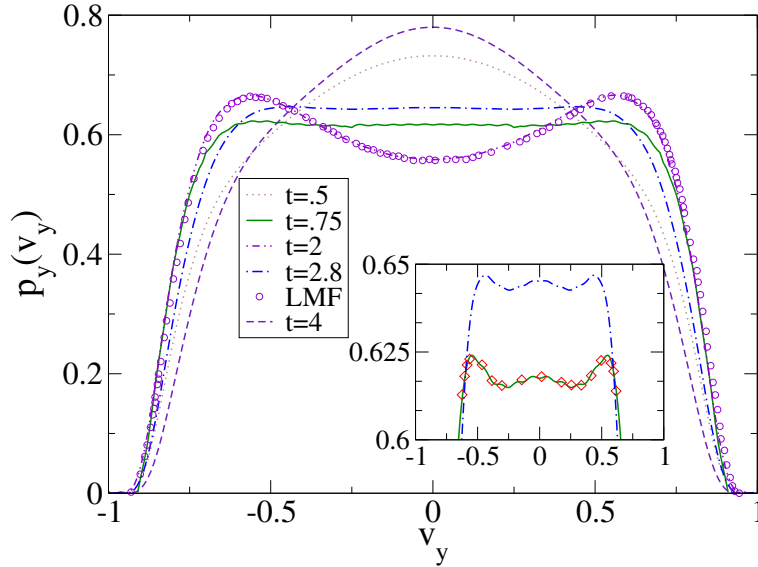
FIGURE 3.5: The integrated probability density $p_y(v_y)$ is plotted at various stiffnesses t. At $t = 4$ there is a single maximum at $v_y = 0$. Decreasing t we see at $t = 2.8$ emergence of two more peaks at nonzero v_y except for the one at $v_y = 0$ (See inset). At $t = 2$ central peak vanishes, the trimodal distribution becomes bimodal. The circles labeled LMF are data taken from Ref.[43] at $t = 2$ to show exact agreement with our theory. At $t = 0.75$ we see re-emergence of the central peak and tri-modality in $p_y(v_y)$ (See inset, ◇s are from our MC simulation in the FRC model at $t = 0.75$, the lines are calculated from theory).

data from the FRC model and xy model simulation. The exact match validates our theory and both the simulation techniques. In $p_x(v_x)$ the peak in near complete extension along positive x is due to the large bending energy and orientation of the other end towards this direction (also see $p(v_x, v_y)$ in Fig.3.13). We then explore the transverse fluctuation $p_y(v_y)$ of this system, in detail, for different t (Fig.3.5). At large $t(= 10)$, $p_y(v_y)$ has single maximum at $v_y = 0$. At such low stiffnesses entropy takes over energy contributions. Number of possible configurations and thus entropy gains if end to end separation remains close to zero. This gives rise to this single central maximum. The emergence of multiple maxima at nonzero v_y in polymers, the multi- stability, with larger stiffness ($t = 2.8$) is due to the entropy- energy competition. The central peak is due to the entropy driven Gaussian behavior. The other two peaks emerge as entropy tries the polymer to bend around $v_y = 0$ and energy restricts the amount of bending. Since bending in positive and negative y- directions are equally likely, the transverse fluctuation shows two more maxima at non- zero v_y. With further increase in stiffness ($t = 2$), the central Gaussian peak vanishes (see Fig.3.13) and therefore $p_y(v_y)$ becomes bistable with two maxima (Fig.3.5). At even higher stiffness ($t = 0.75$) central peak reappears, this time due to higher bending energy. At $t = 0.5$ the distribution again becomes single peaked at $v_y = 0$ as entropy almost completely
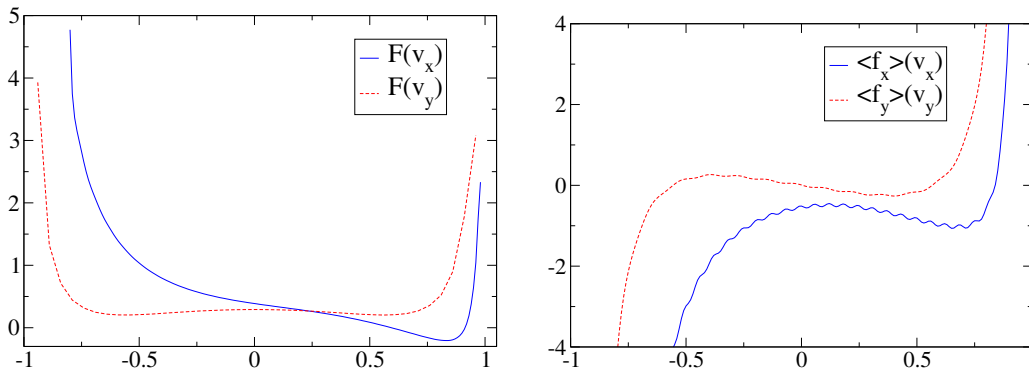
FIGURE 3.6: The left panel shows the Helmholtz free energies $\mathcal{F}(v_x)$ and $\mathcal{F}(v_y)$ of a polymer with $t = 2$ and one end grafted in x- direction. The right panel shows the corresponding force- extensions in Helmholtz ensemble. Both $\langle f_x \rangle$- v_x and $\langle f_y \rangle$- v_y show regions of negative slope. Free energies are expressed in units of $k_B T$ and forces are expressed in units of $k_B T/\lambda$.

loses out. This is the rigid rod limit. Notice that we have plotted MC data as obtained in Ref.[43] for xy model simulation at $t = 2$. This agrees exactly with our theory. In the inset of Fig.3.5 we have blown up the multistability at $t = 2.8$ and $t = 0.75$. We have also plotted our FRC model simulation data at $t = 0.75$ for comparison.

At this point it is instructive to look at the force extension behavior in Helmholtz ensemble, the ensemble in which $p_y(v_y)$ and $p_x(v_x)$ have been calculated above. In it the extension v_x [or v_y] is held constant and the corresponding average force in x- [or y-] direction is found from the relation $\langle f_x \rangle = \partial \mathcal{F}(v_x)/\partial v_x$ (or $\langle f_y \rangle = \partial \mathcal{F}(v_y)/\partial v_y$). In Fig.3.6 we show the Helmholtz free energies $\mathcal{F}(v_x) = -(1/t)\ln p_x(v_x)$ and $\mathcal{F}(v_y) = -(1/t)\ln p_y(v_y)$ and the corresponding force extension curves in constant extension ensemble. Note that unlike the monotonicity beared by $\langle v_y \rangle$-f_y curve (Fig.3.7) obtained in Gibbs ensemble the $\langle f_y \rangle$-v_y curve in Fig.3.6 clearly shows non-monotonicity, a signature of the Helmholtz ensemble.

Gibbs ensemble: From our theory we can also explore the transverse response of a polymer which has one of its ends grafted to a substrate and a constant force is applied to the other end in a direction transverse to the grafting. Assume that the grafting direction is x and we apply a force f_y in y- direction to study the response. A linear response theory was proposd earlier[53] to tackle this qustion. Our theory can predict the effect of externally applied force f_y of arbitary magnitude on the average positions $\langle v_x \rangle$ and $\langle v_y \rangle$. As the force is applied in y-direction i.e. $\vec{f} = \hat{y}f_y$, we have $H_I = -f_y \sin\theta$. Because one end of the polymer is grafted in x- direction we use $\langle n|\hat{H}_I|n'\rangle = -(f_y/2i)(\delta_{n',n+1} - \delta_{n',n-1})$ to evaluate $\tilde{Z}(f_y)$, whereas to calculate $\langle v_x \rangle = -(\partial G/\partial f_x)$ [or, $\langle v_y \rangle = -(\partial G/\partial f_y)$] we introduce a small perturbing force δf_x (or, δf_y) in the Hamiltonian matrix to obtain the partial derivatives. Thus we obtain the corresponding force- extensions shown in Fig.3.7. As the grafted end is oriented in x- direction
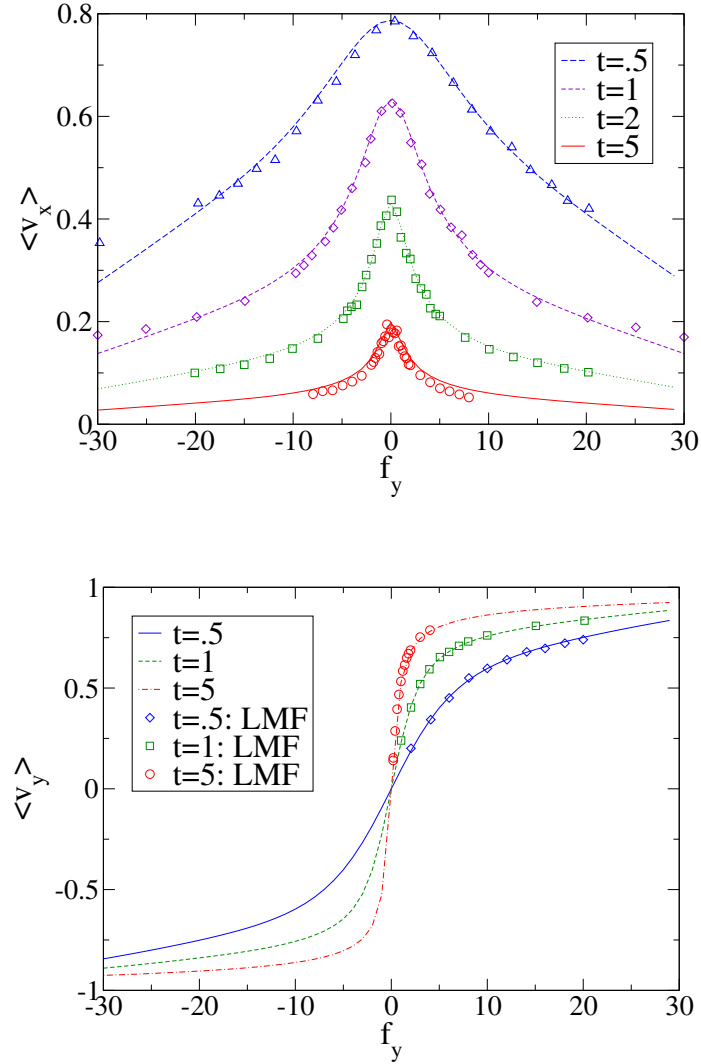
FIGURE 3.7: Average displacements along x- direction $\langle v_x \rangle$ and y- direction $\langle v_y \rangle$ as a function of transverse force (transverse to grafting direction) in constant force ensemble. Lines denote our theoretical calculation while points denote the MC simulation data taken from Ref.[43]. Forces (F_y) are expressed in units of $k_B T/\lambda$, i.e. $f_y = F_y \lambda / k_B T$.

we expect in absence of any external force $\langle v_x \rangle$ will be maximum and will keep on reducing due to the bending of the other end generated by the external force imposed in y- direction. Thus $\langle v_x \rangle$ is expected to be independent of the sign of f_y. Similarly $\langle v_y \rangle$ should follow the direction of external force and therefore is expected to carry the same sign as f_y. Fig.3.7 verifies these expectations and shows the comparison of our theory with simulated data taken from Ref.[43].
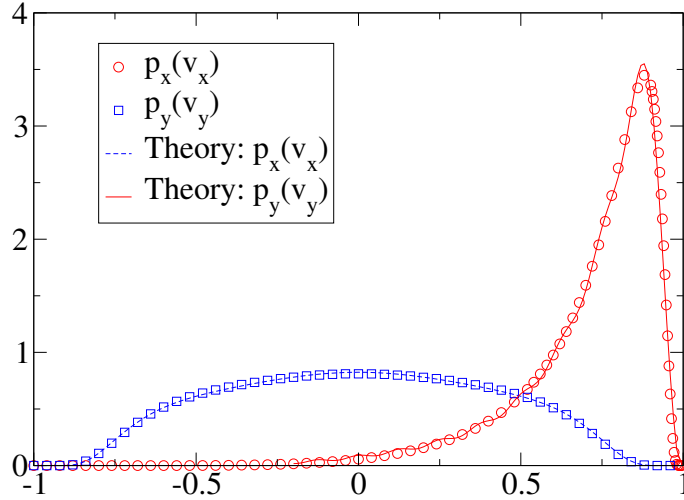
FIGURE 3.8: The simulation data for $p_x(v_x)$ and $p_y(v_y)$ from XY- model simulations of a WLC polymer are compared with their theoretical estimates. Simulations and calculations were done at $t = 2$ for a WLC polymer with both its ends grafted in x- direction.

3.3.3 Grafted Polymer: Both Ends

Helmholtz ensemble: Let us first fix the orientations of the polymer at both its ends along x- axis and compare $p_x(v_x)$ and $p_y(v_y)$ obtained from our xy model simulation and our theory (Fig.3.8). This validates both our theory and simulation. Next, we go on to explore the properties of this system using our theory. We take a polymer with both its ends grafted, orientation of first end is fixed in x- dirction ($\theta_i = 0$) and that in the other end (θ_f) is varied to study the change in transverse fluctuation $p_y(v_y)$.   To begin with let us find $p_y(v_y)$ for different stiffnesses t with $\theta_f = 0$ (Fig.3.9). The height of central peak shows non- monotonicity; with increase in t from $t = 1$ the height of central peak first decreases up to $t = 2$ and then eventually again increases. The initial decrease in the height of the maximum is due to the fact that with increase in t the other end of the polymer (relative to the first end) starts to sweep larger angles about x- axis. With further increase in t entropic contributions that favor $\vec{v} = 0$ win over to increase the height of the maximum (see Fig.3.13). Note that, $p_y(v_y)$ does not show multimodality as has been seen in the transverse fluctuation of a polymer with one end grafted.

    We then fix the stiffness at $t = 4$ and rotate the orientation of the other end and find out the transverse fluctuation $p_y(v_y)$ (transverse to the orientation of first end, see Fig.3.9). At $\theta = \theta_f = 0$ the fluctuation is unimodal with the maximum at $v_y = 0$. With increase in θ the orientation of the other end rotates from positive x- axis towards positive y- axis.   Energetically the polymer gains the most if it bends on the perimeter of a circle. Therefore, energetically at any θ, the peak of $p_y(v_y)$ should be at $v_y = (\ 1. - \cos\theta\ )/\theta$. Thus at $\theta = 0, \pi/4, \pi/2, 3\pi/4, 7\pi/8, \pi$ the
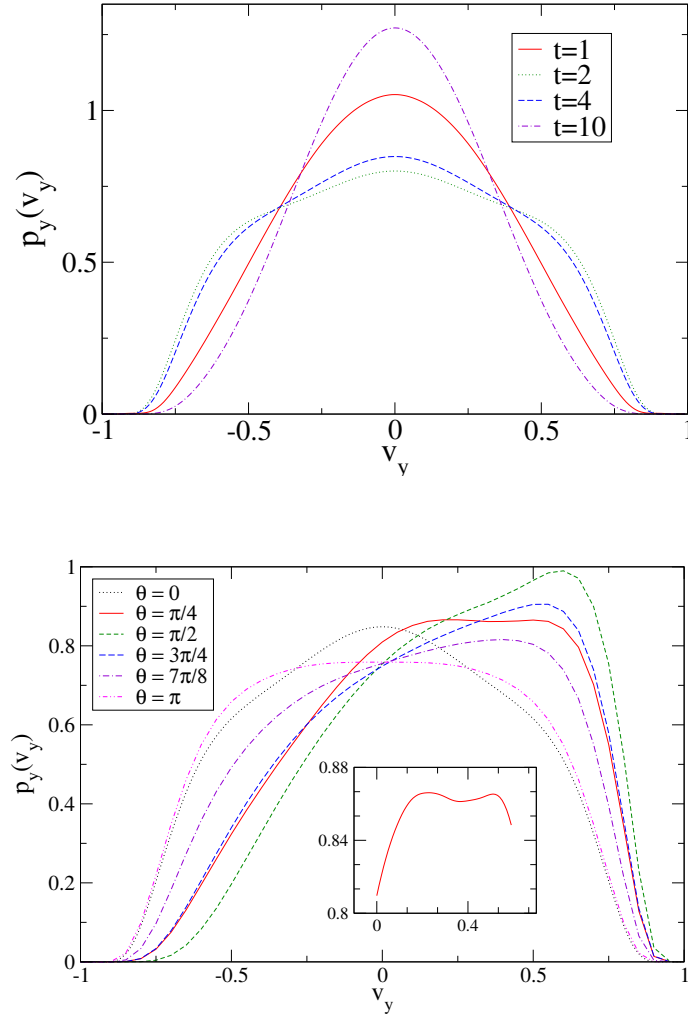
FIGURE 3.9: The upper panel shows $p_y(v_y)$ response of a polymer with both ends grafted along the same direction at various stiffness parameters t. They always remain single moded. In lower panel, $p_y(v_y)$ plotted for various relative angle between the orientations of two ends θ at $t = 4$. The inset shows imergence of bistability at $\theta = \pi/4$.

peak of $p_y(v_y)$ should be, respectively, at $v_y = 0, 0.37, 0.64, 0.72, 0.69, 0.64$. Fig.3.9 shows that the peak positions almost follow these values up to $\theta = \pi/2$, above which entropic contribution dominates. However, entropy always play a crucial role, e.g. at $\theta = \pi/4$ showing a double peak around $v_y = 0.37$. At $\theta = \pi$ the two ends of the polymer are anti- parallel. Notice that, as $\theta = \pi$ and $\theta = -\pi$ are physically the same thing, $v_y = \pm0.64$ are equally likely. Entropy would like the two ends to bend to $v_y = 0$. Competition between energy and entropy leads to almost a constant distribution up to $|v_y| \sim 0.5$. Notice that the bending energy couples to end orientations. For end orientations perpendicular to each- other, this coupling is strongest leading to a peak position that is closest to energetic expectation. The behavior of $p_y(v_y)$ for
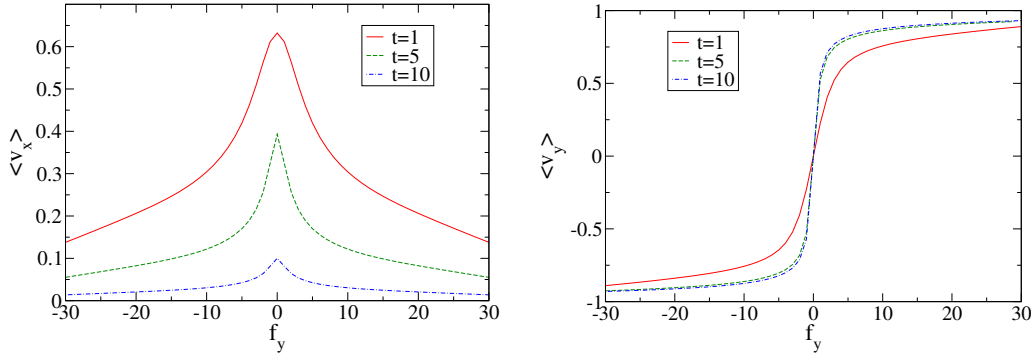
FIGURE 3.10: The left panel shows the transverse response and the right panel shows the longitudinal response of a polymer with both ends grafted along the same direction.

$-\pi \leq \theta \leq 0$ is mirror symmetric about $v_y = 0$ with respect to the behaviour of $p_y(v_y)$ in the region $0 \leq \theta \leq \pi$.

Gibbs ensemble: We then work in the constant force ensemble by applying a force $\vec{f} = \hat{y} f_y$. Let us fix $\theta = 0$, i.e. both ends are oriented along x- axis. We find out the corresponding transverse and longitudinal response to this force in the similar manner as in the case of a polymer with one end grafted (see Fig.3.10). The force extension carries the same qualitative features as for a single end grafted polymer. For other end orientations ($\theta \neq 0$) $\langle v_x \rangle$ and $\langle v_y \rangle$ does not remain at zero at $f_y = 0$. Otherwise the nature of responses remain the same. To see the impact of the change in relative angle θ between the orientations at the two ends we calculate the average extension of the polymer ends in x- and y- directions as we vary θ in constant force ensemble at $f = 0$. Due to the bending energy, the $\langle v_x \rangle$ is expected to by highest at $\theta = 0$ and lowest for $\theta = \pm\pi$. Similarly, $\langle v_y \rangle$ is expected to be highest at $\theta = \pm \pi/2$ and lowest for $\theta = 0$ and $\theta = \pm\pi$. Fig.3.11 shows, while $\langle v_x \rangle - \theta$ bears out the above expectations for all t, the expectation of getting highest magnitude for $\langle v_y \rangle$ at $\theta = \pm \pi/2$ is fulfilled only for lower stiffnesses ($t \geq 5$). At lower t the highest $\langle v_y \rangle$ shifts towards higher relative angles θ as bending energy takes over entropy. Note that, the smaller t gets, larger gets $\langle v_y \rangle$, an impact of larger stiffness.

3.3.4 End to End Vector Distribution

We now employ MC simulations to study some other aspects of probability distribution in Helmholtz ensemble. We first examine the radial distribution function $p(v)$ ($v = r/L$, $p(v) = L^2 P(r)$). It is clear from Fig.3.12 that grafting one end does not change the double maxima feature in $p(v)$ at intermediate values of stiffness ($4 \leq t \leq 2$). Though grafting both the ends change the distribution function, the double maxima feature persists. Here we note that once one end of a polymer is grafted immediately the system loses its spherical symmetry, more
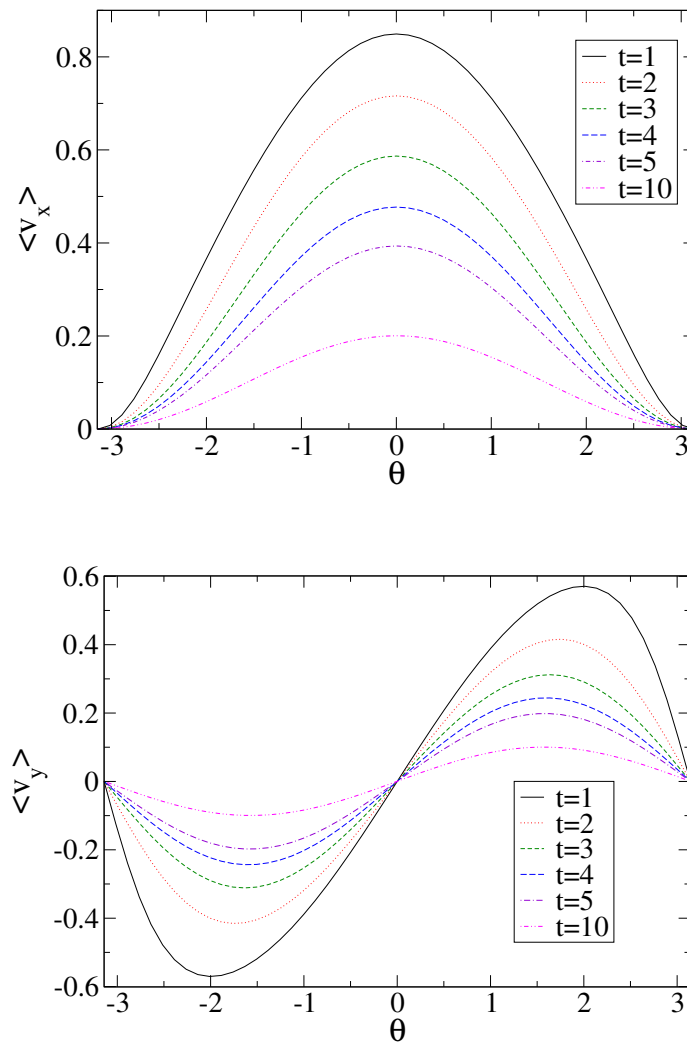
FIGURE 3.11: The upper panel shows the variation of $\langle v_x \rangle$ as a function of θ and the lower panel shows the variation of $\langle v_y \rangle$ as a function of θ. $\langle v_x \rangle$ and $\langle v_y \rangle$ are calculated for stiffness parameters $t = 1, 2, 3, 4, 5, 10$.

so, since we restrict ourselves to semi-flexible regime. We have already seen that the projected probability distribution $p_x(v_x)$ and $p_y(v_y)$ are very different depending on the orientations of polymer ends. However, for grafting of one end, this does not show up in radial distribution function $p(v)$ (Fig.3.12). This is because, fixing one end only shifts the probability weight distributed over all possible angles at a given radial distance v towards the direction of orientation but on the same radial distance.

The full statistics is encoded in the vector distribution function $p(v_x, v_y)$. To see the complete structure of it we next obtain $p(v_x, v_y)$ from MC simulations in FRC (for one or both ends of the polymer free to rotate) and xy- model (for polymer with both its ends fixed in some
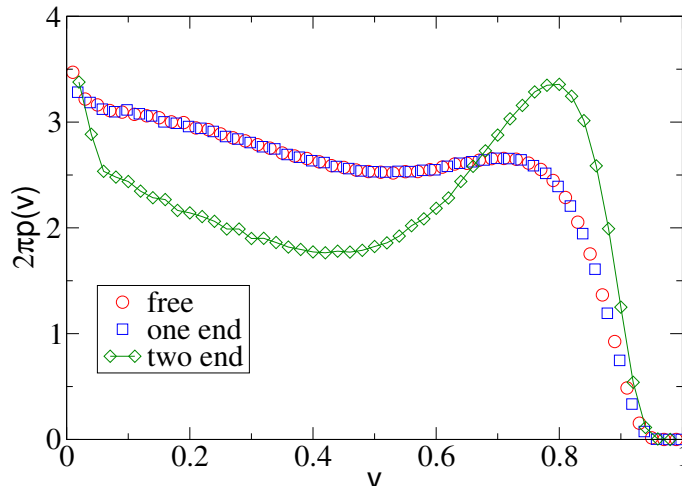
FIGURE 3.12: The radial distribution function $p(v)$ at stiffness $t = 4$ is plotted for the three different boundary conditions – (a) both ends free, (b) one end oriented in x- direction and the other is free, (c) both ends oriented in x- direction. Radial distribution of first two cases are equal, whereas for the third case it is different. However, all three show double maxima.

given orientation) and plot the total distribution $p(v_x, v_y)$ as a two dimensional density plot. We compare $p(v_x, v_y)$ of free polymer, polymer with one end grafted and polymer with both ends grafted (Fig.3.13). For definiteness we chose all the graftings to be in the x- direction. We plot $p(v_x, v_y)$ over a range of stiffnesses ($t = 0.5, 2, 4, 10$). The distribution has finite values for $v \leq 1$ and zero for $v > 1$. This is due to the inextensibility constraint in WLC model. In these density plots high probability is shown in red and low in blue (Fig.3.13). At small stiffness (large t) $p(v_x, v_y)$ shows a single entropic peak, at $\vec{v} = 0$ for free polymer and slightly shifted towards the direction of end- orientations in grafted polymers. This shifted entropic peak slowly moves to $\vec{v} = 0$ in the limit $t \to \infty$.

With increase in stiffness ($t = 4$) an energy dominated probability peak starts to appear near the full extension limit $v = 1$ of the polymer. This peak forms a circular ring for free polymers. For a grafted polymer this peak is aligned in the direction of grafting. The probability distribution $p(v_x, v_y)$ at $t = 4$ clearly shows two regions of probability maxima, one near zero extension another near full extension, that gives rise to the double maxima in radial distribution function [42].

At larger stiffness ($t = 2$) the entropic maximum near the centre ($\vec{v} = 0$) disappears. For the free polymer, one energy dominated maximum gets equally distributed over all angles. This way the system uses its spherical symmetry to gain in entropy. For grafted polymers, probability maximum near the full extension fans a finite solid angle around the direction of grafting. The distribution around the grafting direction is narrower for the polymer with both its ends grafted
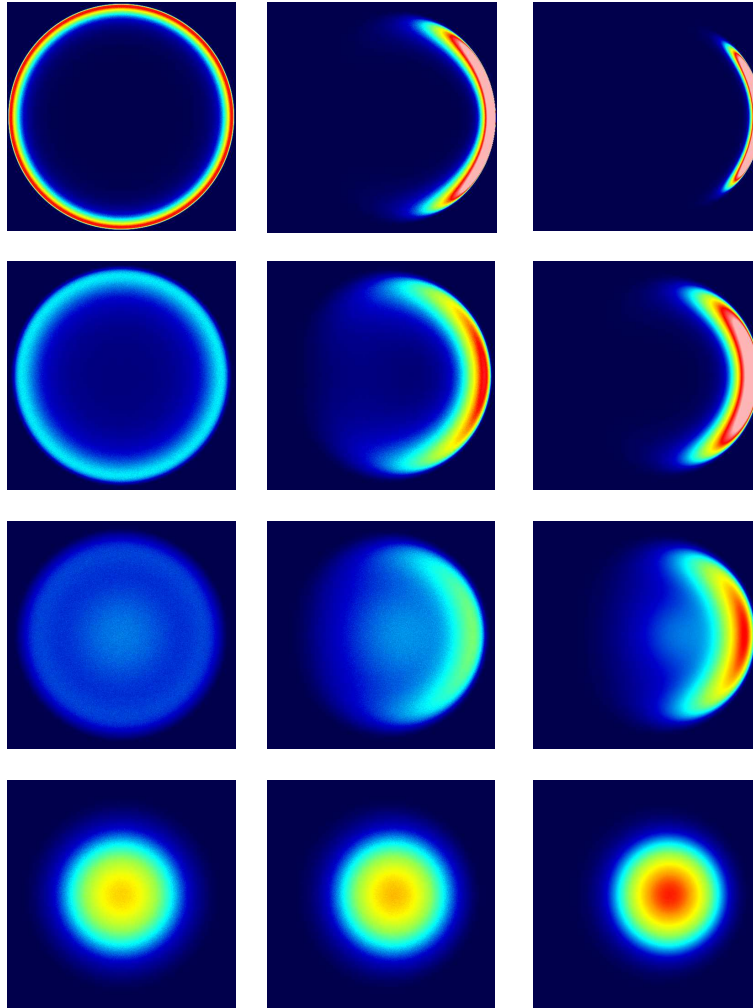
FIGURE 3.13: Density plot of $p(v_x, v_y)$. Color code : red - high density, blue - low density. Left panel is for free polymer, middle panel is for polymer having one end grafted in x- direction and the right panel is for polymer having both ends grafted in x- direction. From top to bottom four panels denote stiffness values $t = .5, 2, 4, 10$. Note that the double maxima feature in $p(v_x, v_y)$ (one maximum near the centre and another near the rim) at $t = 4$ persists for all three boundary consitions.

along the same direction. End orientation and bending energy couples to decide the probability distribution. This coupling is higher at smaller t [55]. This fact is more pronounced in plot of $p(v_x, v_y)$ at $t = 0.5$ (Fig.3.13). Spakowitz *et. al.* have investigated $p(v_x, v_y)$ using their Greens function calculations for a polymer with one of its ends grafted [55]. In this section we have used MC simulations to study $p(v_x, v_y)$ for all the possible boundary conditions. We have shown that multiple maxima in $p(v_x, v_y)$ persists near $t = 4$ for all these boundary conditions.

As mentioned earlier, in Helmholtz ensemble the free energy is given by $\mathcal{F}(v_x, v_y) = -(1/t) \ln[p(v_x, v_y)]$. In Fig.3.14 we plot this free energy profile on constant $v_x = 0$ line at $t = 4$ and compare the three
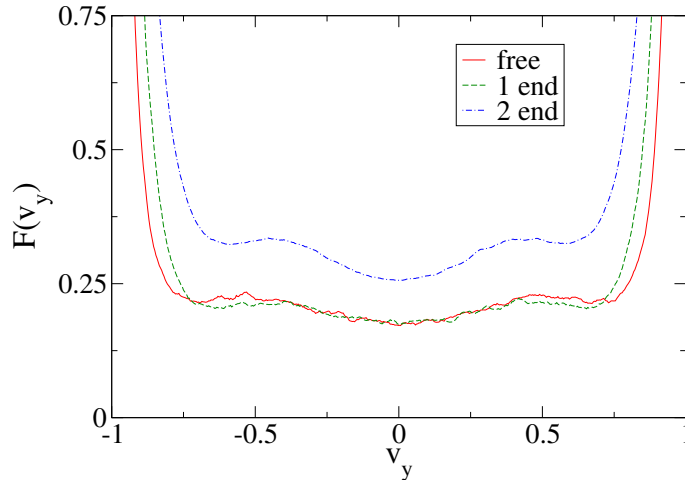
FIGURE 3.14: At $t = 4$ free energy profile $\mathcal{F}(v_y)$ in y- direction at $v_x = 0$ corresponding to the probability distributions shown in Fig.3.13 are plotted. This clearly shows that the triple minima feature in free energy for a polymer with both ends free persists even after grafting one or both ends of the polymer.

different boundary conditions. This is obtaind from $v_x = 0$ cut of 2D probability density $p(v_x, v_y)$. This plot clearly shows that triple minima in free energy [42] prevails even after grafting one or both ends of a semi- flexible polymer. This means that in constant extension ensemble if one fixes the position of one end and traps the other end in 2D (both x- and y- directions) to extend the end to end separation of a semiflexible polymer from the first free energy minimum at $v_y = 0$ to full extension of v_y along $v_x = 0$ line, for small extensions an average force will try to pull back the separation to zero corresponding to the central minimum of the free energy. However, once the separation is taken beyond the maxima in the free energy near $v_y = \pm 0.5$ the average force will push the separation away from the center towards the non- zero v_y minima in free energy. Further extension will cause a huge force towards this second minimum in the free energy. This is due to the inextensibility constraint in WLC model. Thus, in force- extension experiments on a polymer in constant extension ensemble, this multi- stability (non- monotonic force extension) at intermediate stiffness values will be measurable for all kind of boundary conditions[42]. The coupling of end orientation and bending energy have raised the free energy of a polymer with both its ends grafted, with respect to that of a free polymer and a polymer with one of its grafted (Fig.3.14).

We again emphasize that whether the end to end vector distribution or some projected proba- bility distribution will capture the results of a force- extension measurement will depend on the kind of trapping potential (what are the directions in which it traps a polymer end). Apart from this, as we have shown, the orientational boundary conditions at the ends of a polymer and the

ensemble of experiment will affect the force- extension behavior non- trivially.

3.4 Conclusion

In this chapter, we found the exact solution of WLC model of semi- flexible polymers for all possible end orientations and in both Gibbs and Helmholtz ensembles. In previous chapter, we had emphasized on the ensemble dependence of mechanical properties [42]. In this chapter we have shown that polymer properties also crucially depend on end orientations. Conditions of fixed end orientations are biologically important in several processes. Magnetic tweezer experiments can be used in laboratory to study orientation dependent properties of semi- flexible polymers. We have presented an exact theory to obtain end to end distribution function of WLC polymers by calculating the propagator for a quantum particle moving on a unit sphere. For a finite chain, the free energies in two ensembles were shown to be related via a Laplace transform relation which in thermodynamic limit goes over to the typical Legendre transform relation. Two discretized versions of WLC model have been used in MC simulations. In Helmholtz ensemble, for stiffness parameters around $t = 4$, we found multimodality (multiple minima in free energy) for all kinds of boundary orientations. Thus we have generalized the finding of triple minima in free energy that we obtained for free polymers in the previous chapter [42]. The radial distribution function of a free polymer and a polymer with a fixed orientation in one end show the same behavior. This we trace back to the properties of full distribution of end to end vector. We have calculated various projected probability distributions. The transverse fluctuation of a polymer with a fixed orientation at one end had been studied using MC simulation [43] and an effective medium theory [54] which approximately captures the qualitative features of the simulations. We have calculated this fluctuation from our theory that shows exact numerical agreement with our simulation and Lattanzi *et. al.*'s [43] simulation results. For a polymer with orientations at both its ends fixed, the end to end distribution shows dependence on relative angle θ between the two ends. The end orientations couple to the bending energy to take an unimodal distribution through bimodality with change in θ. We have seen the general presence of non- monotoinic force extension in Helmholtz ensemble. We have also studied the force- extension behavior in Gibbs ensemble. These never show non- monotonicity. It is important to note that, multiple maxima in end to end distribution means a non- monotonic force extension in Helmholtz ensemble, *not* in Gibbs ensemble. As we have shown, the response function in Gibbs ensemble is always positive, thus non-monotonicity in this ensemble is impossible. We have outlined the general theoretical framework in d- dimensions. However, in this study we have looked at the properties of a 2D polymer. At the onset we have shown that an important point of polymer statistics, multimodality, is dependent on the dimensionality of embediing space. In three dimensional free polymer, multimodality in projected probability distribution is impossible, however presence of this is a reality in 2D. Similar

studies in 3D remains to be an interesting direction forward. The presence of multimodality in intermediate range of stiffness (near $t = 4$) gives rise to a possibility of multi-stability in the dynamics of semi- flexible polymers. The simplest question remains, for a free polymer how does the presence of a triple minima in free energy affects its dynamics. This might be important in the context of understanding the time- scale of a messanger- RNA finding out an active site on a DNA chain.

4 Laser Induced Freezing and Re-entrant Melting

Reviewing Melquiades' notes, serene now, without the exaltation of novelty, in prolonged and patient sessions they tried to separate Úrsula's gold from the debris that was stuck to the bottom of the pot.   *– G. G. Márquez*

In the previous two chapters we have studied the properties of a finite semiflexible polymer in different ensembles and under different conditions of its boundary orientations. These conditions can be implemented on the polymer by imposing various kinds of external trapping and constraints. The finite size and bending rigidity of such molecules coupled with the boundary orientations rendered the different statistical and mechanical properties. In this chapter we consider another kind of trapping. A one dimensional modulating external trapping potential that couples with the local density is applied on a two dimensional system of particles interacting via various spherically symmetric short range repulsions. This trapping potential constrains the system in one direction. We find out the phase behavior of this system with change in the strength of the trapping potential. It is known that in two dimensions melting occurs by the unbinding of dislocation pairs [61–63]. How does this scenario change if there are periodic constraining potentials which may reduce the dimensionality of the system from two to one?

Examples of phase transitions mediated by the unbinding of defect pairs abound in two dimensions. The quasi- long- ranged order to disorder transition in the XY and planar rotor models[61, 64–68], the melting transition of two dimensional solid[61–63, 69–71], the super-conductor to normal phase transition in two dimensional Josephson junction arrays[72], the commensurate- incommensurate transition of the striped phase of smectic liquid crystals on anisotropic substrates[73], and the more recent discovery of a defect mediated re-entrant freezing transition in two dimensional colloids in an external periodic potential [74, 75] are all understood within such defect unbinding theories. While the very first defect mediated transition theory for the phase transition in the XY-model by Kosterlitz and Thouless (KT)[61] enjoyed almost immediate acceptance and was verified in simulations[64–66, 68] as well as experiments[76, 77], defect mediated theories of two dimensional melting took a long time to gain general acceptance in the community[78]. There were several valid reasons for this reticence however.

Firstly, as was recognized even in the earliest papers[62, 63] on this subject, the dislocation unbinding transition, which represents an instability of the solid phase, may always be pre-empted

by a first order[79, 80] transition from a metastable solid to a stable liquid. Whether such a first order melting transition actually occurs or not depends on the temperature of instability T_{KT}; so that if the transition temperature $T_c < T_{KT}$ the unbinding of dislocations does not occur. Clearly, neither this condition nor its converse can hold for all 2d systems in general. This is because T_{KT} is a non-universal number which depends on the "distance" in coupling parameter space between the bare and the fixed point Hamiltonian and hence on the details of the interaction. Secondly, the renormalization group flow equations derived in all defect mediated theories to date are perturbative expansions in the defect density (fugacity) in the ordered phase. How fast does this perturbation series converge? The answer lies again in the position of the bare Hamiltonian in the coupling parameter space. For the planar rotor model[61, 68], past calculations show that next to leading order terms in the flow equations are essential to reproduce the value of the transition temperature obtained in simulations[68]. Thirdly, defect mediated transitions predict an essential singularity[61] of the correlation length at the transition temperature. This means that effects of finite size[81] would be substantial and may thoroughly mask the true thermodynamic result. A rapid increase of the correlation length also implies that the relaxation time diverges as the transition temperature is approached – critical slowing down. For the two dimensional solid, this last effect is particularly crucial since, even far from the transition, the motion of defects is mainly thermally assisted and diffusional and therefore slow. The equilibration of defect configurations[82] is therefore often an issue even in solids of macroscopic dimensions.

On the other hand, over the last few years it has been possible to test quantitatively some of the non-universal predictions of defect mediated theories of phase transitions using simulations of restricted systems[68, 71, 83]. A simulation of a system without defects is used to obtain the values for the bare coupling constants which are then taken as inputs to the renormalization group equations for the appropriate defect unbinding theory to obtain quantities like the transition temperature. Needless to say, the simulated system does not undergo a phase transition and therefore problems typically related to diverging correlation lengths and times do not occur. Numerical agreement of the result of this calculation with that of unrestricted simulations or experiments is proof of the validity of the RG flow equations[61–63, 71]. This idea has been repeatedly applied in the past to analyze defect mediated phase transitions in the planar rotor model[68], two dimensional melting of hard disks[71] and the re-entrant freezing of hard disks in an external periodic potential [83, 84]. The last system is particularly interesting in view of its close relation with experiments on laser induced re-entrant freezing transition in charge stabilized colloids [74, 75] and this constitutes the subject of the present chapter as well.

In this chapter we show in detail how restricted simulations of systems of particles interacting among themselves via a variety of interactions and with a commensurate external periodic potential can be used to obtain phase diagrams showing the re-entrant freezing transition. The results obtained are compared to earlier unrestricted simulations for the same systems. Briefly

our results are as follows. Firstly, we observe that, as in an earlier study of the planar rotor model[68], next to leading order corrections to the renormalization flow equations are *essential* to reproduce even the gross features of the phase diagram. Specifically, the re-entrant portion of the phase diagram can be reproduced *only* if such correction terms are taken into account. Secondly while we find almost complete agreement with earlier results for the hard disk system which has been studied most extensively, our phase diagram for the other forms of interaction is shifted with respect to the results available in the literature. This may mean either of two things — inadequacy of the RG theory used by us or finite size effects in the earlier results. Lastly, as a by product of our calculations, we have obtained the core energy for defects (dislocations) in these systems and studied its dependence on thermodynamic and potential parameters.

The problem of re-entrant freezing transition of a system of interacting colloidal particles in a periodic potential has an interesting history involving experiments[74, 75], simulations[85–92] and theory[93–95]. In last couple of decades soft systems like colloids have been studied extensively[96] both for their own sake and as typical toy models to study various important condensed matter questions like structural and phase transitions through experiments that allow real space imaging. Charged colloids confined within two glass plates form a model 2-d system as the electrostatic force from the plates almost completely suppresses the fluctuations of colloids perpendicular to the plates, practically confining them to a 2-d plane. In their pioneering experiment Chowdhury[74] *et. al.* imposed a simple static background potential which is periodic in one direction and constant in the other (except for an overall Gaussian profile of intensity- variation) by interfering two laser beams. This potential immediately induces a density modulation in the colloidal system. The potential minima are spaced to overlap with the close packed lines of the ideal lattice of the colloidal system at a given density. With increase in potential strength such a colloidal liquid has been observed to solidify. This is known as laser induced freezing (LIF). In a recent experiment[75] it has been shown that with further increase in potential strength, surprisingly, the solid phase re-melts into a modulated liquid. This phenomenon is known as re-entrant laser induced freezing (RLIF). Qualitatively, starting from a liquid phase, the external periodic potential immediately induces a density modulation, reducing fluctuations which eventually leads to solidification. Further increase in the amplitude of the potential reduces the system to a collection of decoupled 1-d strips. The dimensional reduction now *increases* fluctuations remelting the system.

The early mean field theories, namely, Landau theory[74] and density functional theory[93] predicted a change from a first order to continuous transition with increase in potential strength and failed to describe the re-entrant behavior, a conclusion seemingly confirmed by early experiments[74] and some early simulations[85]. Overall, the results from early simulations remained inconclusive however, while one of them[85] claimed to have found a tri-critical point at intermediate laser intensities and re-entrance, later studies refuted these results [86–88]. All of these studies used the

change in order parameter and the maximum in the specific heat to identify the phase transition points. While some later studies[86–88] found RLIF for hard disks they reported laser induced freezing and absence of any re-entrant melting for the DLVO potential[88] in direct contradiction to experiments[75].

Following the defect mediated disordering approach of Kosterlitz and Thouless [61](KT), Frey, Nelson and Radzihovsky[94](FNR) proposed a detailed theory for the re-entrant transition based on the unbinding of dislocations with Burger's vector parallel to the line of potential minima. This theory predicted RLIF and no tricritical point. The results of this work were in qualitative agreement with experiments[75] and provided a framework for understanding RLIF in general. More accurate simulation studies on systems of hard disks[89], soft disks[91, 92], DLVO[90] etc. confirmed the re-entrant freezing-melting transition in agreement with experiments[75] and FNR theory[94, 95]. In these studies the phase transition point was found from the crossing of Binder-cumulants[5, 97] of order parameters corresponding to translational and bond- orientational order, calculated for various sub- system sizes. A systematic finite size scaling analysis[89] of simulation results for the 2-d hard disk system in a 1-d modulating potential showed, in fact, several universal features consistent with the predictions of FNR theory. It was shown in these studies that the resultant phase diagram remains system size dependent and the cross- over to the zero field KTHNY melting[62, 63] plays a crucial role in understanding the results for small values of the external potential. While the data collapse and critical exponents were consistent with KT theory for stronger potentials, for weaker potentials they match better with critical scaling[89]. A common problem with all the simulation studies might be equilibration with respect to dislocation movements along climb (or even glide) directions. Also, non universal predictions, namely the phase diagram are difficult to compare because the FNR approach (like KT theory) is expressed in terms of the appropriate elastic moduli which are notoriously time-consuming to compute near a continuous phase transition. Diverging correlation lengths and times near the phase transition further complicate an accurate evaluation of the non universal predictions of the theory.

We calculate the phase diagrams of three different 2-d systems with a 1-d modulating potential (see Fig. 6.1) following the technique of restricted Monte Carlo simulations[68, 71, 83], to be discussed below. For the laser induced transition we use this method to generate whole phase diagrams. We reject Monte Carlo moves which tend to distort an unit cell in a way which changes the local connectivity[71]. The percentage of moves thus rejected is a measure of the dislocation fugacity[71]. This, together with the elastic constants of the dislocation free lattice obtained separately, are our inputs (bare values) to the renormalization flow equations[94, 95] to compute the melting points and hence the phase diagram. Our results (Fig. 4.13,4.17,4.16) clearly show a modulated liquid (ML) $\rightarrow$ locked floating solid (LFS) $\rightarrow$ ML re-entrant transition with increase in the amplitude (V_0) of the potential. In general, we find, the predictions of FNR theory to be valid.
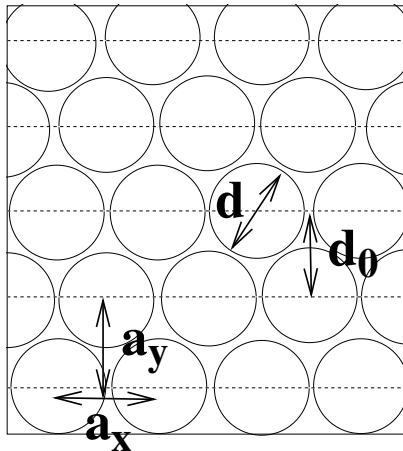
FIGURE 4.1: This cartoon shows a typical 2-d system under consideration. d is the length scale over which repulsive two body potentials are operative. The dashed lines indicate minima of external modulating potential $\beta V(y) = -\beta V_0 \cos(2\pi y/d_0)$. $a_x = a_0$ is the lattice parameter fixed by the density ρ and a_y indicate the average separation between two layers along y-direction perpendicular to a set of close-packed planes. For a perfect triangular lattice $a_y = \sqrt{3}a_0/2$. The modulating potential is commensurate with the lattice such that $d_0 = a_y$.

Lastly, we must mention that our technique, as summarized above and used in this as well as earlier[83] work, corresponds closely with early studies of the melting of the electron solid by Morf[69, 98]. In the latter case, the dislocation fugacity, which is one of the important inputs to the KTHNY flow equations was obtained by a careful and direct calculation of the dislocation core energy at $T = 0$. Our approach is somewhat cruder but gives us numbers for nonzero T which automatically contain the effects of phonon fluctuations.

In section 4.1 we first briefly discuss the FNR theory and then go on to show in detail the restricted simulation scheme used by us to obtain the various quantities required to calculate the phase diagram. In section 4.2 we give the simulation results. We describe, in detail, the various quantities leading to the phase diagram for one of the systems, viz. the hard disks[71, 99]. Then we present the phase diagrams for the other two systems we study. We compare our results with earlier simulations. Lastly, in section 5.7 we summarize our main results and conclude.

4.1 Method

A cartoon corresponding to the systems considered for our study is given in Fig. 6.1. The elastic free energy of the solid is given in terms of the spatial derivatives of the displacement field $\vec{u}(\vec{r}) = \vec{r} - \vec{r}_0$ with $\vec{r}_0$ being the lattice vectors of the undistorted reference triangular lattice.

For a solid in presence of a modulating potential $\beta V(y)$ (Fig. 6.1) the displacement mode u_y becomes massive, leaving massless u_x modes. After integrating out the u_y modes the free energy of the LFS may be expressed in terms of gradients of u_x and elastic moduli[94, 95], namely, the Young's modulus $K(\beta V_0, \rho)$ and shear modulus $\mu(\beta V_0, \rho)$,

$$\mathcal{H}_{el} = \int dxdy \left[\frac{1}{2}K \left(\frac{\partial u_x}{\partial x} \right)^2 + \frac{1}{2}\mu \left(\frac{\partial u_x}{\partial y} \right)^2 \right] \tag{4.1}$$

Similar arguments[94, 95] show that among the three sets of low energy dislocations available in the 2-d triangular lattice, only those (type I) with Burger's vector parallel to the line of potential minima survive at large βV_0. Dislocations with Burger's vector pointing along the other two possible close-packed directions (type II) in the 2-d triangular lattice have larger energies because the surrounding atoms are forced to ride the crests of the periodic potential[94, 95]. Within this set of assumptions, the system therefore shares the same symmetries as the XY model. Indeed, a simple rescaling of $x \to \sqrt{\mu}x$ and $y \to \sqrt{K}y$ leads this free energy to the free energy of the XY-model with spin-wave stiffness $K_{xy} = \sqrt{K\mu}a_0^2/4\pi^2$ and spin angle $\theta = 2\pi u_x/a_0$:

$$\mathcal{H}_{el} = \int dxdy \left[\frac{1}{2}K_{xy}(\nabla\theta)^2 \right]$$

This immediately leads to the identification of a vortex in XY model ($\oint d\theta = 2\pi$) with a dislocation of Burger's vector $\vec{b} = \hat{i}a_0$ ($\oint du_x = a_0$, $\hat{i}$ = unit vector along x- direction) parallel to the potential minima *i.e.* the dislocation of type I. The corresponding theory for phase transitions can then be recast as a KT theory[61] and is described in the framework of a two parameter renormalization flow for the spin-wave stiffness $\beta K_{xy}(l)$ and the fugacity of type I dislocations $y'(l)$, where l is a measure of length scale as $l = \ln(r/a_0)$, r being the size of the system. The flow equations are expressed in terms of $x' = (\pi \tilde{K}_{xy} - 2)$ where $\tilde{K}_{xy} = \beta K_{xy}$ and $y' = 4\pi \; exp(-\beta E_c)$ where E_c is the core energy of type I dislocations which is obtained from the dislocation probability[71, 98]. Keeping up to next to leading order terms in y' the renormalization group flow equations[68, 100] are,

$$\begin{aligned} \frac{dx'}{dl} &= -y'^2 - y'^2 x' \\ \frac{dy'}{dl} &= -x'y' + \frac{5}{4}y'^3. \end{aligned} \tag{4.2}$$

Flows in l generated by the above equations starting from initial or "bare" values of x' and y' fall in two categories. If, as $l \to \infty$, y' diverges, the thermodynamic phase is disordered (i.e. ML), while on the other hand if y' vanishes, it is an ordered phase (a LFS)[94, 95]. The two kinds of flows are demarcated by the *separatrix* which marks the phase transition point. For the linearized equations, that   keeps i only the leading order terms in y', the separatrix is simply

the straight line $y' = x'$, whereas for the full non-linear equations one needs to calculate this numerically[68, 71, 100].

The bare numbers for x' and y' are relatively insensitive to system size since our Monte Carlo simulation does not involve a diverging correlation length associated with a phase transition. This is achieved as follows[68, 71]. We monitor individual random moves of the particles in a system and look for distortions of the neighboring unit cells. If in any of these unit cells the length of a next nearest neighbor bond becomes smaller than the nearest neighbor bond, the move is rejected. All such moves generate disclination quartets and are shown in the Fig. 4.2. Notice that each of these moves break a nearest neighbour bond to build a new next nearest neighbour bond, in the process generating two 7-5 disclination pairs. These are the moves rejected in the restricted simulation scheme we follow. The probabilities of such bond breaking moves are however computed by keeping track of the number of such rejected moves. One has to keep track of all the three possible distortions of the unit rhombus with measured probabilities $P_{mi}, i = 1, 2, 3$ (see Fig. 4.2),

$$P_{mi} = \frac{\text{number of rejected bond breaking moves of type i}}{\text{Total number of MC moves}}$$

Each of these distortions involves four $7 - 5$ disclinations *i.e.* two possible dislocation- antidislocation pairs which, we assume, occur mutually exclusively in a way that we explain shortly. For a free ($V_0 = 0$) two dimensional system the dislocation core energy E_c^t can be found through the relation[98]

$$\Pi = \exp(-\beta \ 2E_c^t)Z(\tilde{K}) \tag{4.3}$$

where $\Pi = \sum_{i=1}^{3} P_{mi}$ is the total number density of dislocation pairs per particle and $Z(\tilde{K})$ is the "internal partition function" incorporating all three types of degenerate orientations of dislocations,

$$Z(\tilde{K}) = \frac{2\pi\sqrt{3}}{\tilde{K}/8\pi - 1} \left(\frac{r_{min}}{a_0}\right)^{2-\tilde{K}/4\pi} I_0\left(\frac{\tilde{K}}{8\pi}\right) \exp\left(\frac{\tilde{K}}{8\pi}\right)$$

where I_0 is a modified Bessel function, $\tilde{K} = \beta K a_0^2$ is a dimensionless Young's modulus renormalized over phonon modes, a_0 being the lattice parameter and r_{min} is the separation between dislocation-antidislocation above which one counts the pairs. The above expression for $Z(\tilde{K})$ and Eq.(4.3) have been used previously in simulations[71, 98] of phase transitions of 2-d systems in absence of any external potential to find the dislocation core energy E_c^t.

We now show how the probabilities for generating pairs of specific types of dislocations P_{di} for $V_0 \neq 0$ are related to P_{mi}. Consider Fig.4.2 where each of the three varieties of bond breaking moves are depicted. It is clear that each given distortion can occur due to the presence of two possible dislocation- antidislocation pairs acting independently. For example a distortion of type-A can take place either due to dislocation dipoles with Burgers vectors making an angle of 60°
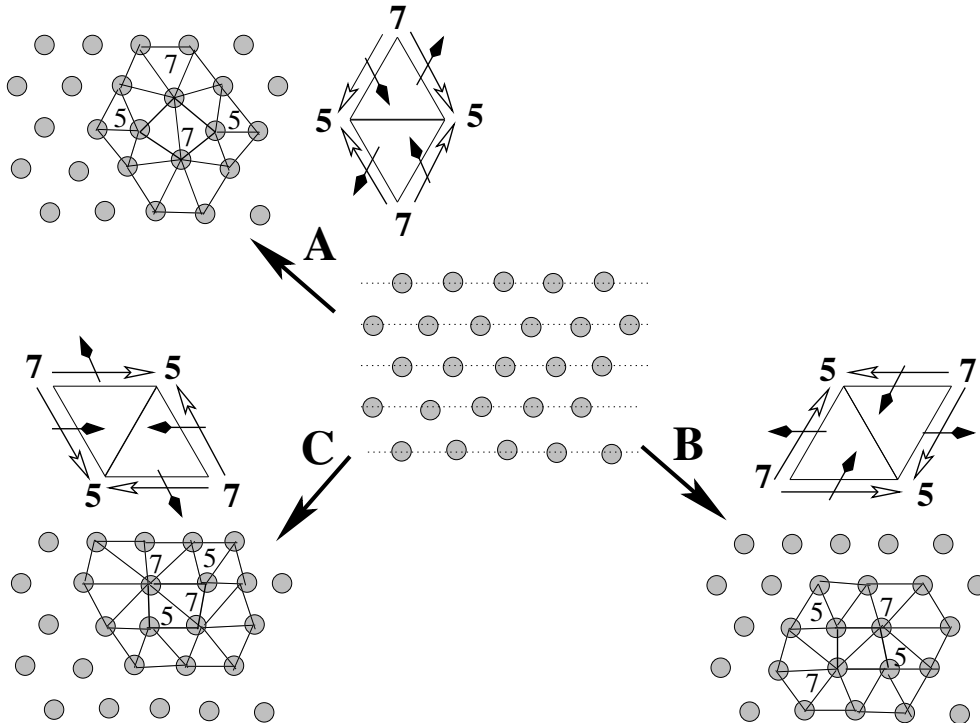
FIGURE 4.2: This diagram depicts all the possible dislocation generating moves that we reject. Starting from the triangular lattice shown in the centre (the dotted lines show the potential minima), in all, there can be three types of dislocation- pair generating moves shown as A, B & C. The numbers 7 and 5 denote the positions of two types of disclinations having seven nearest neighbours and five nearest neighbours respectively. Only those bonds, which are necessary to show distortions due to the generation of disclination quartets, have been drawn. The rhombi near each of the distorted lattice denote the unit cells and open arrows from $7 \rightarrow 5$ show the direction of dislocation generating moves. The probabilities of these moves are $P_{m1}(A)$, $P_{m2}(B)$ and $P_{m3}(C)$. Corresponding Burger's vectors (filled arrows) are bisectors pointing towards a direction rotated counter-clockwise starting from $7 \rightarrow 5$ directions and are parallel to one of the lattice planes. Notice, the separation between Burger's vectors of a pair along the glide direction (parallel to the Burger's vectors) is a single lattice separation (a_0) and within this construction it is impossible to draw Burger's loop that can generate non-zero Burger's vector. Depending on which of the two possible disclination pairs separate out any one dislocation-antidislocation pair will be formed.

with the horizontal or an angle of 120°. Both of these dislocation dipoles are of type II. If this bond breaking move were to be accepted, then at a subsequent time step the individual dislocations making up any one of the two possible pairs could separate, the two possible events being mutually exclusive. This allows us to write down the following relations among the various probabilities.

$$P_{m1} = P_{d2} + P_{d3}, \; P_{m2} = P_{d2} + P_{d1}, \; P_{m3} = P_{d3} + P_{d1}.$$

Solving for P_{di}s and remembering that $P_{d2} = P_{d3}$ by symmetry, we get $P_{d1} = \frac{1}{2}(P_{m2} + P_{m3} - P_{m1})$

and $P_{d2} = P_{m1}/2$. The above expressions are motivated and illustrated in Fig.4.2. Once the probability of dislocation pairs are obtained in this fashion, we may proceed to calculate the dislocation core energy E_c and the dislocation fugacity y'.

An argument following the lines of Fisher *et. al.*[98] shows that the dislocation probability (number density of dislocation pair per particle) for our system,

$$P_{d1} = \exp(-\beta\ 2E_c)Z(\tilde{K}_{xy}) \tag{4.4}$$

where $2E_c$ is the core energy and $Z(\tilde{K}_{xy})$ is the internal partition function of dislocation pair of type I (single orientation).

$$
\begin{aligned}
Z(\tilde{K}_{xy}) &= \int_{r>r_{min}} \frac{d^2r}{A_c} \exp\left[-2\pi\tilde{K}_{xy}\log\left(\frac{r}{a_0}\right)\right] \\
&= \frac{2\pi}{\sqrt{3}} \frac{(r_{min}/a_0)^{2-2\pi\tilde{K}_{xy}}}{\pi\tilde{K}_{xy} - 1}
\end{aligned}
\tag{4.5}
$$

with $\tilde{K}_{xy} = \beta K_{xy}$ and $A_c = \sqrt{3}a_0^2/2$ being the area of an unit cell in the undistorted lattice. We choose $r_{min} = 2a_0$. At this point this choice is arbitrary. We give the detailed reasoning for this choice at the end of the discussions on hard disks in the section 4.2. Eq.4.4 and Eq.4.5 straightaway yield the required core energy E_c. The corresponding fugacity contribution to RG flow equations (Eq.4.2) is given via

$$y' = 4\pi\sqrt{P_{d1}/Z(\tilde{K}_{xy})} \tag{4.6}$$

In the above, the following assumption is, however, implicit. Once a nearest neighbor bond breaks and a potential dislocation pair is formed, they separate with probability one [1].This assumption goes into the identity Eq.4.4 as well as in Eq.4.3[71]. Taking the rejection ratios due to bond- breaking as the dislocation probabilities, as well, require this assumption [2].

The same restricted Monte Carlo simulation can be used to find out the stress tensor, and the elastic moduli from the stress-strain curves. The dimensionless stress tensor for a free ($V_0 = 0$) system is given by[102],

$$\beta\sigma_{\lambda\nu}d^2 = -\frac{d^2}{S}\left(-\sum_{<ij>}\left\langle\beta\frac{\partial\phi}{\partial r^{ij}}\frac{r_\lambda^{ij}r_\nu^{ij}}{r^{ij}}\right\rangle + N\delta_{\lambda\nu}\right) \tag{4.7}$$

where i, j are particle indices and λ, ν denote directions x, y; $\phi(r^{ij})$ is the two- body interaction, S/d^2 is the dimensionless area of the simulation box [3].

---

[1]This assumption is similar in spirit to assuming that a particle which reaches the saddle point in the Kramers barrier crossing problem would automatically cross the barrier [101].

[2]Note that the calculation of the bare fugacity from the dislocation probability is, we believe, more accurate that the procedure used in [83].

[3]In the presence of an external 1D modulating potential periodic in the y- direction the stress has contribution from another virial- like additive term, $-\frac{\beta d^2}{S}\left\langle\sum_\lambda y^\lambda f_y^\lambda\right\rangle$, where y^λ is the y-component of position

4.2 Results and Discussion

In this section we present the results from our simulations for three different 2-d systems, namely hard disks, soft disks and a system of colloidal particles interacting via the DLVO (Derjaguin-Landau-Verwey-Overbeek)[103, 104] potentials. We discuss, first, our calculation for a two dimensional system of hard disks, in detail. The procedure followed in other systems is almost identical.

Hard disks: The bulk system of hard disks where particles i and j, in 2-d, interact via the potential $\phi(r^{ij}) = 0$ for $r^{ij} > \mathrm{d}$ and $\phi(r^{ij}) = \infty$ for $r^{ij} \leq \mathrm{d}$, where d is the hard disk diameter and $r^{ij} = |\mathbf{r}^j - \mathbf{r}^i|$ the relative separation of the particles, is known to melt[71, 99, 105–107] from a high density triangular lattice to an isotropic liquid with a narrow intervening hexatic phase[62, 63, 71, 99]. The hard disk free energy is entirely entropic in origin and the only thermodynamically relevant variable is the number density $\rho = N/V$ or the packing fraction $\eta = (\pi/4)\rho \mathrm{d}^2$. Simulations[99], experimental[96] and theoretical[108] studies of hard disks show that for $\eta > .715$ the system exists as a triangular lattice which transforms to a liquid below $\eta = .706$. The small intervening region contains a hexatic phase predicted by the KTHNY theory[62, 63] of 2-d melting. Apart from being easily accessible to theoretical treatment[109], experimental systems with nearly "hard" interactions viz. sterically stabilized colloids[96] are available.

In presence of a periodic external potential, the only other energy scale present in the system is the relative potential [4]strength βV_0. If the modulating potential is commensurate with the spacing between close- packed lines, the elastic free energy of this system in it's solid phase follows Eq.4.1 and the corresponding renormalization flow equations are given by Eq.4.2.

We obtain the bare y' and x' from Monte Carlo simulations of $43 \times 50 = 2150$ hard disks and use them as initial values for the numerical solution of Eqs. (4.2). The Monte Carlo simulations for hard disks is done in the usual[110] way viz. we perform individual random moves of hard disks after checking for overlaps with neighbours. When a move is about to be accepted, however, we look for the possibility of bond breaking as described in the previous section (Fig.4.2). We reject any such move and the rejection ratios for specific types of bond breaking moves give us the dislocation probabilities of type I and II, separately (Fig.5.12).

---

vector of particle λ. This contribution comes from the part of the free energy that involves higher energy (massive) excitations. For the elastic free energy which is lowest order in the displacement gradient (Eq.4.1) this part does not contribute towards the elastic constants, as the x- and y- component of gradient remain uncoupled. This extra term in stress remains a constant background without disturbing the elastic constants connected to the Young and shear modulus that corresponds to distortions of the system in the low energy directions. We therefore neglect this background in calculating stresses where from we obtain the elastic moduli.

[4]This interaction in colloids is due to polarization of the dielectric colloidal particles by the electric field of the laser. Though experiments of Refs.[74, 75] use charged colloids, the interaction of hard sphere colloids with lasers is similar.
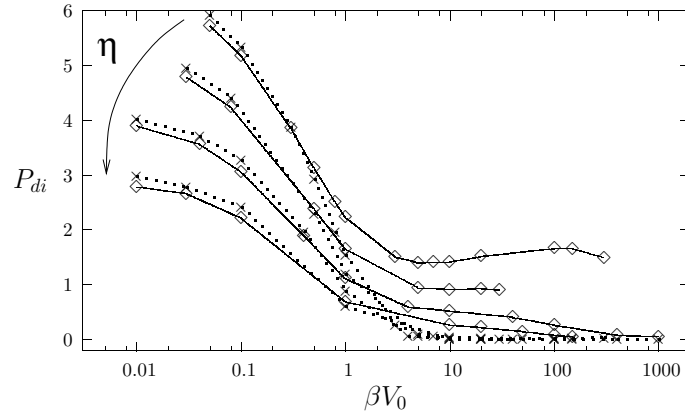
FIGURE 4.3: Number density of dislocation pairs of type I and II per particle as a function of the amplitude of the laser potential βV_0. In this plot the $\diamond$ symbols correspond to P_{d1}, the probability for type I dislocations and the $\times$ symbols to P_{d2} the probability for type II dislocations obtained from the P_{mi} (see text and Fig.4.2) for various η values, arrow denoting the direction of increasing $\eta(= .69, .696, .7029, .71)$. The P_{di} for $i = 1, 2$ are multiplied by 10^4. These probabilities are plotted against the potential strength βV_0. Note that for $\beta V_0 > 1$, the probability for type I dislocations is larger than that of type II. The dots and solid lines are only guides to eye.

From Fig.5.12 it is clear that the probability of type II dislocations *i.e.* P_{d2} drops down to zero for all packing fractions at higher potential strengths βV_0. The external potential suppresses formation of this kind of dislocations. For small βV_0 on the other hand, the probabilities of type I and type II dislocations are roughly the same. This should be a cause of concern since we neglect the contribution of type II dislocations for *all* βV_0. We comment on this issue later in this section. Using Eq.4.6 and Eq.4.5 along with the identity $r_{min} = 2a_0$ gives us the initial value y_0' to be used in renormalization flow Eq.4.2.

Before we move on, we comment on the magnitude of the errors for P_{mi} and hence for y_0'. There are two main sources of errors for these quantities. This may arise from (a)finite simulation times and (b)small size of the system. In order to check for this, we have plotted the accumulated values for the probability P_{d1} as a function of Monte Carlo step for 2150 and 21488 hard disks (Fig.4.4). It is clear that our estimates for the probabilities are virtually error free! This demonstrates clearly the usefulness of our restricted Monte Carlo scheme.

To obtain K_{xy} we need to calculate the Young's modulus K and shear modulus μ. In order to do that consider Eq.4.7, the expression for stress tensor. For hard disk potentials the derivative $\partial\phi/\partial r^{ij}$ becomes a Dirac delta function and the expression for stress can be recast into[102]

$$\beta\sigma_{\lambda\nu}\mathrm{d}^2 = -\frac{\mathrm{d}^2}{S}\left(\sum_{<i,j>}\left\langle\frac{r_\lambda^{ij}r_\nu^{ij}}{r^{ij}}\delta(r^{ij}-d)\right\rangle + N\delta_{\lambda\nu}\right) \tag{4.8}$$

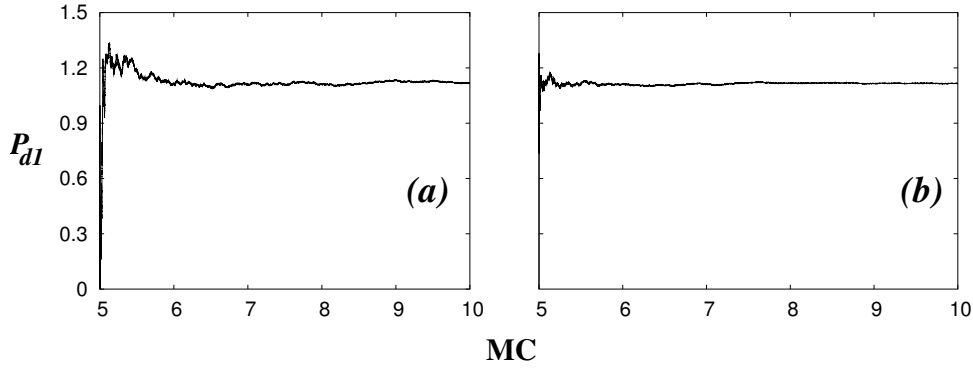The presence of the Dirac delta function $\delta(r^{ij}-d)$ in the above expression requires that the terms

FIGURE 4.4: P_{d1} as a function of MC steps. P_{d1} has been multiplied by 10^4 and MC steps has been multiplied by 10^{-4} for clarity. The data have been collected for $\eta = .7029$ and $\beta V_0 = 1$. Panel (a) is for system size of 2150 particles whereas (b) for 21488 particles. Within 10^5 MC steps all fluctuations die out. Clearly, the dependence of the dislocation number density on the system sizes and the Monte Carlo errors are negligible. To calculate dislocation fugacity we use averaging of data between 5×10^5 to 10^6 MC steps.
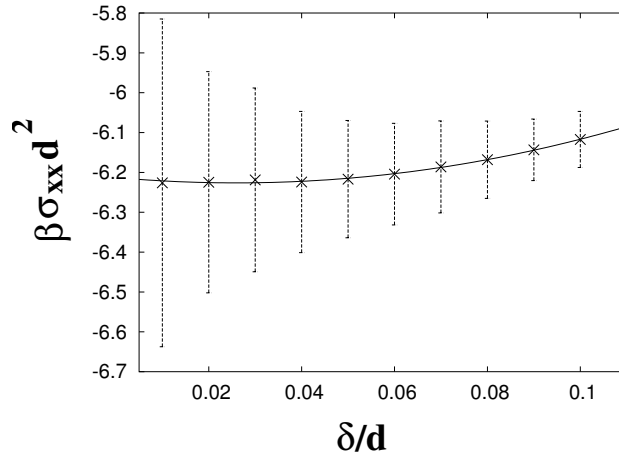
FIGURE 4.5: Plot of $\beta d^2 \sigma_{xx}$ vs. δ/d at a strain value $\epsilon_{xx} = .02$ for packing fraction $\eta = .7029$ and potential strength $V_0 = 1$. A second order polynomial fit (solid line) utilizing the error bars to assign weights to each data points gives $\lim_{\delta \to 0} \beta d^2 \sigma_{xx} = -6.21$ with an error within .08%.

under the summation contribute, strictly, when two hard disks touch each other *i.e.* $r^{ij} \equiv r = \sigma$. In practice, we implement this, by adding the terms under summation when each pair of hard disks come within a small separation $r = \sigma + \delta$. We then find $\beta \sigma_{\lambda\nu} \mathrm{d}^2$ as function of δ and fit the curve to a second order polynomial. Extrapolating to the $\delta \to 0$ limit obtains the value of a given component of stress tensor at each strain value $\epsilon_{\lambda\nu}$[102](Figs 4.5,4.7).

For completeness, now we show how we calculate the two relevant elastic moduli from the
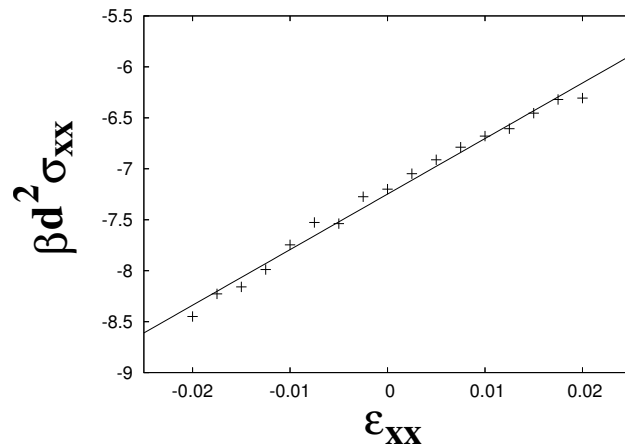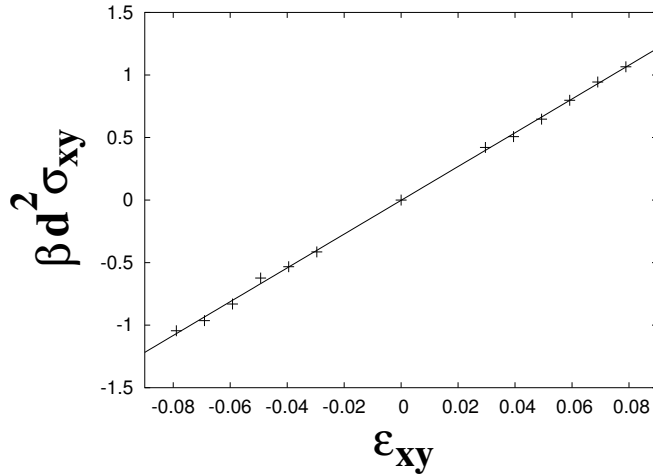
FIGURE 4.6: A typical stress-strain curve used to obtain the Young's modulus from a linear fit (solid line). The graph is plotted at $\eta = .7029$, $V_0 = 1.0$. The fitted Young's modulus $\beta K \mathrm{d}^2 = 54.5$ with an error within 2.9%. The error bars in stress are less than $.2\%$ and much smaller than the point sizes plotted in this graph.
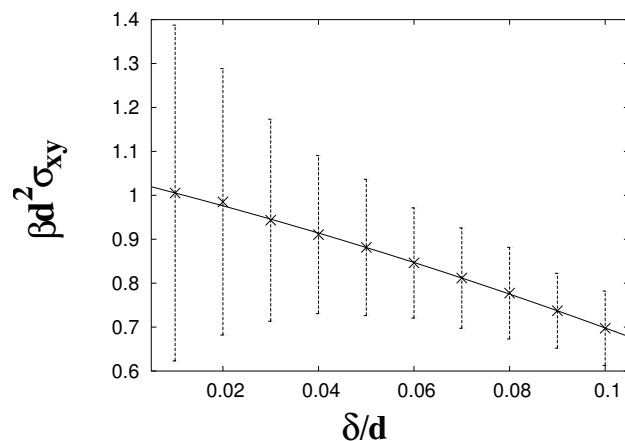
FIGURE 4.7: Plot of $\beta d^2 \sigma_{xy}$ vs. δ/d at strain value $\epsilon_{xy} = .079$ at the packing fraction $\eta = .7029$ and potential strength $V_0 = 1$. A second order polynomial fit (solid line) gives $\lim_{\delta \to 0} \beta d^2 \sigma_{xy} = 1.033$ with an error within $.5\%$.

stresses : σ_{xx} at a given longitudinal strain ϵ_{xx} (Fig. 4.5) and σ_{xy} for a shear strain ϵ_{xy} (Fig. 4.7). All the data points are from our MC simulations averaged between $10,000$-$20,000$ MC steps. Increasing the number of configurations does not change the values significantly. The total errors arising from the MC simulations and the fit for a typical calculation of stresses is less than a percent. We thus calculate the stress at each value of strain and from the slopes of stress-strain curves find out the bare Young's modulus $\beta K \mathrm{d}^2$ (Fig. 4.6) and shear modulus $\beta \mu \mathrm{d}^2$ (Fig. 4.8).

FIGURE 4.8: A typical stress-strain curve used to obtain shear modulus from a linear fit (solid line). The graph is plotted at $\eta = .7029$, $V_0 = 1.0$. The fitted shear modulus $\beta\mu\mathrm{d}^2 = 13.5$ with an error within .9%. The error bars in stress are less than .5% and much smaller than the point sizes plotted in this graph.

We impose an elongational strain in x- direction which is parallel to the direction of potential minima to obtain $\beta K\mathrm{d}^2$. Imposition of a shear strain in the same direction gives us $\beta\mu\mathrm{d}^2$. Any strain that forces the system to ride potential hills will give rise to massive displacement modes which do not contribute to elastic theory. Our results for the stress strain curves for obtaining $\beta K\mathrm{d}^2$ and $\beta\mu\mathrm{d}^2$ are shown in Figs 4.6,4.8 respectively. Note that the errors for the calculation of the elastic constants arise solely from the fitting of the stress- strain curves. These can be made as small as possible by increasing the number of strain values at which the stresses are calculated. The values of the stress are also free from any residual finite size effects which we checked by simulating systems of sizes 10×10 to 136×158. From these elastic moduli we get the 'bare' $\tilde{K}_{xy}$ (and hence $x'_0 = \pi\tilde{K}_{xy} - 2$, see section 4.1). Our final estimate for the 'bare' $\tilde{K}_{xy}$ are also correct to within a percent.

In Ref.[95] it is argued that the elastic constant $\beta K\mathrm{d}^2$ remains more or less independent of amplitude of the laser potential βV_0, while the shear modulus decreases linearly with increasing βV_0 for large βV_0. In figures 4.9 and 4.10 we have plotted the values of $\beta K\mathrm{d}^2$ and $\beta\mu\mathrm{d}^2$ respectively as a function of βV_0. It is apparent that the expectations of Ref.[95] are borne out by our data. Incidentally, the behaviour of $\beta K\mathrm{d}^2$ and $\beta\mu\mathrm{d}^2$ with increasing βV_0 offers an intuitive interpretation of the RLIF transition which we offer below.

In Fig. 4.11 we have plotted x'_0 and y'_0 the bare values of x' and y' for various potential strengths βV_0 at packing fraction $\eta = .7029$ along with the separatrices for the linearized and
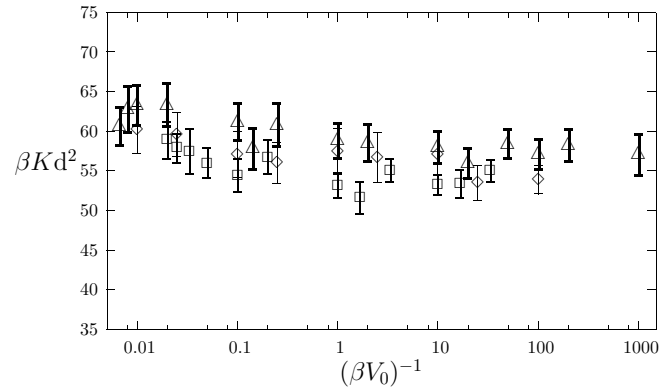
FIGURE 4.9: Young's modulus $\beta K d^2$ as a function of inverse laser potential $(\beta V_0)^{-1}$. Various symbols denote different densities − $\diamond$ denotes $\eta = .7029$, $\triangle$ denotes $\eta = .705$ and $\square$ denotes $\eta = .7$. The data for Figs 4.9 and 4.10 were obtained from a separate run with a slightly higher error than that in Figs. 4.6 and 4.8.
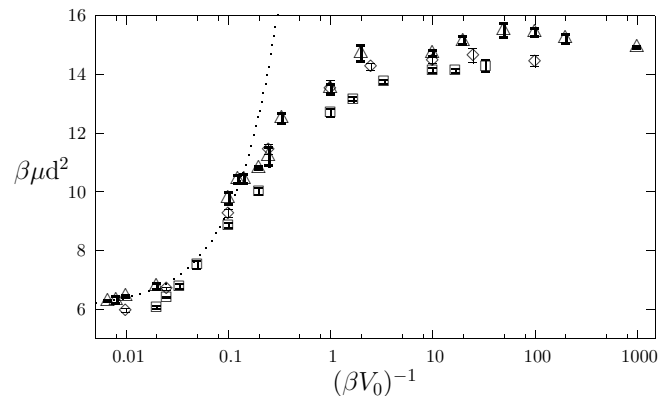

FIGURE 4.10: Shear modulus $\beta \mu d^2$ as a function of inverse laser potential $(\beta V_0)^{-1}$. Various symbols denote different densities − $\diamond$ denotes $\eta = .7029$, $\triangle$ denotes $\eta = .705$ and $\square$ denotes $\eta = .7$. The dotted line is a linear fit of the form $\beta \mu d^2 = a/\beta V_0 + b$ in the large βV_0 limit[95].

the non-linear flow equations (Eq. 4.2). The line of initial conditions is seen to cross the non-linear separatrix twice (signifying re-entrant behaviour) while crossing the corresponding linearized separatrix only once at high potential strengths. For small βV_0 the freezing transition is seen to be driven mainly by the decrease of y' (the dislocation density) since $\beta K d^2$ and $\beta \mu d^2$ are virtually constant. For large βV_0, the shear modulus $\beta \mu d^2$ vanishes and this results in the second point of intersection with the separatrix (remelting). The phase diagram (Fig. 4.13) is obtained by computing the points at which the line of initial conditions cut the non-linear separatrix using a simple interpolation scheme. It is interesting to note that within a linear theory the KT flow
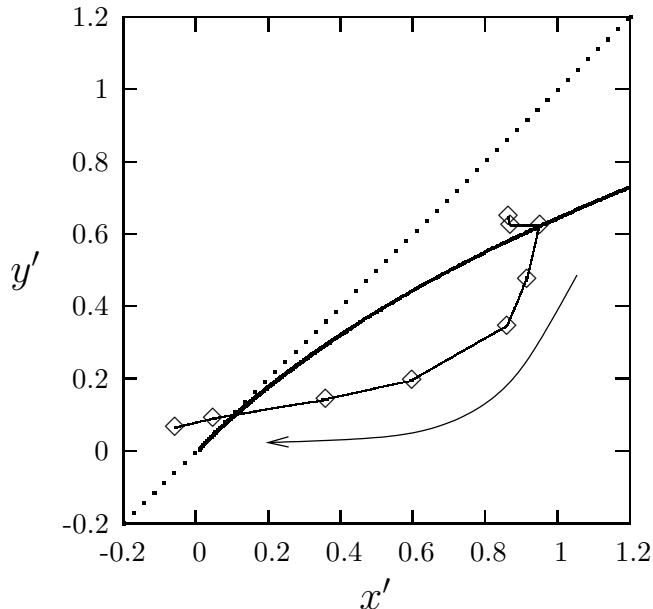
FIGURE 4.11: The initial values of x' and y' obtained from the elastic moduli and dislocation probability at $\eta = .7029$ plotted in $x' - y'$ plane. The line connecting the points is a guide to eye. The arrow shows the direction of increase in $\beta V_0 (= .01, .04, .1, .4, 1, 4, 10, 40, 100)$. The dotted line denotes the separatrix $(y' = x')$ incorporating only the leading order term in KT flow equations. The solid curve is the separatrix when next to leading order terms are included. In $l \to \infty$ limit any initial value below the separatrix flows to $y' = 0$ line whereas that above the separatrix flows to $y' \to \infty$. The intersection points of the line of initial values with the separatrix gives the phase transition points. The plot shows a freezing transition at $\beta V_0 = .1$ followed by a melting at $\beta V_0 = 30$.

equations *fail to predict a RLIF transition*. Performing the same calculation for different packing fractions η we find out the whole phase diagram of RLIF in the η- βV_0 plane.

Small, residual numerical errors in x'_0 and y'_0 translate into errors in the location of the phase transition points. These are calculated as follows. The quantity βK_{xy} varies linearly with η at all potential strengths. Therefore the numerical error in η is proportional to the error in βK_{xy} (see Fig. 4.12). The error in y'_0 is neglected [5]. The final error estimates are shown (as vertical error bars) in our results for the phase diagram of hard disks in an external potential in Fig.4.13.

Comparing with previous computations[88, 89] of the phase diagram for this system (also shown in Fig. 4.13) we find that, within error- bars, our results agree at all values of η and βV_0 with the results of Strepp *et. al.* [89]. In numerical details, they, however, disagree with the results of C. Das *et. al.*[88], though even these results show RLIF and are in qualitative agreement with ours. This validates both our method and the quantitative predictions of Ref. [94, 95].

---

[5]The error in y'_0 has contributions from both P_{di}s and from K_{xy} while the former is practically zero, the contribution from the latter is neglected in this work.
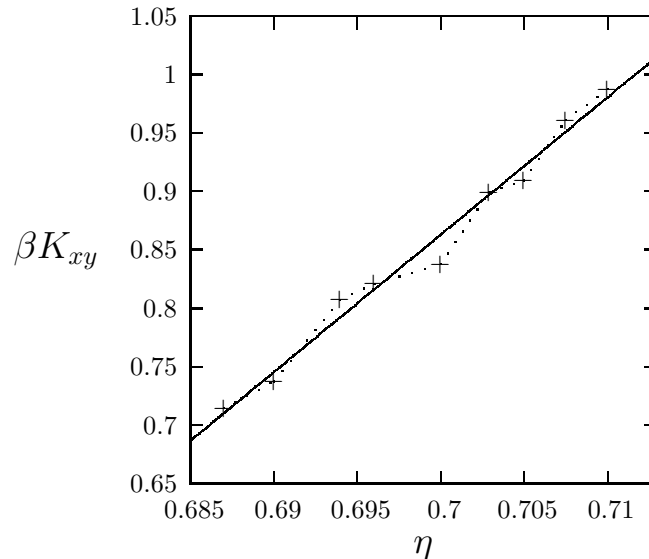
FIGURE 4.12: For hard disk system $\tilde{K}_{xy} = \beta K_{xy}$ varies linearly with η. Data plotted at $V_0 = 1$. The solid line is a linear fit to the form $f(x) = a + bx$ with $a = -7.37$ and $b = 11.76$. At each V_0 the error in $\tilde{K}_{xy}$ determines the error in η: $\delta\eta/\eta = |1 + a/\eta b|(\delta\tilde{K}_{xy}/\tilde{K}_{xy})$.

The effect of higher order terms in determining non-universal quantities has been pointed out earlier[68] for the planar rotor model but in the present case their inclusion appears to be crucial. Nevertheless, we expect our procedure to break down in the $\beta V_0 \to 0$ limit where effects due to the cross-over from a KT to a KTHNY[62, 63] transition at $\beta V_0 = 0$ become significant. Indeed, as is evident from Fig. 5.12 for $\beta V_0 < 1$ the dislocation probabilities of both type I and type II dislocations are similar [6] and the assumptions of FNR theory and our process (which involves only type I dislocations) need not be valid at small potential strengths. This fact is also supported by Ref.[89] where it was shown that though at $\beta V_0 = 1000$ the scaling of susceptibility and order parameter cumulants gave good data collapse with values of critical exponents close to FNR predictions, at $\beta V_0 = .5$, on the other hand, ordinary critical scaling gave better data collapse than the KT scaling form, perhaps due to the above mentioned crossover effects. In the asymptotic limit of $\beta V_0 \to \infty$ the system freezes above $\eta = .706$ which was determined from a separate simulation in that limit. This number is very close to the earlier value $\eta \sim .71$ quoted in Ref.[89]. As expected, the freezing density in the $\beta V_0 \to \infty$ limit is lower than the value without the periodic potential *i.e.* $\eta \simeq .715$.

Before we go on to discuss other systems, we discuss the reasons behind the particular choice

---

[6]In analysing Fig.3 we must keep in mind that we can calculate from our simulations only the probability of formation of a disclination quartet. While we can, perhaps, safely assume that if type I dislocations are involved, they will seperate out with unit probability, the same can not be said of type II dislocations. This means that the probability of type II dislocations could be much lower than what Fig.3 suggests.
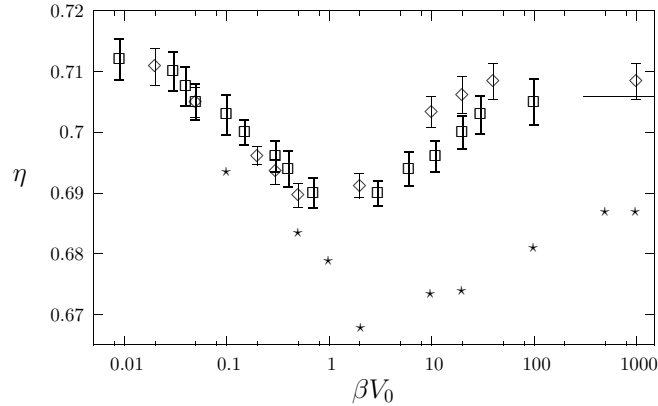
FIGURE 4.13: The phase diagram of the hard disk system in the presence of a 1-d, commensurate, periodic potential in the packing fraction (η) - potential strength (βV_0) plane. The points denoted by $\square$ correspond to our RG calculation using the techniques described in this chapter. The points denoted by $\diamond$[89] and $*$[88] are taken from earlier simulations. The vertical bars denote estimate of error. Our data clearly matches with Ref[7].The horizontal line at $\eta = .706$ denotes the calculated asymptotic phase transition point at $\beta V_0 = \infty$.

of r_{min} that we made throughout this work. After a disclination quartet is formed, they get separated out and the easy direction of separation is the glide direction which is parallel to the Burger's vector. In Fig.4.14 we show four steps of separation of such a dislocation pair of type I. It is clear that, it is possible to give individual identification to a dislocation only when the Burger's vector separation within a pair is $\geq 2a_0$ (Fig.4.14) i.e. $r_{min} = 2a_0$. For $r \geq 2a_0$ Burger's loops can be drawn around each $5 - 7$ disclination pair (Fig.4.14) giving rise to a non-zero Burger's vector. After motivating $r_{min} = 2a_0$ we show, in Fig.4.15, the three sets of initial values corresponding to $r_{min} = a_0, \ 2a_0, \ 3a_0$ along with the non-linear separatrix at $\eta = .7029$ of hard disk system. It is clear from the figure that $r_{min} = a_0$ predicts the system to be in the solid phase for any arbitrarily small amount of external potential and to melt at larger βV_0. This behaviour contradicts physical expectation that the melting density at $\beta V_0 = 0$ has to be larger than that at $\beta V_0 = \infty$. On the other hand, while $r_{min} = 3a_0$ does not produce any unphysical prediction, it shrinks the region of re-entrance in the βV_0 direction. It is therefore satisfying to note that $r_{min} = 2a_0$, the minimum possible value for the separation between members of a dislocation- antidislocation pair which allows unambiguous identification also produces physically meaningful results for the phase diagram in closest agreement with earlier simulation data.

It is possible to find out phase diagrams of any 2-d system in presence of external modulating potential commensurate with the density of the system in a similar fashion. We illustrate this by calculating similar phase diagrams for two other systems, viz. soft disks and the DLVO system.
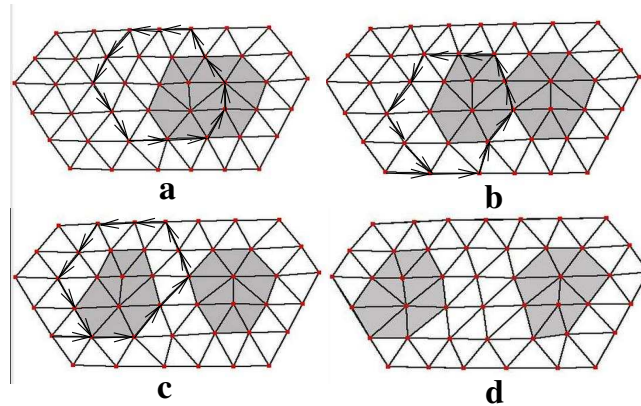
FIGURE 4.14: The figures a – d which we have drawn using the applet "voroglide"[111] show four steps of separation of a type I dislocation pair, from a separation of a_0 to $4a_0$. The shaded regions show the $5 - 7$ disclination pairs constituting the dislocations. Burger's circuits are shown in a – c. Note that for separations $\geq 2a_0$ separate Burger's circuits around each disclination pair give rise to non-zero Burger's vectors, giving the dislocations their individual identity. This shows that the minimum meaningful separation between dislocation cores $r_{min} = 2a_0$.

Soft disks: Soft disks interact via the potential :

$$\phi(r) = \frac{1}{r^{12}}$$

where r denotes the separation between particles. In simulations, the cutoff distance is chosen to be $r_c = 2$ above which the particles are assumed to be non- interacting. Apart from the external potential strength βV_0 the relevant thermodynamic quantity is the number density $\rho = N/L_x L_y$. To obtain 'bare' elastic moduli from restricted simulations the stress is calculated using Eq.4.7. As this expression does not involve any Dirac delta functions (unlike hard disks), we do not require any fitting and extrapolation to obtain the stresses and the errors are purely due to random statistical fluctuations in our MC simulations. The elastic moduli are again found from stress-strain curves like Figs.4.6,4.8. The dislocation fugacity of type I is calculated from rejection ratio of dislocation generating moves. All these, at a given ρ value generate the initial conditions x'_0 and y'_0 in RG flow diagrams. Again, the crossing of these initial conditions with the separatrix found from Eq.4.2 gives the phase transition points. The phase diagram is plotted and compared with phase diagram from earlier simulations[91, 92] in Fig.4.16. The error bar in ρ is found from the error in $\tilde{K}_{xy}$, as $\tilde{K}_{xy}$ varies linearly with ρ, through the relation $\delta\rho/\rho = |1+a/\rho b|(\delta\tilde{K}_{xy}/\tilde{K}_{xy})$ where a and b are obtained from a linear $(a + bx)$ fit of the $\tilde{K}_{xy}$ vs. ρ curve, at any given βV_0. The phase diagram (Fig. 4.16) again clearly shows re-entrance (RLIF). This is in qualitative agreement with earlier simulations[91, 92] (see Fig.4.16).

DLVO: For charge stabilized colloids the inter-particle potential that operates is approximately
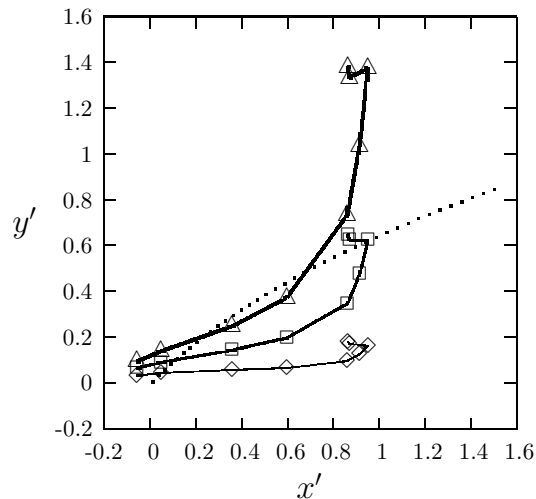
FIGURE 4.15: Similar to Fig.4.11. The initial conditions x'_0 and y'_0 are plotted as a function of βV_0. The different data sets are created for different values of r_{min}. The symbols mean the following : $\Diamond$ denotes data for $r_{min} = a_0$, $\square$ denotes that for $r_{min} = 2a_0$ and $\triangle$ denote data for $r_{min} = 3a_0$. The dotted line denotes the non- linear separatrix.
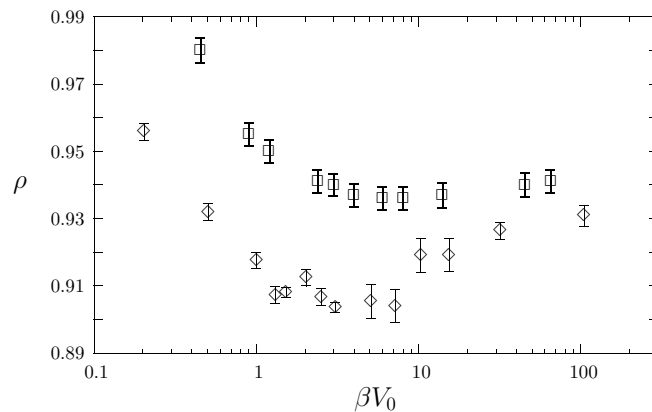

FIGURE 4.16: Phase diagram for soft disks: $\square$ denote our calculation, $\Diamond$ indicate earlier simulation data[91, 92]. The vertical lines are the error- bars.

given by the DLVO potential [103, 104]:

$$\phi(r) = \frac{(Z^*e)^2}{4\pi\epsilon_0\epsilon_r} \left(\frac{exp(.5\kappa \mathrm{d})}{1 + .5\kappa \mathrm{d}} \right)^2 \frac{exp(-\kappa r)}{r}$$

where r is the separation between two particles, d is the diameter of the colloids, κ is the inverse Debye screening length, Z^* is the amount of effective surface charge and ϵ_r is the dielectric constant of the water in which the colloids are floating. In order to remain close to experimental
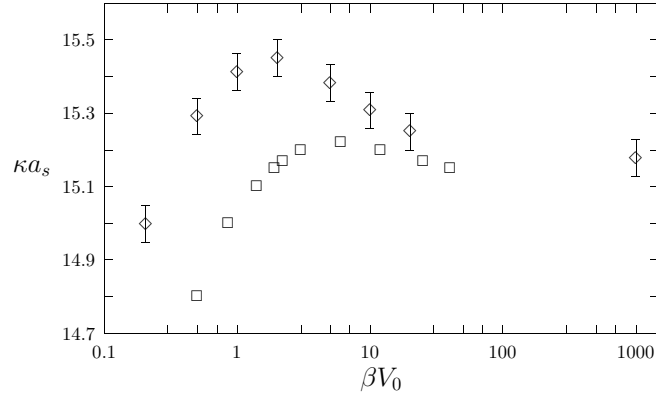
FIGURE 4.17: Phase diagram for particles interacting via the DLVO potential. □ denote our calculation, ◊ show the earlier simulation data[90]. The vertical lines are the error- bars. Error bars in our calculation being smaller than the symbol size are not shown.

situations and to be able to compare our phase diagram with the simulations of Strepp et. al.[89] we use $T = 293.15K$, d$= 1.07\mu m$, $Z^* = 7800$, $\epsilon_r = 78$. In experiments, the dimensionless inverse Debye screening length κa_s can be varied either by changing κ through the change in counter-ion concentration or by changing a_s by varying density[112]. In our restricted MC simulations we vary κ keeping the density fixed at $0.18\mu m^{-2}$ by fixing the lattice parameter of the in ital configuration of ideal triangular lattice at $a_s = 2.52578\mu m$. Further, we use a cut-off radius r_c such that, $\phi(r > r_c) = 0$ where r_c is found from the condition $\beta\phi(r_c) = .001$. We find out phase transition points (in κa_s) at different external potential strengths βV_0 in the same fashion as described earlier. The phase diagram in $\kappa a_s - \beta V_0$ plane is shown in Fig. 4.17. To obtain error bars in this case we note that $\tilde{K}_{xy}$ varies linearly with κa_s and therefore the error in $\tilde{K}_{xy}$ is proportional to the error in κa_s (Fig.4.17) through the relation $\delta(\kappa a_s)/(\kappa a_s) = |1 + a/b\kappa a_s|(\delta\tilde{K}_{xy}/\tilde{K}_{xy})$. The quantities a and b are found from fitting $\tilde{K}_{xy}$ to a linear form of κa_s, at any given βV_0.

Though there is a quantitative mismatch between our data and that of Strepp *et. al.*[90], our data shows a clear region in κa_s (between 15.1 and 15.2) where we obtain re-entrance (RLIF). This is in contrast to the simulated phase diagram of C. Das *et. al.*[88], where they observe absence of re-entrance at high field strengths. We do not plot their data as the parameters these authors used are not the same as the ones used in Fig.4.17.

It is interesting to note that, with increase in the range of the two- body interaction potentials the depths of re-entrance (in η, ρ or κa_s) decreases. This is again in agreement with the understanding that, the re-entrant melting comes about due to decoupling of the 1-d trapped layers of particles that reduces the effective dimensionality thereby increasing fluctuations. With

an increase in range of the interacting potentials this decoupling gets more and more suppressed, thereby reducing the region of re-entrance.

One aspect of our study which stands out is the exceptionally better agreement of our results with previous simulations for hard disks as opposed to systems with soft potentials like the soft disks and the DLVO. This could, in principle, be due either (a) to the failure of the RG equations used by us or some other assumptions in our calculations (b) or to unaccounted finite size effects in earlier simulations. While it is difficult to estimate the effect of (a) since RG equations to higher orders in y are unknown at present, we may be able to motivate an estimation for (b). In order to explain the discrepancy in the positions of the phase boundaries, we need to go into some details of how the phase diagrams were obtained in the earlier simulations. In these simulations [89–92] the phase boundaries were obtained   from the crossing of the order parameter cumulants [5, 97] for various coarse graining sizes. The system sizes simulated in these studies are the same ($N = 1024$). However, the range of interaction differs. To obtain an objective measure we define the range of the potentials ξ as that at which the interaction potential ϕ is only 1% of its value at the lattice parameter. In units of lattice parameter, we obtain, for soft disks $\xi = 1.47$ and for the DLVO potential $\xi = 1.29$ at typical screening of $\kappa a_s = 15$. By definition, for hard disks $\xi = 1$. The particles within the range of the potential are highly correlated and we calculate the number N_{corr} of such independent bare *uncorrelated particles* within the full system size. N_{corr} takes the values $N_{corr} = 1024,\ 473.88,\ 615.35$ for hard disks, soft disks and the DLVO potential respectively. Since the effective system sizes are smaller for the soft potentials, finite size effects are expected to be larger. In this connection, it is of interest to note that in the same publications [89–92] a systematic finite size analysis showed that the phase diagrams shift towards higher (lower) density (kappa) for hard and soft disks (DLVO). A look at Fig.4.16 and 4.17 should convince the reader that such a shift would actually make the agreement with our results better. We emphasize here that our present restricted simulations are virtually free of finite size effects since the system does not undergo any phase transition.

4.3 Conclusion

We have presented a complete numerical renormalization group scheme to calculate phase diagrams for 2-d systems under a commensurate modulating potential. We have used FNR theory along with this scheme to calculate phase diagrams for three different systems, namely, the hard disks, the DLVO and the soft disks. In all the cases we have found laser induced freezing followed by a re-entrant laser induced melting. We show that the re-entrance behavior is built into the 'bare' quantities themselves. We find extremely good agreement with earlier simulation results. In particular the phase diagram for hard disk comes out to be exactly the same as found from one set of earlier simulations[89].To obtain the correct phase diagram, however, flow equations

need to be correct at least upto next to leading order terms in the dislocation fugacity. Our results, especially for small potential strengths, is particularly sensitive to these terms. Cross-over effects from zero potential KTHNY melting transition are also substantial at small values of the potential.

In this chapter we have studied the phenomena of RLIF, that comes about due to a confining potential which is constant in one direction and modulating in the other. In next chapter we shall study the effect of another kind of confinement. We shall confine a two dimensional solid in a narrow but long channel and will find out its properties, phases, strain induced failure and phase diagram.

5 Confined Solid: Phases and Failure

One afternoon the boys grew enthusiastic over the flying carpet that went swiftly by the laboratory at the window level . . .   – *G. G. Márquez*

In the last chapter we studied phase transitions in a two dimensional solid driven by a periodic confining potential which caused a dimensional crossover from two to one dimension as the amplitude of the periodic potential was increased. In this chapter we study the effect of a different kind of external potential which forces a system of "hard-disk" atoms to remain in-between one and two dimensions. Specifically, we consider here the mechanical and thermodynamic properties of a narrow strip of crystalline solid with one dimension much longer than the other other i.e. a quasi one dimensional (Q1D) system. In the short dimension, the solid is confined by hard, featureless walls.

We shall show in this chapter, that such a Q1D solid strip has rather anomalous properties, which are quite different from bulk one, two or three dimensional systems. The Q1D solid is shown to have a non zero Young's modulus which offers resistance to tensile deformations and approximate two dimensional hexagonal crystalline order. On the other hand, the shear modulus of the system is vanishingly small. Large wavelength displacement fluctuations are seen to destabilize crystalline order beyond a certain length scale at low densities. At high densities these fluctuations appear to be kinetically suppressed. The failure properties of this quasi solid is also rather interesting. In the constant extension (Helmholtz) ensemble, the initial rise in the tensile stress with tensile loading is interrupted at a limiting value of strain and on further extension the stress rapidly falls to zero accompanied by a reduction in the number of solid layers parallel to the hard wall by one. However, this failure is reversible and the system completely recovers the initial structure once the strain is reduced. The critical strain for failure by this novel mechanism, for small channel widths, decreases with increase in channel width so that thinner strips are *more* resistant to failure. We have used an idealized model solid to illustrate these phenomena. Our model solid has particles (disks) which interact among themselves only through excluded volume or "hard" repulsion. We have reasons to believe, however, that for the questions dealt with in this chapter, the detailed nature of the inter particle interactions are relatively irrelevant and system behaviour is largely determined by the nature of confinement and the constraints. Our results may be directly verified in experiments on sterically stabilized "hard sphere" colloids[96] confined in glass

channels and may also be relevant for similarly confined atomic systems interacting with more complex potentials. We have also speculated on applications of this reversible failure as accurate strain transducers or strain induced electrical or thermal switching devices. In the next chapter we shall study thermal transport across this Q1D solid, especially with respect to the effects of reversible failure on the transport coefficients.

Studies of small assemblages of molecules with one or more dimensions comparable to a few atomic spacings are significant in the context of nano-technology[113, 114]. Designing nano-sized machines requires a knowledge of the mechanical behavior of systems up to atomic scales, where, a priori, there is no reason for our ideas, derived from macroscopic continuum elasticity theory, to be valid[115]. Small systems often show entirely new behaviour if hard constraints are imposed leading to confinement in one or more directions. Consider, for example, the rich phase behaviour of quasi two-dimensional colloidal solids [116–121] confined between two glass plates showing square, triangular and "buckled" crystalline phases and a, recently observed, re-entrant surface melting transition[122] of colloidal hard spheres not observed in the bulk[71, 99, 105–107].

Recent studies on various confined Q1D systems have shown many different structures depending on the range of interactions and commensurability of the natural length scale of the system with the length scale of confinement [123, 124]. These structures play crucial role in determining the local dynamical properties like asymmetric diffusion, viscosity etc. and phase behaviour [125]. A study by G. Piacente *et. al.* [123] on confined charged particles interacting via the screened Coulomb potential and confined in one direction by a parabolic potential showed many zero temperature layering transitions, i.e. change in the number of layers with a change in density or range of interaction. This also showed regions where these transitions were reentrant [123]. Apart from the transition from one to two layers, all these layering transitions were shown to be first order [123]. At high temperature this classical Wigner crystal melts and the melting temperature shows oscillations as a function of density [123]. Such oscillations are charecteristic of confined systems, arising out of commensurability. Confined crystals always align one of the lattice planes along the direction of confinement [123, 124] and confining walls generate elongational asymmetry in the local density profile along the walls even for the slightest incommensuration. A study by R. Haghgooie *et. al.* on a system of purely repulsive dipoles confined in Q1D hard channel showed layering transitions mediated via an order- disorder transition near the centre of the channel [124]. All the structural properties showed oscillations as the channel width increased [124]. Wall induced layering was also observed in a dusty-plasma study by L.-W. Teng *et. al.* [126] and in shell structures in circular confinements [127–131]. A similar layering transition, in which the number of smectic layers in a confined liquid changes discretely as the wall-to-wall separation is increased, was noted by P. G. deGennes [132] and J. Gao *et. al.* [133]. J. Gao *et. al.*'s study also revealed the relations between the local layering structures and dynamical quantity like diffusion constant [133]. deGennes and Gao *et. al.*'s work also calculated the wall to wall force due to

this smectic layering and its commensurability with channel width. For long ranged interactions extreme localization of wall particles has been observed in studies of V. M. Bedanov *et. al.* [127] and R. Haghgooie *et. al.* [124]. In an earlier experiment on confined steel balls in Q1D vibrated to simulate the effect of temperature, layering transition, phase coexistance and melting was observed by P. Pieranski *et. al.* [134]. Confinement, in general, can lead to new behaviours in various systems and processes. Schmidt and Lowen [120] studied the phase behaviour of a collection of hard spheres confined within a two dimensional slit defined by two parallel hard plates. Plate separations such that upto two layers of solid are accomodated were considered by these authors. Recently Fortini and Dijkstra studied the same system for separations of one to five hard sphere diameters to find a rich phase diagram consisting of a dazzling array of upto 26 distinct crystal structures[121]. Similar studies had been carried out long back in 1983 by Pieranski and his group [116] to find out many of the structures identified by Fortini *et. al.* [121]. In biology specific structures of proteins are required for their specific functioning which keeps a cell living. Double barreled chaperonins capture protiens into them to fold them to specific structures. Recently, an array of genetically engineered chaperonin templates have been used by McMillan *et. al.* [135] to produce ordered nano- particle arrays.

   This chapter is organized as follows. In the next section, we shall introduce the model confined solid and discuss the geometry and basic definitions of various structural and thermodynamic parameters. We shall then introduce the various possible structures and phases with their basic characteristics. This will be followed by the results of computer simulations, in the constant NAT (number, area, temperature) ensemble, exploring the deformation and failure properties of this system and the relation of the various structures described in the previous section to one another. In the fifth section we shall try to understand the various transitions seen in the computer simulations within simple mean field free volume and density functional approaches. In section **VI** we shall show the effect of fluctuations and its role in destruction of long range order in this system. We conclude the chapter in section **VII**.

5.1 The Model System

The bulk system of hard disks where particles i and j, in two dimensions, interact with the potential $V_{ij} = 0$ for $|\mathbf{r}_{ij}| > d$ and $V_{ij} = \infty$ for $|\mathbf{r}_{ij}| \leq d$, where d is the hard disk diameter and $\mathbf{r}_{ij} = \mathbf{r}_j - \mathbf{r}_i$ the relative position vector of the particles, has been extensively[71, 99, 105–107] studied. Apart from being easily accessible to theoretical treatment[109], experimental systems with nearly "hard" interactions viz. sterically stabilized colloids[96] are available. The hard disk free energy is entirely entropic in origin and the only thermodynamically relevant variable is the number density $\rho = N/V$ or the packing fraction $\eta = (\pi/4)\rho d^2$. Accurate computer simulations[99] of hard disks show that for $\eta > \eta_f = .719$ the system exists as a triangular
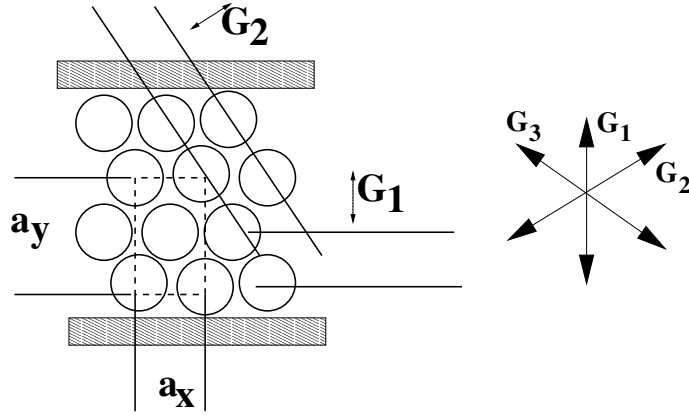
Figure 5.1: The confined solid is shown along with the centered rectangular (CR) unit cell. For an unstrained triangular lattice $a_x = a_0$ and $a_y = \sqrt{3}a_0$. $\mathbf{G_1}$, $\mathbf{G_2}$ and $\mathbf{G_3}$ denote the directions of the three reciprocal lattice vectors (RLV). The third reciprocal lattice direction $\mathbf{G_3}$ is equivalent to the direction $\mathbf{G_2}$, even in presence of the walls.

lattice which melts below $\eta_m = .706$. Elastic constants of bulk hard disks have been calculated in simulations[71, 136]. The surface free energy of the hard disk system in contact with a hard wall has also been obtained[137] taking care that the dimensions of the system are compatible with a strain-free triangular lattice.

Consider a narrow channel in two dimensions of width L_y defined by hard walls at $y = 0$ and L_y ($V_{\text{wall}}(y) = 0$ for $d/2 < y < L_y - d/2$ and $= \infty$ otherwise) and length L_x with $L_x \gg L_y$. Periodic boundary conditions are assumed in the x direction(Fig.5.1). In order that the channel may accommodate n_l layers of a homogeneous, triangular lattice with lattice parameter a_0 of hard disks of diameter d, (Fig.5.7) one needs,

$$L_y = \frac{\sqrt{3}}{2}(n_l - 1)a_0 + d \tag{5.1}$$

For a system of constant number of particles and L_y, a_0 is decided by the packing fraction η alone. Note that $L_x = n_x a_0 = Na_0/n_l$, and a_0 is given by $\rho = N/L_x L_y$. This gives

$$a_0 = \frac{\frac{-d}{n_l} + \sqrt{\frac{d^2}{n_l^2} + 2\sqrt{3}(1 - \frac{1}{n_l})\frac{1}{\rho}}}{\sqrt{3}(1 - \frac{1}{n_l})}. \tag{5.2}$$

Defining $\chi(\eta, L_y) = 1 + 2(L_y - d)/\sqrt{3}a_0$, the above condition reads $\chi = \text{integer} = n_l$ and violation of Eqn.(5.1) implies a rectangular strain away from the reference triangular lattice of n_l layers. The lattice parameters of a centered rectangular (CR) unit cell are a_x and a_y (Fig. 5.1). In general, for a CR lattice with given L_y we have, $a_y = 2(L_y - d)/(n_l - 1)$ and, ignoring vacancies, $a_x = 2/\rho a_y$.
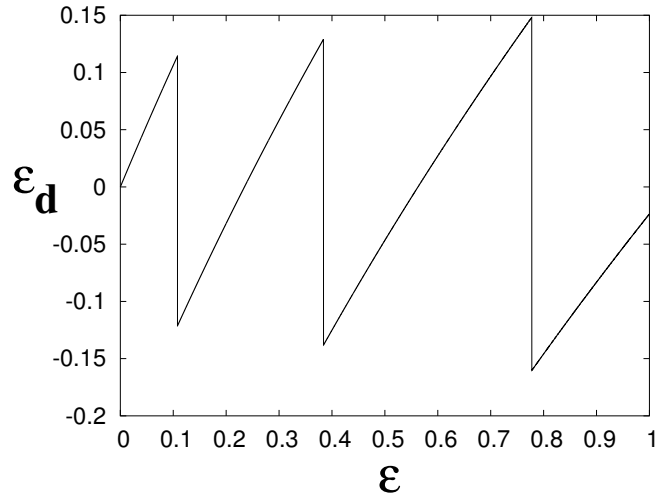
FIGURE 5.2: A plot of internal strain ε_d as a function of external strain ϵ. The jumps in ε_d corresponds to half-integral values of χ.

Calculation of the deformation strain needs some care at this stage. Using the initial triangular solid (packing fraction η_0) as reference, the "external" strain associated with changing L_x, while keeping N and L_y fixed, is $\epsilon = (L_x - L_x^0)/L_x^0 = (\eta_0 - \eta)/\eta$ where η is the packing fraction of the deformed solid and $\eta = N\pi d^2/4L_yL_x$. Internally, the solid is, however, free to adjust n_l to decrease its energy (strain). Therefore, one needs to calculate strains with respect to a reference, distortion-free, triangular lattice at η. Using the definition $\varepsilon_d = \varepsilon_{xx} - \varepsilon_{yy} = (a_x - a_0)/a_0 - (a_y - \sqrt{3}a_0)/\sqrt{3}a_0 = a_x/a_0 - a_y/\sqrt{3}a_0$ and the expressions $a_x = 2/\rho a_y$, $a_y = 2(L_y - d)/(n_l - 1)$, $a_0 = 2(L_y - d)/\sqrt{3}(\chi - 1)$ we obtain,

$$\varepsilon_d = \frac{n_l - 1}{\chi - 1} - \frac{\chi - 1}{n_l - 1}, \tag{5.3}$$

where the number of layers n_l is the nearest integer to χ so that ε_d has a discontinuity at half - integral values of χ. For large L_y this discontinuity and ε_d itself vanishes as $1/L_y$ for all η. This "internal" strain ε_d is related non-linearly to ϵ and may remain small even if ϵ is large (Fig.5.2). Note that any pair of variables η and L_y (or alternately ϵ and χ) uniquely fixes the state of the system.

5.2 Structures and Phases

The different possibilities of structures and phases along with their typical structure factors are presented in this section.
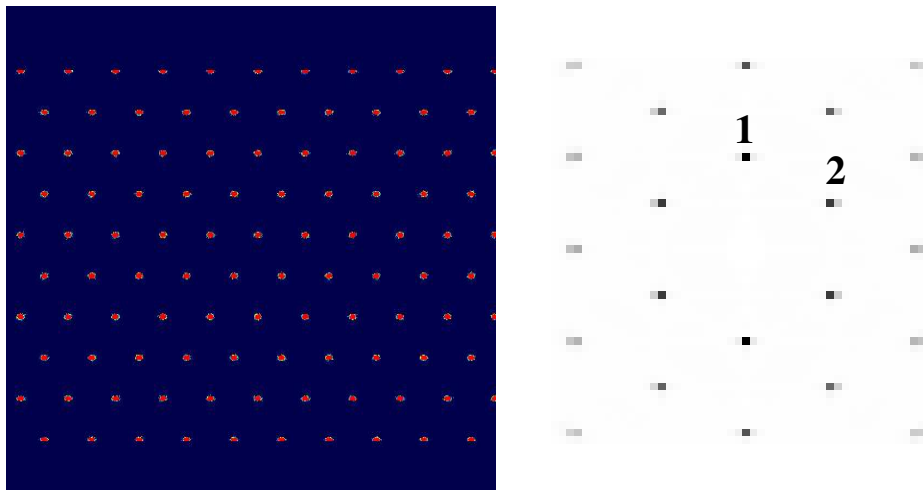
FIGURE 5.3: Solid: Left panel shows an picture of 10^3 overlapped configurations of a high densitiy ($\eta = .85$) solid phase with wall to wall separation commensurate with the density. The color code is such that red means high local density and blue means low density. The right panel shows the corresponding structure factor which shows the typical pattern for a two dimensional hexagonal solid.

If the separation between the hard walls is kept commensurate such that $\chi = n_l$, some integer number of layers then the equilibrium phase is a perfect two dimensional *triangular solid* (Fig.5.3). The solid shows a diffraction pattern which is typical of a two dimensional trangular crystal. We show later that appearances can be deceptive, however. This triangular "solid" is shown to have zero shear modulus which would mean that it can flow without resistance along the length of the channel like a liquid. Stretching the solid strip lengthwise, on the other hand, costs energy and is resisted. The strength of the diffraction peaks decreases rapidly with the order of the diffraction. In strictly two dimensions this is governed by a nonuniversal exponent dependent on the elastic constants [62]. In Q1D this decay should be faster but larger system sizes and averaging over a large number of configurations would be required to observe this decay since contraints placed by the hard walls makes the system slow to equilibriate at high densities. We return to this question in section **VI**.

As discussed in the earlier section, even a small incommensuration due to the confining walls in Q1D immediately introduces elongational asymmetry to local density profiles along the confining directions. As a result of this, a nonzero elongational stress is induced in the system. This causes the two diffraction spots corresponding to planes parallel to the hard walls to strengthen at the cost of the other four spots in the smallest reciprocal lattice set. This increases the one dimensional character of the system even further.

A little extra space introduced between the walls starting from a high density solid phase gives rise to buckling instability in y- direction and the system breaks into triangular solid regions along
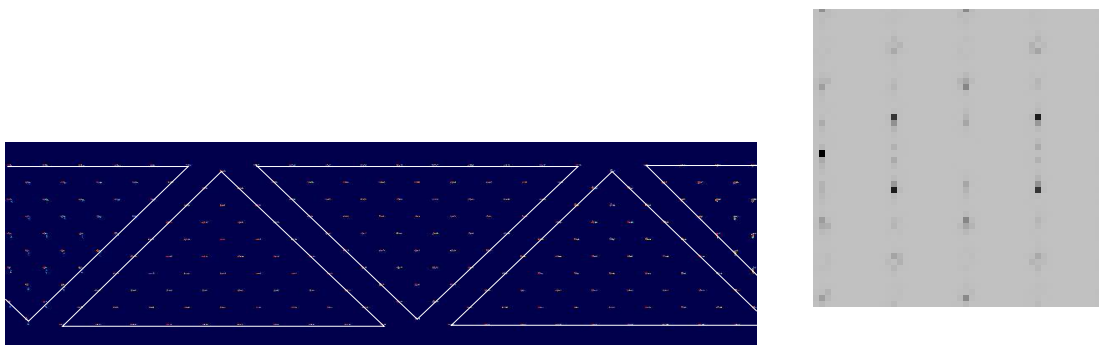
FIGURE 5.4: Buckled phase: A small incommensuration of wall to wall separation introduced via a small increase in it from a separation that is commensurate with a high density triangular solid at $\eta = 0.89$ gives rise to this phase. Increase in channel width reduces the density to $\eta = 0.85$. The left panel shows the picture corresponding to 10^3 overlapped equilibrium configurations. The color code for the local denisties are same as before. Note different portions of triangular solid separated in x- direction are displaced along y- direction to span the extra space introduced between the walls. Lines are drawn to identify this shift in triangular regions. The right panel shows the corresponding structure factor which has the peak in $\mathbf{G}_1$ direction diminished. Some extra weak peaks corresponding to superlattice reflections appear at lower values of the wavenumber.

the x- direction (Fig.5.4). Each of these regions fluctuate with respect to the other in y- direction giving the impression of a buckling wave travelling along the length of the solid. In conformity with the two dimensional analog [118–120] we call this the *buckled solid* and it interpolates continuously from $\chi = n_l$ to $n_l \pm 1$ layers. This phase can also occur due to the introduction of a compressional strain in x-direction keeping L_y fixed. We do not observe the buckled solid at low densities close to the freezing transition. Extreme incommensuration at such densities lead to creation of bands of the smectic phase within a solid eventually causing the solid to melt (see next section). The diffraction pattern shows a considerable weakening of the spots corresponding to planes parallel to the walls, together with an extra spot at smaller wavenumber corresponding to the buckled superlattice. The diffraction pattern is therefore almost complementary to that of the smectic phase to be discussed below.

At low enough densities or high enough incommensuration the elongated density profiles in the lattice planes parallel to the walls can overlap to give rise to a *smectic* phase (Fig.5.5) in which local denity peaks are completely smeared out in x- direction but are clearly seperated in y- direction giving rise to a solid like order in that direction and making the system liquid like in x- direction. The diffraction pattern shows two spots which is typical corresponding to the symmetry of a smectic phase.
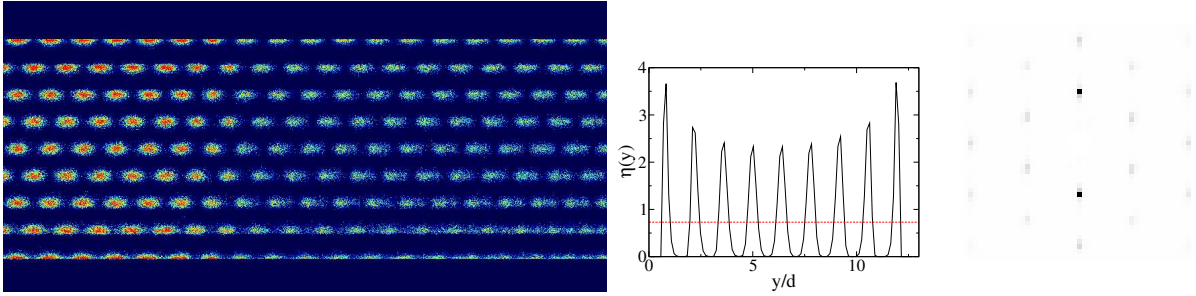
FIGURE 5.5: Smectic: The left panel shows the picture of 10^3 equilibrium configurations. The color code for local density is same as before. The middle panel shows the density modulation in y- direction in a typical smectic phase which is solid like in a direction perpendicular to the walls ($\mathbf{G}_1$ direction) and liquid like in the other direction. A fact corroborated by solid- like peak in $\mathbf{G}_1$ direction in structure factor plotted in right hand panel. This is at a packing fraction $\eta = 0.73$ obtained the straining a triangular lattice at $\eta = 0.85$ in x- direction.

At further lower densities the relative Lindeman parameter, a quantity which measures the relative displacement fluctuations between neighbours (will be defined in following section) diverges and the structure factor shows a ring- like feature typical of a liquid appears together with the smectic like peaks in $\mathbf{G}_1$ direction. This is a *modulated liquid* (Fig.5.6). The density modulation decays away from the walls and in channels with larger widths, the density profile in the middle of the channel becomes uniform.

5.3 Mechanical Properties and Failure

A bulk solid, strained beyond it's critical limit, fails by the nucleation and growth of cracks[138–141]. The interaction of dislocations or zones of plastic deformation[141, 142] with the growing crack tip determines the failure mechanism viz. either ductile or brittle fracture. Studies of the fracture of single-walled carbon nanotubes[143, 144](SWCNT) also show failure driven by bond-breaking which produces nano cracks which run along the tube circumference leading to brittle fracture. Thin nano-wires of Ni are known[145, 146], on the other hand, to show ductile failure with extensive plastic flow and amorphization.

In this section we shall present our results for the mechanical behaviour and failure of the Q1D solid under tension. As mentioned earlier, we show that the Q1D solid behaves anomalously, showing a reversible plastic deformation and failure in the constant extension ensemble. The failure occurs by the nucleation and growth of smectic regions which occur as distinct bands spanning the width of the solid strip.

We study the effects of strain on the hard disk triangular solid at fixed L_y large enough to
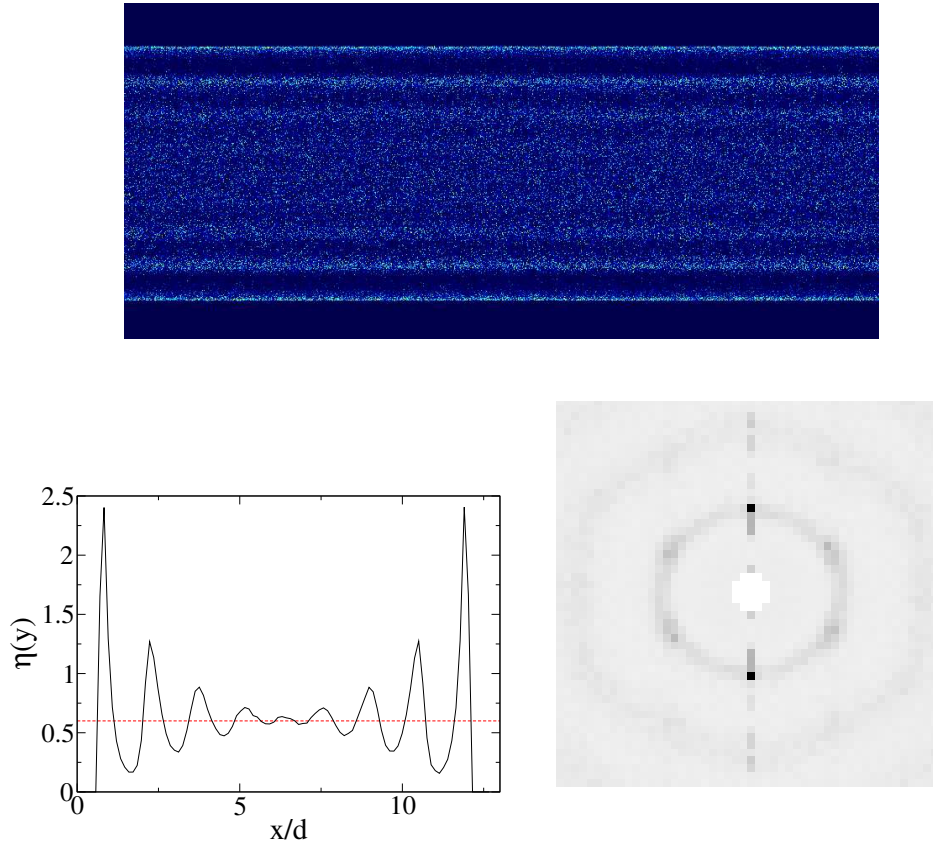
FIGURE 5.6: Modulated liquid: The upper panel shows the picture of 10^3 equilibrium configurations. Local denisties are coded in the same color code as before. The lower left hand panel shows the density modulation in y- direction which is like the smectic phase but the modulation dies out at the centre. The structure factor in right hand panel shows a ring structure which is a typical signature of liquid superimposed on smectic- like strong peaks in $\mathbf{G}_1$ direction. This is the signature of a modulated liquid. This behaviour is found at a packing fraction $\eta = 0.6$ obtained the straining a triangular lattice at $\eta = 0.85$ in x- direction.

accommodate a small number of layers $n_l \sim 9 - 25$. We monitor the Lindemann parameter

$$l = <(u^x{}_i - u^x{}_j)^2> /a_x^2 + <(u^y{}_i - u^y{}_j)^2> /a_y^2$$

where the angular brackets denote averages over configurations, i and j are nearest neighbors and $u^\alpha{}_i$ is the α-th component of the displacement of particle i from it's mean position. The parameter l diverges at the melting transition [147]. We also measure the structure factor

$$\rho_{\mathbf{G}} = \left| \left\langle \frac{1}{N^2} \sum_{j,k=1}^{N} \exp(-i\mathbf{G}.\mathbf{r}_{jk}) \right\rangle \right|,$$

for $\mathbf{G} = \pm\mathbf{G_1}(\eta)$, the reciprocal lattice vector (RLV) corresponding to the set of close-packed lattice planes of the CR lattice perpendicular to the wall, and $\pm\mathbf{G_2}(\eta)$ the four equivalent RLVs
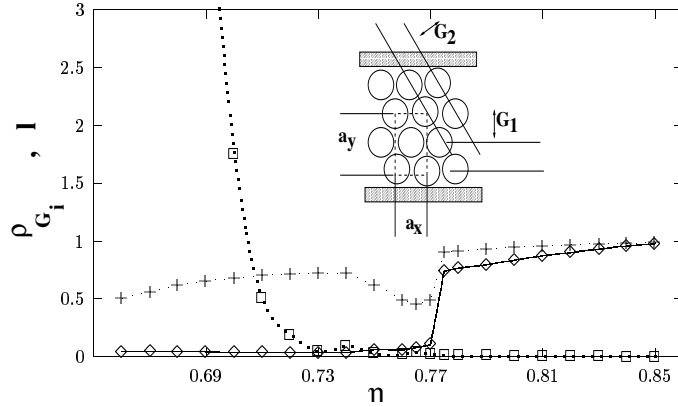
FIGURE 5.7: Results of NVT ensemble Monte Carlo (MC) simulations of $N = n_x \times n_y = 65 \times 10$ hard disks confined between two parallel hard walls separated by a distance $L_y = 9\,d$. For each η, the system was equilibrated over 10^6 MC steps (MCS) and data averaged over a further 10^6 MCS. At $\eta = 0.85$ we have a strain free triangular lattice. Plots show the structure factors $\rho_{\mathbf{G_i}}, i = 1(+), 2(\diamond)$ for RLVs $\mathbf{G_i}(\eta)$, averaged over symmetry related directions, as a function of η. Also plotted in the same graph is the Lindemann parameter $l(\square)$. The lines in the figure are a guide to the eye. Inset shows the geometry used, the reciprocal lattice vectors (RLVs) $\mathbf{G_1}$ and $\mathbf{G_2}$ and the CR unit cell.

for close-packed planes at an angle ($= \pi/3$ and $2\pi/3$ in the triangular lattice) to the wall (see Fig.5.1). Notice that $\pm\mathbf{G_2}(\eta)$ and $\pm\mathbf{G_2}(\eta)$ as shown Fig.5.1 in are equivalent directions.

Throughout, $\rho_{\mathbf{G_2}} < \rho_{\mathbf{G_1}} \neq 0$, a consequence of the hard wall constraint[137] which manifests as an oblate anisotropy of the local density peaks in the solid off from commensuration. As η is decreased both $\rho_{\mathbf{G_1}}$ and $\rho_{\mathbf{G_2}}$ show a jump at $\eta = \eta_{c_1}$ where $\chi = \chi^* \approx n_l - 1/2$ (Fig. 5.8 (inset)). For $\eta < \eta_{c_1}$ we get $\rho_{\mathbf{G_2}} = 0$ with $\rho_{\mathbf{G_1}} \neq 0$ signifying a transition from crystalline to smectic like order. The Lindemann parameter l remains zero and diverges only below $\eta = \eta_{c_3}(\approx \eta_m)$ indicating a finite-size- broadened melting of the smectic to a modulated liquid phase. The stress, $\sigma = \sigma_{xx} - \sigma_{yy}$, versus strain, ϵ, curve is shown in Fig. 5.8. For $\eta = \eta_0$ ($\epsilon = 0$) the stress is purely hydrostatic with $\sigma_{xx} = \sigma_{yy}$ as expected. At this point the system is perfectly commensurate with channel width and the local density profiles are circularly symmetric. Initially, the stress increases linearly, flattening out at the onset of plastic behavior at $\eta \overset{<}{\sim} \eta_{c_1}$. At η_{c_1}, with the nucleation of smectic bands, σ decreases and eventually becomes negative. At η_{c_2} the smectic phase spans the entire system and σ is minimum. On further decrease in η towards η_{c_3}, σ approaches 0 from below (Fig. 5.8) thus forming a Van der Waals loop. If the strain is reversed by increasing η back to η_0 the entire stress-strain curve is traced back with no remnant stress at $\eta = \eta_0$ showing that the plastic region is reversible. For the system shown in Figs.5.7 and 5.8, we obtained $\eta_{c_1} \approx .77$, $\eta_{c_2} \approx .74$ and $\eta_{c_3} \approx .7$. As L_y is increased, η_{c_1} merges with η_{c_3} for $n_l \overset{>}{\sim} 25$. If instead, L_x and L_y are both rescaled to keep $\chi = n_l$ fixed or periodic boundary
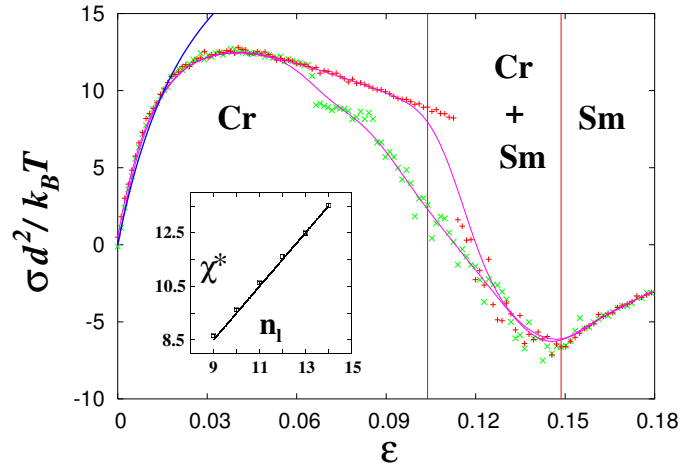
FIGURE 5.8: A plot of the conjugate stress σ versus external strain ϵ obtained from our MC simulations of 65×10 hard disks initially at $\eta = 0.85$. Data is obtained by equilibrating at each strain value for 2×10^4 MCS and averaging over a further 3×10^4 MCS. The stress for the hard disk system has been calculated by the standard method[102]. The entire cycle of increasing $\epsilon(\diamond)$ and decreasing to zero $(+)$ using typical parameters appropriate for an atomic system, corresponds to a real frequency of $\omega \approx 100\mathrm{K\,Hz}$. Results do not essentially change for $\omega = 10\mathrm{K\,Hz} - 1\mathrm{M\,Hz}$. Inset shows the variation of the critical χ^* with n_l, points: simulation data; line: $\chi^* = n_l - 1/2$.

conditions are imposed in both x and y directions, the transitions in the various quantities occur approximately simultaneously as expected in the bulk system. Varying n_x in the range $10 - 1000$ produces no essential change in results.

For $\eta_{c_2} < \eta < \eta_{c_1}$ we observe that the smectic order appears within narrow bands (Fig. 5.9). Inside these bands the number of layers is less by one and the system in this range of η is in a mixed phase. A plot (Fig.5.9 (a) and (b)) of $\chi(x,t)$, where we treat χ as a space and time (MCS) dependent "order parameter" (configuration averaged number of layers over a window in x and t), shows bands in which χ is less by one compared to the crystalline regions. Once nucleated narrow bands coalesce to form wider bands, the dynamics of which is, however, extremely slow. The total size of such bands grow as η is decreased. Calculated diffraction patterns (Fig. 5.9 (c) and (d)) show that, locally, within a smectic band $\rho_{\mathbf{G_1}} \gg \rho_{\mathbf{G_2}}$ in contrast to the solid region where $\rho_{\mathbf{G_1}} \approx \rho_{\mathbf{G_2}} \neq 0$.

The total free energy per unit volume of a *homogeneous* solid, $\mathcal{F}^T$, which is in contact with a hard wall and distorted with a (small) strain ε_d is given by,

$$\begin{aligned} \mathcal{F}^T(\eta, \chi) &= -\rho \ln v_f(\eta, \chi) \\ &\simeq \frac{1}{2} K^\Delta(\eta) \varepsilon_d^2(\chi) + \mathcal{F}^\Delta(\eta) \end{aligned} \tag{5.4}$$
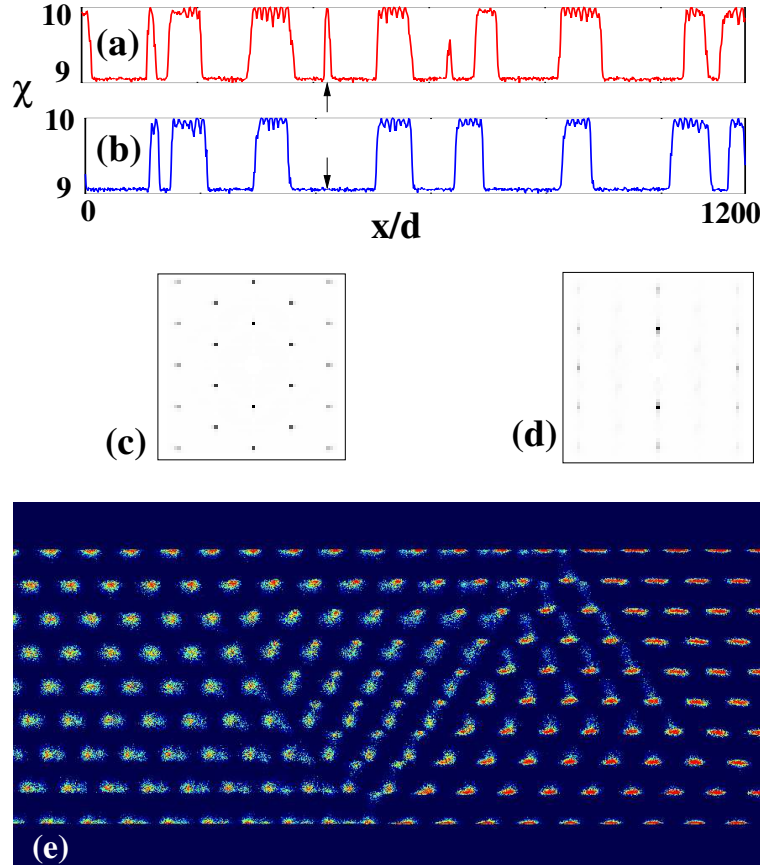
FIGURE 5.9: Plot of $\chi(x,t)$ as a function of the x/d at $\eta = .76$ after time $t = $ (a)5×10^5 and (b)2×10^6 MCS for $N = 10^3 \times 10$. Note that $\chi = 10$ in the solid and $= 9$ in the smectic regions. Arrows show the coalescence of two bands as a function of time. Calculated diffraction patterns for the (c) solid and (d) smectic regions. (e) Close up view of a crystal-smectic interface from superimposed positions of 10^3 configurations at $\eta = .77$. The colors code the local density of points from red/dark (high) to blue/light (low). Note the misfit dislocation in the inter-facial region.

where $K^\Delta(\eta)$ is an elastic constant and $\mathcal{F}^\Delta(\eta)$ the free energy of the (undistorted) triangular lattice in contact with a hard wall[137] at packing fraction η. The "fixed neighbor" free volume $v_f(\eta, \chi)$ may be obtained using straight forward, though rather tedious, geometrical considerations so that $\mathcal{F}^\Delta(\eta) = -k_B T \rho \log v_f(\eta, 0)$ and $K^\Delta(\eta) = \partial^2 \mathcal{F}^\Delta(\eta, \varepsilon_d)/\partial \varepsilon_d^2|_{\varepsilon_d=0}$ (see Fig.5.8). v_f is expressed in units of d^2. In fixed neighbour free volume theory (FNFVT), we think of a single disk moving in a fixed cage formed by taking the average positions of its six nearest neighbor disks [see Fig. (5.10)]. The free volume available to this central particle is given entirely by the lattice separations b $(= AQ)$ and h (See Fig.5.10). Note that, $b = a_0(1 + \epsilon_{xx})$ and $h = \sqrt{3}(1 + \epsilon_{yy})/2$ where a_0 is lattice parameter of a triangular lattice at any given packing fraction η and $\epsilon_{xx} = (n_l - 1)/(\chi - 1)$, $\epsilon_{yy} = (\chi - 1)/(n_l - 1)$. As stated in Sec.5.1, χ is obtained
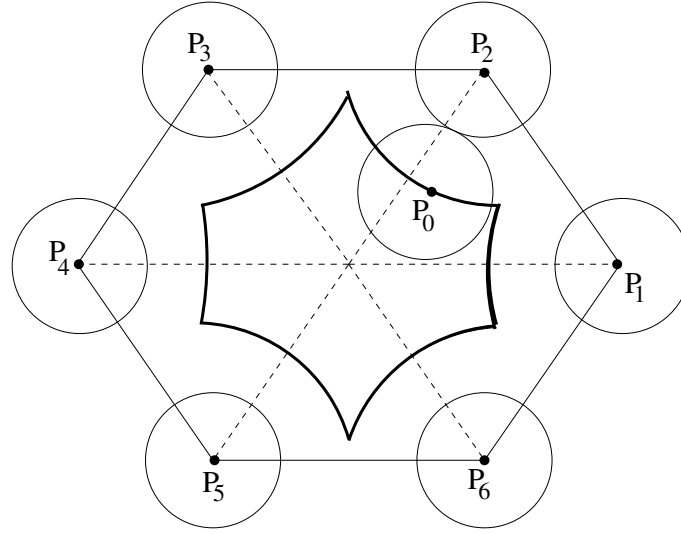
FIGURE 5.10: In our free-volume theory we assume that the outer six disks are fixed and the central disk moves within this cage of fixed particles. The curve in bold line shows the boundary $\mathcal{B}$ of the free volume. A point on this boundary is denoted by $P_0(x, y)$ while the centers of the six fixed disks are denoted by $P_i(x_i, y_i)$ with $i = 1, 2...6$.

from channel width L_y and packing fraction η. v_f is the area enclosed by the boundary $\mathcal{B}$ in Fig.5.10. In calculating the free volume we have assumed the geometry of the free volume to be close to hexagonal (Fig.5.10). For small strains (within 6%) around a triangular lattice this assumption is valid. However, for large strains the free volume area goes over to a rhombic shape. At these points our theory fails. It is clear that $\mathcal{F}^T$ has minima for all $\chi = n_l$. For half integral values of χ the homogeneous crystal is locally unstable. The FNFVT fails also at these points. This same FNFVT free energy for solid is used in Sec.5.5 to calculate the phase diagram of this confined system.

Noting that, $\chi^* = n_l - 1/2$ (Fig. 5.8 inset), it follows from Eqn. 5.3, the critical strain $\varepsilon_d^* = (4n_l - 5)/(2n_l - 3)(2n_l - 2) \sim 1/n_l$ which is supported by our simulation data over the range $9 < n_l < 14$. At these strains the solid generates bands consisting of regions with one less atomic layer. Within these bands adjacent local density peaks of the 'atom's overlap in the x direction producing a smectic. Indeed, the overlap maybe calculated approximately using simple density functional arguments[148] to be $\Delta \equiv \sqrt{< u_x^2 >}/a_x = (\chi - 1)/4\pi \sqrt{C_0 \rho_{\mathbf{G_2}}}(n_l - 1)$ (where C_0, direct correlation function for a hard disk uniform liquid, is a constant of order unity) which, evidently, diverges as $\rho_{\mathbf{G_2}} \to 0$ (see Sec.5.5). Note that at $\chi = \chi^*$ the term $(\chi - 1)/(n_l - 1)$ and hence the overlap shows a jump discontinuity even before $\rho_{\mathbf{G_2}} \to 0$. In Fig.5.11 this overlap term has been plotted as a function of strain ϵ imparted on a ten layered solid. Fig.5.11 shows that the overlap Δ undergoes a jump increase of around 150% at $\epsilon \sim 0.1$ and reaches its highest value
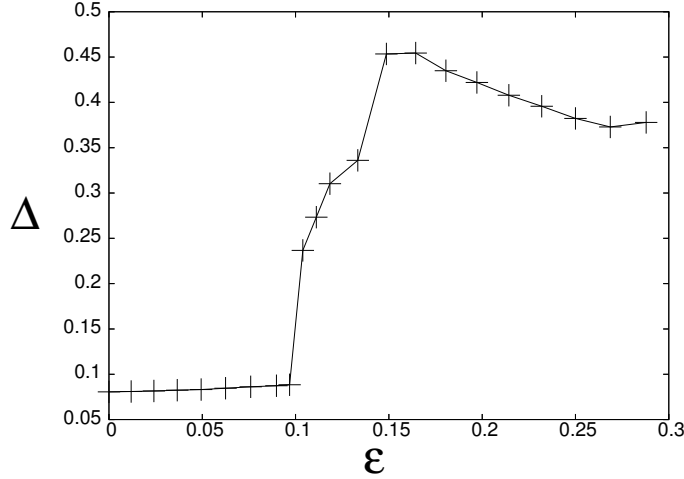
FIGURE 5.11: Values of ρ_{G_2}, χ and n_l have been calculated from the same simulation which is used in plotting Fig.5.7. C_0 has been set to one in calculating density profile overlap Δ at each strain value ϵ.

at $\epsilon \sim 0.15$ as the smectic phase spans the whole system. At further higher strain this overlap decreases with melting of the smectic into fluid phase. This observation further vindicates the phase demarcation in Fig.5.8. For large L_y, the failure strain ε_d^* reduces significantly to wash out the difference in maxima and minima in free energy, therefore, the minima in $\mathcal{F}^T$ merge to produce a smooth free energy surface independent of χ and more conventional modes of failure, viz. cracks, are expected to become operative.

For small L_y all regions of the parameter space corresponding to non-integral χ are also *globally* unstable as belied by the loop in the stress-strain curve (Fig.5.8). The system should therefore break up into regions with n_l and $n_l - 1$ layers for infinitesimal ε_d. Such fluctuations are, however, kinetically suppressed as we argue below. A superposition of many particle positions near such an interface (see Fig. 5.9(e)) shows that: (1) The width of the interface is large, spanning about $10 - 15$ atomic spacings and the interface is wet by a buckling phase made up of triangular groups of nine- layered solid shifted in a direction normal to the walls. (2) The interface between n_l layered crystal and $n_l - 1$ layered smectic contains a *dislocation* [1] with Burger's vector in the y- direction which makes up for the difference in the number of layers. Each band of width s is therefore held in place by a dislocation-anti-dislocation pair (Fig. 5.9). In analogy with classical nucleation theory[148, 149], the free energy F_b of a single band can be written as

$$F_b = -\delta F s + E_c + \frac{1}{8\pi} b^2 K^\Delta \log \frac{s}{a_0} \tag{5.5}$$

---

[1] A comparison of Fig. 5.9 (e) with Fig. 1 of Ref.[117] leads us to speculate whether a two-dimensional version of the "buckled" phase may in-fact wet the solid-smectic interface thereby reducing its energy.
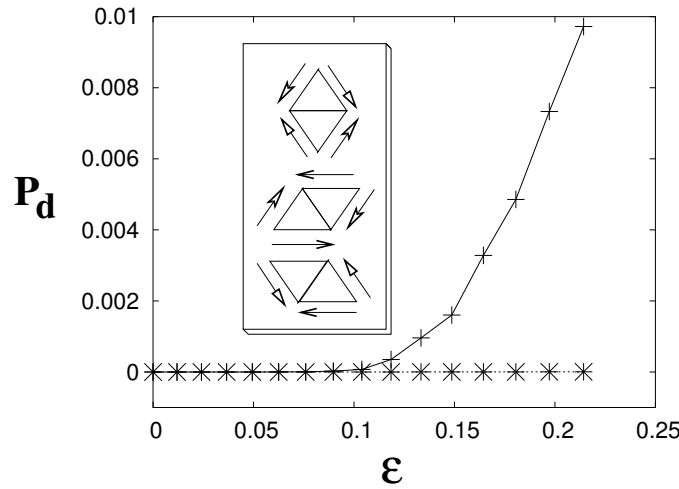
FIGURE 5.12: Dislocation probabilities of a 65×10 system are plotted as a function of strain starting from a solid commensurate with the interwall spacing L_y. The $+$ symbols denote dislocation probabilities for only those Burger's vectors which have components perpendicular to the walls. The corresponding bond-breaking moves are of the type depicted by the uppermost plot in the inset panel. Arrows show the directions of the bond-breaking moves. On the other hand $*$ symbols denote other dislocation probabilities corresponding to the other two types of moves shown in the inset.

where $b = a_y/2$ is the Burger's vector, δF the free energy difference between the crystal and the smectic per unit length and E_c the core energy for a dislocation pair. Bands form when dislocation pairs separated by $s > \frac{1}{8\pi} b^2 K^\Delta / \delta F$ arise due to random fluctuations. To produce a dislocation pair a large energy barrier of core energy E_c has to be overcome. Though even for very small strains ε_d the free energy $\mathcal{F}^T$ becomes unstable the random fluctuations can not overcome this large energy barrier within finite time scales thereby suppressing the production of $n_l - 1$ layered smectic bands up to the point of ε_d^*. In principle, if one could wait for truely infinite times the fluctuations *can* produce such dislocation pairs for any non-zero ε_d though the probability for such productions $\exp(-\beta E_c)$ are indeed very low. Using a procedure similar to that used in Ref.[71], we have monitored the dislocation probability as a function of η (Fig.5.12). Not surprisingly, the probability of obtaining dislocation pairs with the relevant Burger's vector increases dramatically as $\eta \to \eta_{c_1}$ and artificially removing configurations with such dislocations suppresses the transition completely. Band coalescence occurs by diffusion aided dislocation "climb" which at high density implies slow kinetics. Due to this diffusive nature the size of smectic band $L(t)$ scales as $L \sim \sqrt{t}$. Throughout the two-phase region, the crystal is in compression and the smectic in tension along the y direction so that σ is completely determined by the amount of the co-existing phases; orientation relationships between the two phases being preserved throughout. Again the amount of solid or smectic in the system is entirely governed by the strain value ϵ. This means that for

a given strain the amount of solid and smectic and therefore the amount of stress σ is entirely determined by the value of strain. This explains the reversible[150] plastic deformation in Fig. 5.8.

5.4 Mean Field Results: The Reversible Failure Transition

The failure of a commensurate solid under tensile strain imposed in the manner discussed in the previous section, comes about through the nucleation of smectic bands within the solid. Monte-Carlo simulations show, at half-integral χ where the local internal strain ε_d becomes discontinuous, $\rho(\mathbf{r})$ at nearest neighbour sites overlap along the x-direction, parallel to the walls, generating smectic bands. The stress associated with ε_d vanishes at these points and the solid fails under tension. In this section we shall show, using simple density functional[148, 151] arguments, that the phase transition and the consequent tensile failure (a smectic cannot support stress parallel to the smectic layers) is brought about by this overlap in the local density.   Since mechanical failure in our system is a consequence of a phase transition, it is reversible — as the strain is reduced back to zero, the stress also vanishes and the perfect triangular lattice is recovered[152].

Within density functional theory[151], the excess grand potential of a non-uniform liquid containing a density modulation $\rho(\mathbf{r})$ over the uniform liquid of density ρ_l is given by,

$$\frac{\Delta\Omega}{k_B T} = \int d\mathbf{r}[\rho(\mathbf{r})\log(\rho(\mathbf{r})/\rho_l) - \delta\rho(\mathbf{r})]$$
$$-\frac{1}{2}\int d\mathbf{r}' C(|\mathbf{r}-\mathbf{r}'|)\delta\rho(\mathbf{r})\delta\rho(\mathbf{r}'). \tag{5.6}$$

Here $\delta\rho(\mathbf{r}) = \rho(\mathbf{r}) - \rho_l$ and $C(r)$ is the direct correlation function of the uniform liquid[109]. A functional minimization of the free energy yeilds the following self-consistency equation for the density:

$$\frac{\rho(\mathbf{r})}{\rho_l} = \exp[\int d\mathbf{r}' C(|\mathbf{r}-\mathbf{r}'|)\delta\rho(\mathbf{r}')] \tag{5.7}$$

In principle one should solve the above equation within the constraints imposed by the walls and obtain the equilibrium $\rho(\mathbf{r})$. Substitution of this $\rho(\mathbf{r})$ into Eqn.5.6 gives the equilibrium free energy and phase transitions. While we intend to carry out this procedure in the future, we must point out that for the present problem, this is complicated by surface terms and anisotropic, external, fields which are difficult to incorporate. In this chapter we shall take a much simpler route in exploring the various conditions for the solid -smectic transition given the nature of the $\rho_{\mathbf{G_i}}$ (the order parameters) obtained from our simulations.

One may expand, therefore, the logarithm of the local density profile $\log \rho(\mathbf{r})$ in a Fourier series[148] around a lattice point at the origin, to get,

$$\rho(\mathbf{r}) = \mathcal{N} \exp \left(2C_0 \sum_{i=1}^{3} \rho_{\mathbf{G_i}} \cos(\mathbf{G_i}.\mathbf{r}) \right) \tag{5.8}$$

where C_0 is a constant, of order unity, denoting the Fourier transform of the direct correlation function calculated at a q-vector corresponding to the smallest RLV set of the solid. We have kept contributions only from this set.

For a perfect triangular lattice, the RLV's are $\mathbf{G_1} = \hat{y}\frac{2\pi}{d_y}$, $\mathbf{G_2} = \hat{x}\frac{2\pi}{d_y}\cos(\frac{\pi}{6}) + \hat{y}\frac{2\pi}{d_y}\sin(\frac{\pi}{6})$ and $\mathbf{G_3} = \hat{x}\frac{2\pi}{d_y}\cos(\frac{\pi}{6}) - \hat{y}\frac{2\pi}{d_y}\sin(\frac{\pi}{6})$, where $d_y = \frac{\sqrt{3}}{2}a_0$. Using these relations and the fact that in the presence of confining walls the Fourier amplitudes denoting solid order are virtually constant upto the transition and $\rho_{\mathbf{G_2}} = \rho_{\mathbf{G_3}} \neq \rho_{\mathbf{G_1}}$, Eqn.5.8 gives [153],

$$\rho(\mathbf{r}) = \mathcal{N} \exp\{C_0(2\rho_{\mathbf{G_1}} + 4\rho_{\mathbf{G_2}})\} \exp \left(-\frac{1}{2}C_0 \left(\frac{2\pi}{d_y}\right)^2 \{(2\rho_{\mathbf{G_1}} + \rho_{\mathbf{G_2}})y^2 + 3\rho_{\mathbf{G_2}}x^2\} \right) \tag{5.9}$$

Clearly the density profile is Gaussian, of the form, $\rho(\mathbf{r}) \sim exp(-y^2/2\sigma_y^2 - x^2/2\sigma_x^2)$. Therefore, the spreads of density profile in x and y-directions are given by σ_x and σ_y respectively, with

$$\sigma_x^2 = \frac{1}{C_0}\left(\frac{d_y}{2\pi}\right)^2 \frac{1}{3\rho_{\mathbf{G_2}}} \tag{5.10}$$

$$\sigma_y^2 = \frac{1}{C_0}\left(\frac{d_y}{2\pi}\right)^2 \frac{1}{2\rho_{\mathbf{G_1}} + \rho_{\mathbf{G_2}}}. \tag{5.11}$$

In the absence of walls, $\rho_{\mathbf{G_1}} = \rho_{\mathbf{G_2}}$ making $\sigma_x = \sigma_y$, i.e. the density profile comes out to be symmetric in both directions, as expected for the bulk triangular solid. The presence of walls make $\sigma_y < \sigma_x$ making the density profile elliptical with larger spread in x-direction, the direction parallel to the walls. Two neighbouring density profiles will overlap to form a smectic if $\sigma_x > a_x$. This leads us to the definition of a measure of overlap $\mathcal{O}_l = (\sigma_x/a_x)$. The condition $\mathcal{O}_l > 1$ is then the Lindemann criterion for nucleation of the smectic phase. Remembering $a_x = a_0(n_l - 1)/(\chi - 1)$, we get,

$$\mathcal{O}_l = \frac{1}{4\pi}\frac{1}{\sqrt{C_0\rho_{\mathbf{G_2}}}}\frac{\chi - 1}{n_l - 1}. \tag{5.12}$$

Whenever, $\rho_{\mathbf{G_2}} \to 0$ i.e. with the loss of solid order $\mathcal{O}_l$ diverges although σ_y remains finite, since $\rho_{\mathbf{G_1}} \neq 0$ in presence of the walls. This indicates a solid-smectic transition. However, even before $\rho_{\mathbf{G_2}} \to 0$ the quantity $\Delta = \frac{\chi-1}{n_l-1}$ and therefore $\mathcal{O}_l$ shows large jumps at those internal strain (ε_d) values where χ becomes half-integer. It is interesting to note that, at these points ε_d has discontinuities and the system fails[152]. This shows that the mode of failure predicted
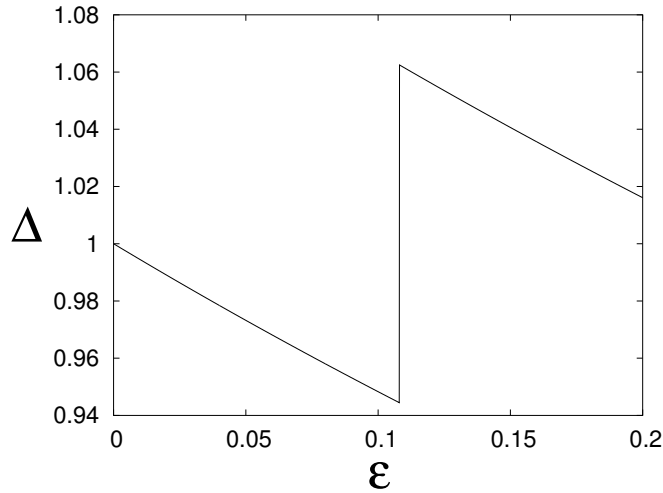
FIGURE 5.13: For a 10-layered solid with L_y commensurate with the initial strainless triangular structure at $\eta = .85$ overlap term Δ is plotted as a function of external strain ϵ. Density profile overlap shows a jump increase at strains $\epsilon > .1$, the failure strain value[152].

by our theory is through a solid-smectic transition. The fact that ρ_{G_1} remains non-zero even at very small densities, due to the confinement from the walls, gives rise to the density modulations in the confined liquid.

We have shown therefore that the overlap in the density profiles may be used as an "order parameter" for the solid to smectic transition. We show below that jumps in this order parameter tantamounts to mechanical failure of the solid.

We begin with studying the overlap Δ as a function of external strain ϵ. For specificity, we start from a triangular solid of packing fraction $\eta = .85$ with L_y commensurate with a $n_l = 10$ layered solid. With increasing strain initially the overlap Δ reduces due to increased separation (a_x) between neighbouring lattice points. But above a strain (ϵ) of about 10%, χ reaches the half-integral mark and Δ shows a discontinuous increase, indicating large overlap between neighbouring density profiles along the wall ; indicating a solid to smectic transition (Fig.5.13) at the failure strain ϵ^*. With further increase in strain the overlap reduces, again due to increased separation between neighbouring lattice points. At higher strains the smectic melts into a modulated liquid due to increased fluctuations connected with the reduced density[152].

We have performed this calculation for various L_y values commensurate with starting triangular solids of $n_l = 2, 3 \ldots 20$ layers at packing fraction $\eta = .85$. We found out the failure strains ϵ^* at each L_y and plotted them in Fig.5.14 as a function of L_y. This clearly shows that the failure strain reduces with increase in L_y. This demonstrates the fact, derived earlier from Monte-Carlo simulations[152], that thinner (smaller L_y) strips are stronger!
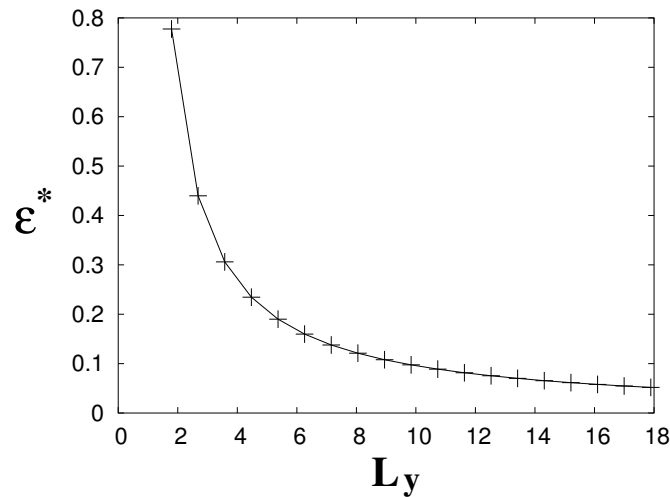
FIGURE 5.14: Failure strains ϵ^* for various interwall separations L_y confining $n_l = 2 \to 20$ layered triangular strips at $\eta = .85$ is plotted. Failure strain decreases with increase in L_y.

In Fig.5.15 we have plotted the overlap term Δ with increasing interwall separation L_y at $\eta = .85$. The jumps, as usual, indicate failure strains corresponding to discontinuities in the internal strain ε_d at half-integral values of χ. The plot shows that the amount of overlap at the failure strains ϵ^* reduces with increasing L_y indicating that at large interwall separations the system starts to behave as a bulk solid and more conventional modes of failure *viz.* through formation and interaction of cracks and twin boundaries starts becoming active.

5.5 Mean Field Results: The Equilibrium Phase Diagram

We now calculate the equilibrium phase diagram of the confined two dimensional system in $\eta - L_y$ plane. For this purpose we utilise the usual common tangent construction method to extract the phase diagram in the canonical ensemble from the free energies of the solid and fluid, the only two unambiguous stable phases of hard disk system in thermodynamic limit. Our computation will, evidently, ignore the other possible phases like smectic and modulating liquid. Physically, confinement always induces density modulations and therefore in phase diagram we understand that the liquid is always a modulated liquid for small channel widths. The phenomenological equation of state due to Santos *et. al.*[154] agrees with bulk fluid simulations of hard disks. The corresponding excess free energy per particle is

$$\mathcal{F}_{San} = \frac{(2\eta_c - 1)\log\left(1 - (2\eta_c - 1)\frac{\eta}{\eta_c}\right) - \log(1 - \frac{\eta}{\eta_c})}{2(1 - \eta_c)}, \tag{5.13}$$
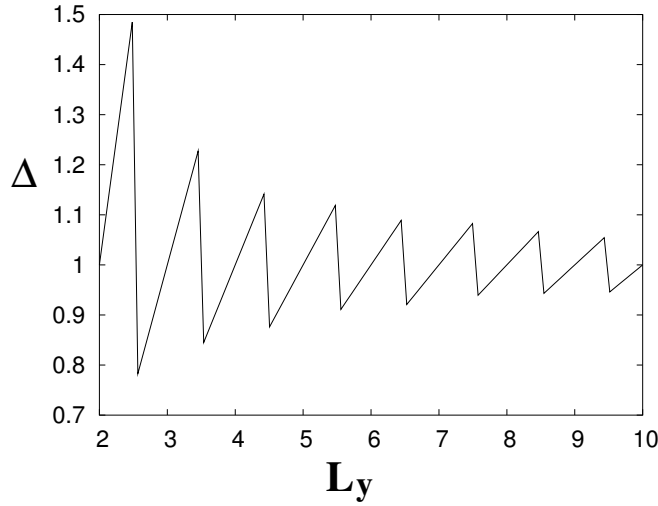
FIGURE 5.15: Overlap Δ is plotted for a system at $\eta = .85$ with changing interwall separation L_y. Amount of smectic overlaps Δ at failures reduces with increasing L_y.

η_c being the packing fraction of hard disk solid at close-packed limit. The total free energy of the fluid will have, moreover, a contribution of free particle free energy per particle $(\log \rho - 1)$. Then the fluid free energy per unit volume becomes $\mathcal{F}_{Fl} = \rho(\mathcal{F}_{San} + \log \rho - 1)$. To incorporate the effect of structureless walls on the fluid we have incorporated the surface tension of a hard disk fluid obtained from scaled particle theory (SPT) [137],

$$\gamma_{Fl} = -\frac{\eta}{2(1-\eta)^2}\rho d + \frac{1}{2}\beta P d \tag{5.14}$$

where the pressure is given by [154]

$$\frac{\beta P}{\rho} = \left(1 - 2\eta + \left(\frac{\eta}{\eta_c}\right)^2 (2\eta_c - 1)\right)^{-1} \tag{5.15}$$

Then the liquid free energy per unit volume becomes $\mathcal{F}_{Fl} = \rho(\mathcal{F}_{San} + \log \rho - 1) + \gamma_{Fl}/L_y$.

We calculate the solid free energy of hard disk system from free volume theory. The surface tension of solid in presence of walls is given by[137]

$$\gamma_{Cr} = \frac{1}{\sqrt{3}}\frac{d}{a(a-d)}\left(1 - \frac{\sqrt{3}}{2}\right). \tag{5.16}$$

Hence the solid free energy per unit volume is $\mathcal{F}_{Cr} = \mathcal{F}_T(\eta, \chi) + \gamma_{Cr}/L_y$. $\mathcal{F}_T(\eta, \chi)$ is the FNFVT free energy as described in Sec.5.3. For every wall to wall separation L_y we vary the packing fraction η and pick up the smaller free energy at each η to obtain $F = \min(\mathcal{F}_{Cr}, \mathcal{F}_{Fl})$ in Fig.5.16.
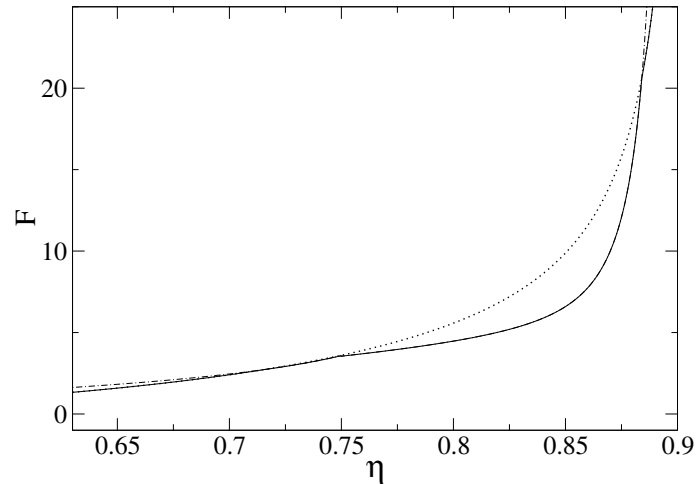
FIGURE 5.16: Plot of free energy used for constructing the phase diagram. The dotted curve, dashed curve and solid curve denote $\mathcal{F}_{Fl}$, $\mathcal{F}_{Cr}$ and F respectively.

Then we use common tangent construction over this free energy F to obtain densities of coexisting phases at equal chemical potential. Within this theory, at densities lower than the coexisting fluid density the thermodynamic phase is stable fluid and at densities higher than the coexisting solid density it is stable solid. At intermediate densities fluid and solid coexist. The corresponding phase diagram is given in Fig.5.17.

From the phase diagram it is evident that solid phase at lower density gets more and more instable as we increase the wall to wall separation. If we start with solids commensurate with L_y, i.e. $\chi = n_l$ at packing fraction $\eta = .85$ and start reducing η keeping L_y fixed, we can find out from the phase diagram the deviatoric strains at which one hits the two-phase boundary as well as the strains where one reaches at half-integral values of χ. These have been plotted in Fig.5.18.

Both the quantities show a decrease in failure strain ε_d^* with increase in width of the strip L_y supporting the simulation result, narrower strips are stronger. Our simple theory therefore predicts a first order solid-fluid transition as a function of ε_d and failure of the solid as the density enters the region of solid-fluid coexistence at larger critical strain ε_d^* for smaller wall to wall separations. However, details like the density modulation, effects of asymmetry in density profile, vanishing displacement modes at the walls and most importantly nucleation and dynamics of misfit dislocations crucial to generate the smectic band mediated failure observed in simulations are beyond the scope of this theory. Also, the effect of kinetic constraints which stabilize the solid phase well inside the equilibrium two phase coexistence region is not captured in this approach. We believe, nevertheless that this equilibrium calculation may be used as a basis for computations of reaction rates for addressing dynamical questions in the future.
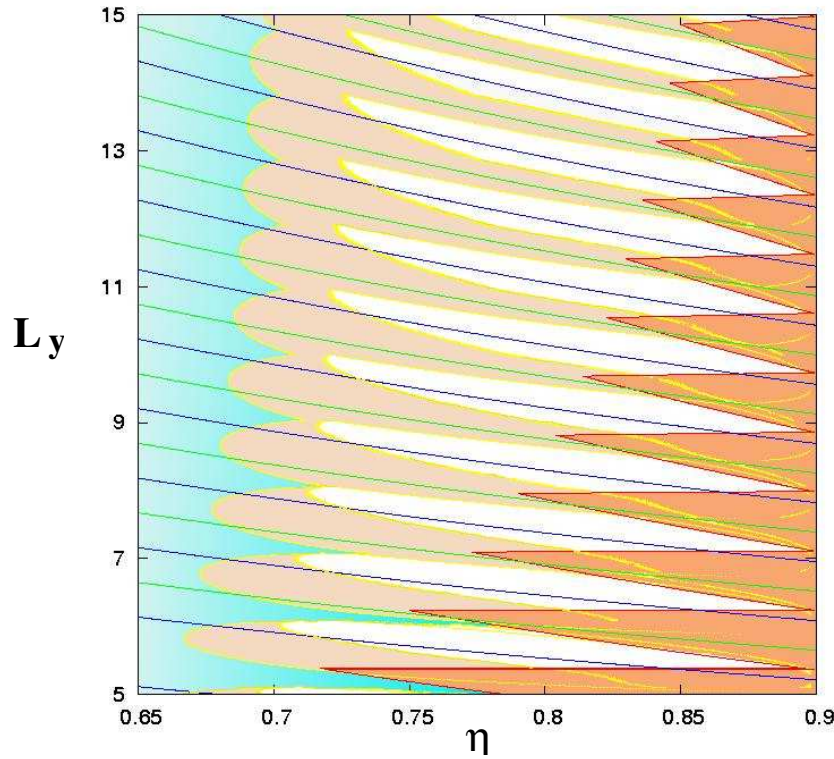
FIGURE 5.17: Phase diagram. White region denotes solid phase. The darkest region at high densities denote regions of phase space inaccessible to the system due to overlapping hard disks. The aqua green region at low densities denote fluid phase. All other regions are two phase coexistence regions. The blue dashed lines denote $\chi = n_l$ and the green dashed lines denote half integral χ.

5.6 Fluctuations and Destruction of Order

One of the key definitions of a solid states that a solid, as opposed to a liquid, is a substance which can retain its shape due to its nonzero shear modulus. Going by this definition, a Q1D solid confined within planar, structureless walls is not a solid despite its rather striking triangular crystalline order as well as an apparently solid- like structure factor. Indeed, the shear modulus of the confined solid at $\eta = 0.85$ is zero, though the corresponding system with periodic boundary condition show large shear modulus (See Fig.5.19). This is a curious result and is generally true for all values of $4 < n_l < 25$ and η investigated by us.

To understand the nature and amount of fluctuations in the confined Q1D system we calculate correlation between displacement fields along the channel, $< (u^x(x) - u^x(0))^2 >$ for a layer of particles near a boundary. The nature of the *equilibrium* displacement correlations ultimately determines the decay of the peak amplitudes of the structure factor and the value of the equilibrium elastic moduli [148]. In one dimension $< (u^x(x) - u^x(0))^2 > \sim x$ and in two dimensions
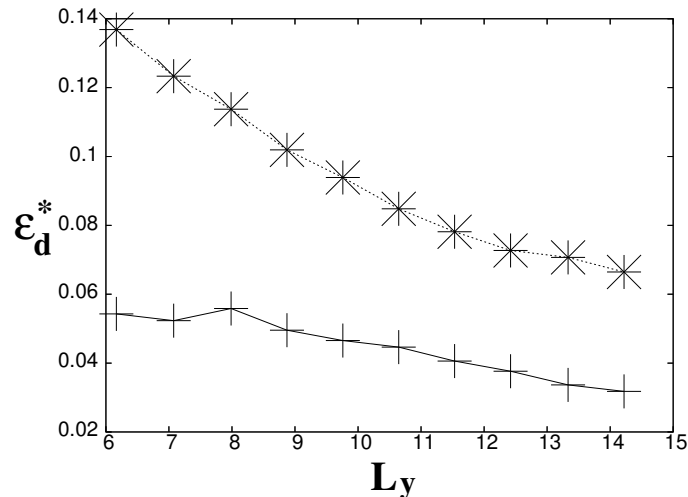
FIGURE 5.18: The data points denoted by ∗ show the deviatoric strain values at which $\chi = n_l - 1/2$ whereas the symbols + denote the arrival of two phase coexistance, *i.e.* failure predicted by this theory. Lines are guide to eye. Data have been extracted from Fig.5.17.

$< (u^x(x) - u^x(0))^2 > \sim \ln(x)$. In the Q1D system it is expected that for small distances, displacement fluctuations will grow logarithmically with distance which will crossover to a linear growth at large distances [155, 156]. We calculate this quantity averaged over 10, 30, 50, 100 configurations equlibrated over 10^5 Monte- Carlo (MC) steps and separated by 10^3 MC steps. We compare the results obtained from a 5000×10 hard diks solid at $\eta = 0.75$ with periodic boundary conditions (PBCs) and with hard channel confinement (Fig.5.20). The structure factor for this system is apparently solid like with prominent triangular order. The shear modulus is vanishingly small for the confined system and non- zero for a system with PBCs. We calculate fluctuations averaged over 10, 30, 50, 100 configurations equlibrated over 10^5 Monte- Carlo (MC) steps and separated by 10^3 MC steps. The fluctuation of displacement field for the system with PBC reduces and converges with the increase in number of configurations over which averagings are done. However, for the confined solid displacement fluctuations continue to increase with number of configurations over which the averaging is done. This clearly shows that as soon as a solid gets confined, even if the confinement length scale is commensurate with that set by the system density, the solid starts to behave like a liquid with zero shear modulus and linearly increasing displacement correlations. Density modulations introduced by the hard walls seems to destabilize long ranged order in the small channel. This is reminiscent of large potential strength limit of laser induced transitions [89, 94, 157] as discussed in the last chapter. However, when we compare the results obtained from a 5000×10 hard disks solid at $\eta = 0.85$ with PBCs and hard channel confinement (Fig.5.21) we obtain a different result. Fig.5.21 clearly shows that with
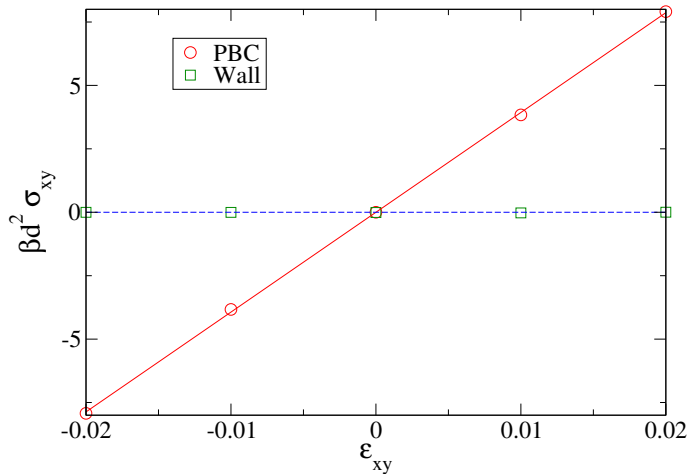
FIGURE 5.19: Shear stress vs. shear strain at $\eta = 0.85$. A system of 43×50 2D hard disks simulated with periodic boundary conditions gives a shear modulus $\mu = 393.42$ with an error within 1%. On the other hand when a 40×10 triangular lattice of hard disks is confined within a commensurate channel, that fits 10-layers of lattice planes, the shear modulus drops drastically to $\mu = 0$!

increase in number of configurations over which the averagings are done, fluctuation reduce and converge to a small number. This is consistent with the solid like structure factor but inconsistent with the vanishing shear modulus of confined system. This result is particularly surprising since it can be shown[155] that *all* Q1D solids whether with PBCs or not and for any density η would have displacement correlations which increase linearly with system length. The exact value of this crossover length has nonuniversal prefactors which depend on boundary conditions, density, nature of interactions etc. If the crossover length turns out to be larger than the system size, then this increase will not be observed and the properties of the system will be anomalous and inconsistent. The fact that displacement fluctuations saturate at high densities as seen in our simulations suggests that this may, in fact, be the reason behind the puzzling behaviour. An accurate calculation of the crossover length is required to settle this question conclusively – a task which is non-trivial due to the nonuniversal nature of this number.

A separate calculation of Young's moduli (response to elongational strain) on a commensurate 40×10 hard disk confined solid at $\eta = 0.85$ shows that $Y_x = 1361$ and $Y_y = 1503$ within 3% error. Young modulus in the longitudinal direction is smaller than that in the direction transverse to the confinement and both these values are larger than the Young modulus of the system under PBC ($Y = 1350$). This implies that the non-hydrodynamic component of the stress $\sigma_{xx} - \sigma_{yy}$ is non-zero for non zero strains as shown in Fig.5.8. Therefore even if we choose to regard this Q1D solid as a liquid, it is quite anomalous since it trivially violates Pascal's law which states that the stress tensor in a liquid is always proportional to the identity! Lastly, commensurability
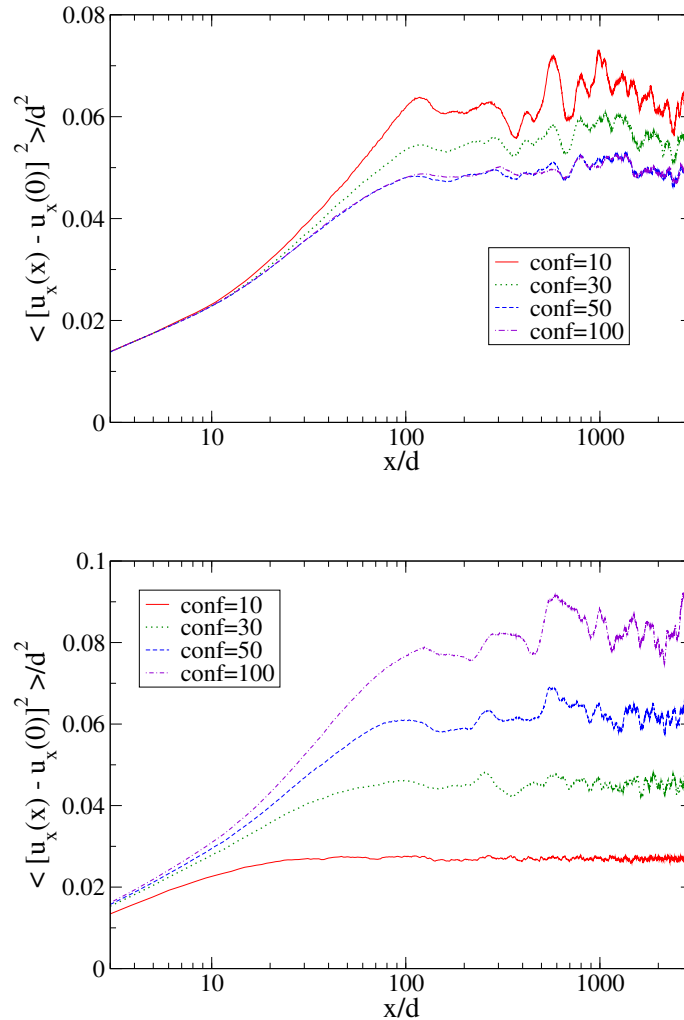
FIGURE 5.20: $< (u^x(x) - u^x(0))^2 > /d^2$ fluctuations within a single lattice plane (line) is averaged over equilibrated configurations of 5000×10 system of hard disks at $\eta = 0.75$ and simulation box dimensions which are commensurate with the lattie parameter of the bulk (unconfined) system. The upper panel shows the case for a system with periodic boundary condition while the lower panel shows the same for Q1D confinement using hard walls. For the confined system, fluctuations increase with increase in the number of configurations over which the displacement correlations are averaged without showing any sign of convergence. Fluctuations in the system with periodic boundary conditions, on the other hand, appear to saturate.

seems to affect strongly the nature and magnitude of the displacement fluctuations which increase dramatically as the system is made incommensurate. Similar behaviour has been recently noticed by A. Ricci *et. al.* [155] for a confined soft disk system. They also noticed that the 1D structure factor of their system showed liquid like behaviour. Here we note that in the work done by A. Ricci *et. al.* [155], they used a soft core interaction potential $(1/r^{12})$ and a soft system- wall
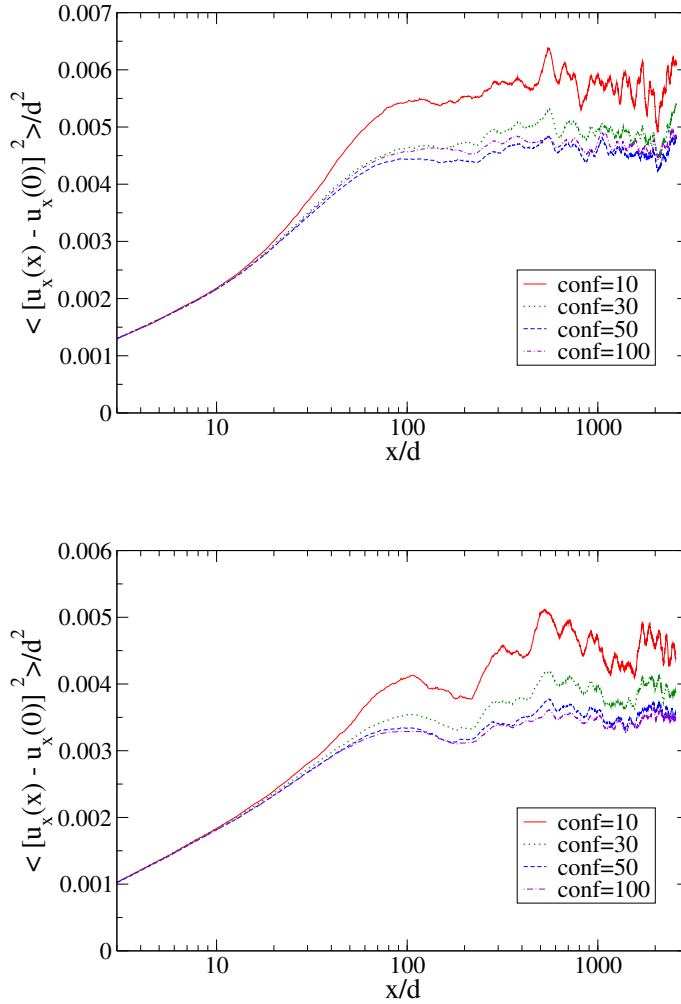
FIGURE 5.21: The same quantities as in Fig.5.20 averaged over equilibrated configurations of 5000×10 system of hard disks at $\eta = 0.85$ and a simulation box size that is commensurate with the lattie parameter of the bulk (unconfined) system. With increase in the number of configurations over which averaging is done, fluctuations reduce and converge, both for a system with periodic boundary condition and for the confined system in channel.

potential $(1/r^{10})$ and studied the shear modulus and structure factor at density $\rho = 1.05$, very close to bulk phase transition at $k_B T = 1$. In that system it is difficult to determine whether the system is commensurate or not, since the long ranged soft wall potential would tend to distort the triangular lattice so that the equilibrium state would not be a perfect triangular solid. Our system has the advantage of having much simpler ground states which makes these distinctions unambiguous.

5.7 Conclusion

In this chapter we explored some of the strange and anomalous properties of Q1D solids which are only a few atomic dimensions wide in one direction. We have found that these properties persist even if the width is increased by a large amount and the approach to bulk behaviour is slow. The bulk limit is also approached in an oscillating manner with commensurability playing a very important role.

What impact, if any, do our results have for realistic systems? Apart from constrained hard sphere colloids[96] where our results are directly testable, a similar fracture mechanism may be observable in experiments on the deformation of mono-layer nano beams or strips of real materials provided the confining channel is made of a material which is harder and has a much smaller atomic size than that of the strip[113, 114]. The effect of elasticity and corrugations of the walls on the fracture process, as well as it's dynamics, are interesting directions of future study. The destruction of long ranged solid like order should be observable in nano wires and tubes and may lead to fluctuations in transport quantities [158].

In the next chapter we shall study the transport of heat accross a Q1D solid and try to find out the effect of the reversible failure transition in the heat transport coefficient.

6 Heat Conduction in Confined Solid

Jose Arcadio Buendia ventured a murmur: "It's the largest diamond in the world". "No", the gypsy countered, "It's ice". — *G. G. Márquez*

In the previous chapter [152] we have observed that the properties of a solid that is confined in a narrow channel can change drastically for small changes in applied external strain. This was related to structural changes at the microscopic level such as a change in the number of layers of atoms in the confining direction. These effects occur basically as a result of the small (few atomic layers in one direction) dimensions of the system considered and confinement along some direction. A similar layering transition, in which the number of smectic layers in a confined liquid changes discretely as the wall-to-wall separation is increased, was noted in [132, 133]. Both [132, 152] look at equilibrium properties while [133] looks at changes in the dynamical properties. An interesting question is as to how transport properties, such as electrical and thermal conductivity, get affected for these nanoscale systems under strain. These questions are also important to address in view of the current interest in the properties of nanosystems both from the point of view of fundamentals and applications [20, 159, 160].

In this chapter we consider the effect of strain on the heat current across a two-dimensional "solid" formed by a few layers of interacting atoms which are confined in a long narrow channel. We note here that, in the thermodynamic limit it is expected that there can be no true solid phase in this quasi-one-dimensional system. However for a long but finite channel, which is our interest here, and at high packing fraction the fluctuations are small and the system behaves like a solid. We will thus use the word "solid" in this sense.

In previous chapter [152] the anomalous failure, under strain, of a narrow strip of a two dimensional solid formed by hard disks confined within hard walls [see Fig. 6.1] was studied. Sharp jumps in the stress-strain were observed. These were related to structural changes in the system which underwent transitions from solid-to-smectic-to-modulated liquid phases [152, 153]. In the present chapter we study changes in the thermal conductance of this system as it undergoes elastic deformation and failure through a layering transition caused by external elongational strains applied in different directions.

The calculation of heat conductivity in a many body system is a difficult problem. The Kubo formula and Boltzmann kinetic theory provide formal expressions for the thermal conductivity.
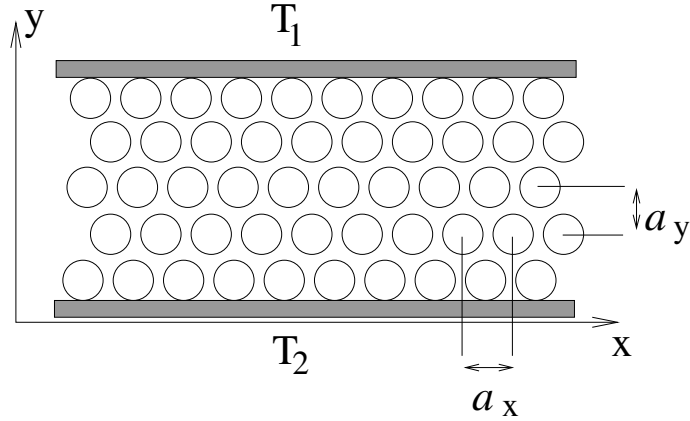
FIGURE 6.1: A solid with a triangular lattice structure formed by hard disks confined between two structureless walls at $y = 0$ and $y = L_y$. The walls are maintained at two different temperatures. The lattice parameters of the unstrained solid are denoted by a_x^0 and a_y^0. Elongational strains can be imposed by rescaling distances either in the x or y directions and the lattice parameters change to a_x and a_y.

In practice these are usually difficult to evaluate without making drastic approximations. More importantly a large number of recent studies [161–164] indicate that the heat conductivity of low-dimensional systems infact diverge. It is then more sensible to calculate directly the heat current or the conductance of the system rather than the heat conductivity. In this chapter we propose a simple-minded calculation of the heat current which can be expected to be good for a hard disk (or hard spheres in the three dimensional case) system in the solid phase. This reproduces some qualitative features of the simulations and gives values for the current which are of the correct order of magnitude.

The organization of this chapter is as follows. In Sec. (6.1) we explain the model and present the results from simulations. In Sec. (6.2) we derive a simple formula for heat current in a hard-sphere system and evaluate it approximately. We conclude with some discussions in Sec. (6.3).

6.1 Results from Simulations

We consider a two dimensional system of hard disks of diameter d and mass m which interact with each other through elastic collisions. The particles are confined within a narrow hard structureless channel [see Fig. 6.1]. The hard walls of the channel are located at $y = 0$ and $y = L_y$ and we take periodic boundary conditions in the $x-$direction. The length of the channel along the $x-$direction is L_x and the area is $\mathcal{A} = L_x \times L_y$. The confining walls are maintained at two different temperatures (T_2 at $y = 0$ and T_1 at $y = L_y$) so that the temperature difference

$\Delta T = T_2 - T_1$ gives rise to a heat current in the y-direction. Initially we start with channel dimensions L_x^0 and L_y^0 such that the system is in a phase corresponding to a unstrained solid with a triangular lattice structure. We then study the heat current in this system when it is strained (a) along the $x-$direction and (b) along the $y-$direction.

We perform an event-driven collision time dynamics [165] simulation of the hard disk system. The upper and lower walls are maintained at temperatures $T_1 = 1$ and $T_2 = 2$ (in arbitrary units) respectively by imposing Maxwell boundary condition [161] at the two confining walls. This means that whenever a hard disk collides with either the lower or the upper wall it gets reflected back into the system with a velocity chosen from the distribution

$$f(\vec{u}) = \frac{1}{\sqrt{2\pi}} \left(\frac{m}{k_B T_W} \right)^{3/2} |u_y| \exp \left(-\frac{m\vec{u}^2}{2k_B T_W} \right) \tag{6.1}$$

where T_W is the temperature (T_1 or T_2) of the wall on which the collision occurs. During each collision energy is exchanged between the system and the bath. Thus in our molecular dynamics simulation, the average heat current flowing through the system can be found easily by computing the net heat loss from the system to the two baths (say Q_1 and Q_2 respectively) during a large time interval τ. The steady state heat current from lower to upper bath is given by $\langle I \rangle = \lim_{t \to \infty} Q_1/\tau = -\lim_{t \to \infty} Q_2/\tau$. In the steady state the heat current (the heat flux density integrated over x) is independent of y. This is a requirement coming from current conservation. However if the system has inhomogeneities then the flux density itself can have a spatial dependence and in general we can have $j = j(x, y)$. In our simulations we have also looked at $j(x, 0)$ and $j(x, L_y)$.

Note that the relevant scales in the problem are: $k_B T$ for energy, d for length and $\tau_s = \sqrt{md^2/k_B T}$ for time. We start from a solid commensurate with its wall to wall separation and follow two different straining protocols. In case (a) we strain the solid by rescaling the length in the $x-$direction and the imposed external strain is $\epsilon_{xx} = (L_x - L_x^0)/L_x^0$. In case (b) we rescale the length along the $y-$direction and the imposed strain is $\epsilon_{yy} = (L_y - L_y^0)/L_y^0$.

The only thermodynamically relevant variable for a hard disk system is the packing fraction $\eta = \pi N d^2 / 4\mathcal{A}$. For a close packed solid with periodic boundary condition this value is about $\eta_c = 0.9069$. On the other hand for a confined solid having N_y number of layers $\eta_c = \pi N_y/(2\sqrt{3}(N_y - 1) + 4)$ and for a 10- layered solid $\eta_c = 0.893$. In our simulations we consider initial values of η for the solid to be close to η_c. The channel is "mesoscopic" in the sense that it has a small width with $N_y = 10$ layers of disks in the $y-$direction (in the initially unstrained solid). In the $x-$direction the system can be big and we consider $N_x = 20, 40, 80, 160$ number of disks in the $x-$direction. In collision time dynamics we perform 10^5 collisions per particle to reach steady state and collect data over another 10^5 collisions per particle. All the currents calculated in this study are accurate within error bars which are less than 3% of averaged current.
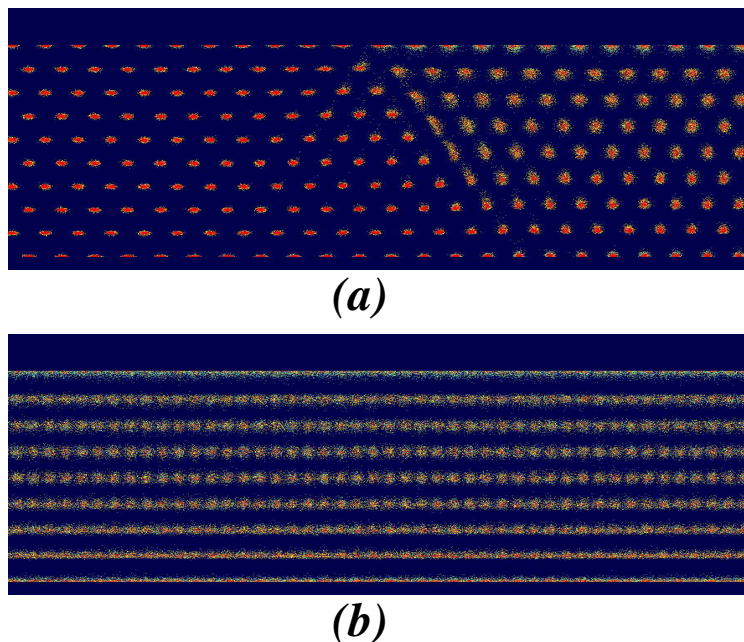
FIGURE 6.2: Plots obtained by superposition of 500 steady state configurations of a portion of 40×10 system taken at equal time intervals. Starting from $\eta = 0.85$ imposition of strains (a) $\epsilon_{xx} = 0.1$, (b) $\epsilon_{xx} = 0.15$ gives rise to these structures. The colors code local density of points from red/dark (high) to blue/light (low). In (a) one can see a 9-layered structure nucleated within a 10-layered solid. The corresponding structure factor identifies this to be a smectic [152]. In (b) the whole system has transformed into a 9-layered smectic.

Let us briefly recapitulate some of the equilibrium results for stress-strain behavior obtained in the last chapter. As the strain ϵ_{xx} is imposed, the perfectly triangular solid shows rectangular distortion along with a linear response in strain versus stress behavior. Above a critical strain $(\epsilon_{xx} \approx 0.1)$ one finds that smectic bands having a lesser number of layer nucleate within the solid [this can also be seen in Fig. (2a), which is for a nonequilibrium simulation]. This smectic is liquid-like in $x-$direction (parallel to the walls) and has solid-like density modulation order in $y-$direction (perpendicular to the walls). With further increase in strain the size of the smectic region increases and ultimately the whole system goes over to the smectic phase at $\epsilon_{xx} \approx 0.15$ [Fig. (2b)]. At even higher strains the smectic melts to a modulated liquid [152, 153]. The modulated liquid shows typical liquid like ring pattern corresponding to average inter- particle separation above the smectic like 1D density modulation peaks in the structure factor [152, 166]. This layering transition is an effect of finite size in the confining direction. Similar phase behaviors have been observed in experiments on steel balls confined in quasi 1D [134]. We note that to fit
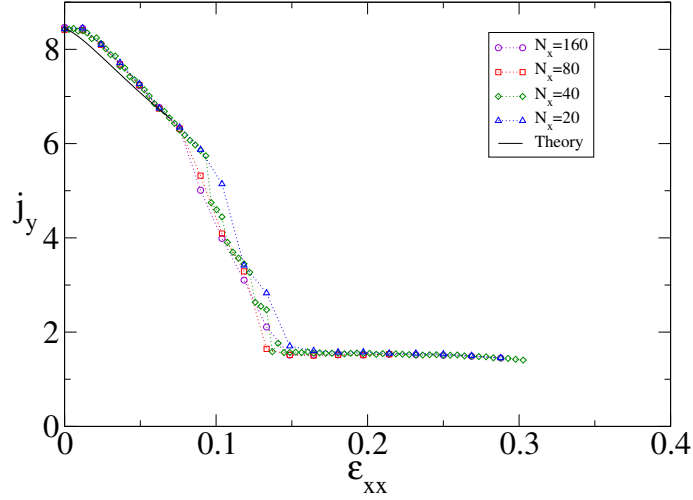
FIGURE 6.3: Plot of j_y (in units of $k_B T/\tau_s d$) versus ϵ_{xx} for different lengths of the channel. The width of the channel is $N_y = 10$ layers. Starting packing fraction is $\eta = 0.85$. The solid line shows the theoretical prediction of dependence of the heat current on strain [see Sec. (6.2)].

a N_y layered triangular solid within a channel of width L_y we require

$$L_y = \frac{\sqrt{3}}{2} a_x^0 (N_y - 1) + d . \qquad (6.2)$$

This enables us to define a fictitious number of layers

$$\chi = 2\frac{L_y - d}{\sqrt{3}a} + 1$$

of triangular solid that can span the channel where a is the lattice parameter at any given density. The actual number of layers that are present in the strained solid is $N_y = I(\chi)$ where the function $I(\chi)$ gives the integer part of χ. For confined solids the free energy has minima at integer values of χ and maxima at half-integral values [152, 153]. The difference in free-energy between succesive maxima and minima gradually decreases with increasing L_y. Thereby the layering transition washes out for $n_l \gtrsim 25$ layered unstrained solid[152]. Up to this number of layers, a triangular solid strip confined between two planar walls fails at a critical deviatoric strain $\epsilon_d^* \sim 1/N_y$, i.e. smaller strips fail at a larger deviatoric strain $(\epsilon_d = \epsilon_{xx} - \epsilon_{yy})$.

We now present the heat conduction simulation results for the two cases of straining in x and y directions.

(a) Strain in x direction - In Fig. 6.3 we plot the heat current density j_y calculated at different values of the strain ϵ_{xx}. Starting from the triangular lattice configuration, we find that the heat current decreases linearly with increase in strain. At about the critical strain $\epsilon_{xx} \approx 0.1$ we find that the heat current begins to fall at a faster rate. This is easy to understand physically.
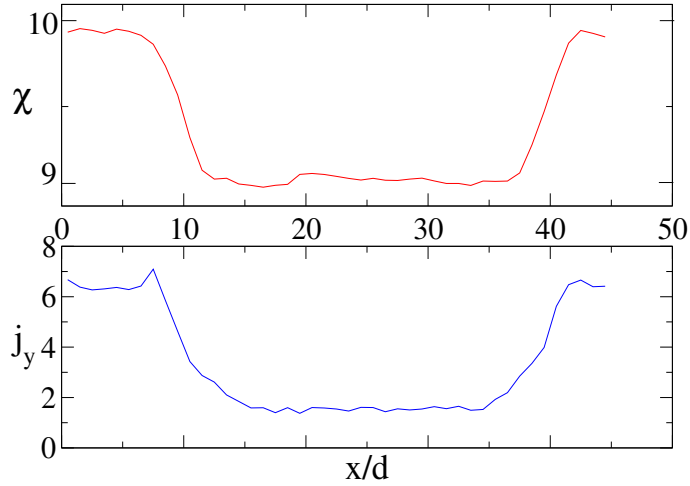
FIGURE 6.4: $\chi(x)$ is the local number of layers averaged over 10^3 steady state configurations for a system of 40×10 hard disks. A starting triangular lattice of $\eta = 0.85$ is strained to $\epsilon_{xx} = 0.118$ and the data collected after steady state set in. Also shown is the local heat current $j_y(x)$. The regions having lower number of layers conduct less effectively.

At the onset of critical strain smectic bands, which have lesser number of particle layers, start nucleating (Fig. 6.2). These regions are much less effective in transmitting heat than the solid phase and the heat current falls rapidly as the size of the smectic bands grow. At about the strain value $\epsilon_{xx} \approx 0.15$ the whole system is spanned by the smectic. Beyond this strain there is no appreciable change in the heat current. The solid line in Fig. 6.3 is an estimate from a simple analysis explained in Sec. (6.2).

In Fig. 6.4 we plot the local steady state heat current $j_y(x)$ for a system of 40×10 particles at a strain $\epsilon_{xx} = 0.118$ $i.e.$ at a strain corresponding to the solid-smectic phase coexistence. At this same strain the number of layers averaged over 10^3 configurations have been plotted. It clearly shows that the local heat current is smaller in regions with smaller number of layers. This is the reason behind getting a sharp drop in average heat current after the onset of phase coexistence.

(b)Strain in y direction - Next we consider the case where, again starting from the density $\eta = 0.85$, we impose a strain along the $y-$direction. As shown in Fig. 6.5, the heat current j_y now has a completely different nature. The initial fall is much steeper and has a form different from the linear drop in Fig. 6.3. The approximate analytic curve is explained in Sec. (6.2). At about $\epsilon_{yy} \approx 0.1$ we see a sharp and presumably discontinuous jump in the current. At this point the system goes over to a buckled phase (Fig. 6.6b) in which different parts of solid (along x- direction) are shifted in y-direction by small displacement to cover extra space between the walls[118–120]. A further small strain induces a layering transition and the system breaks into
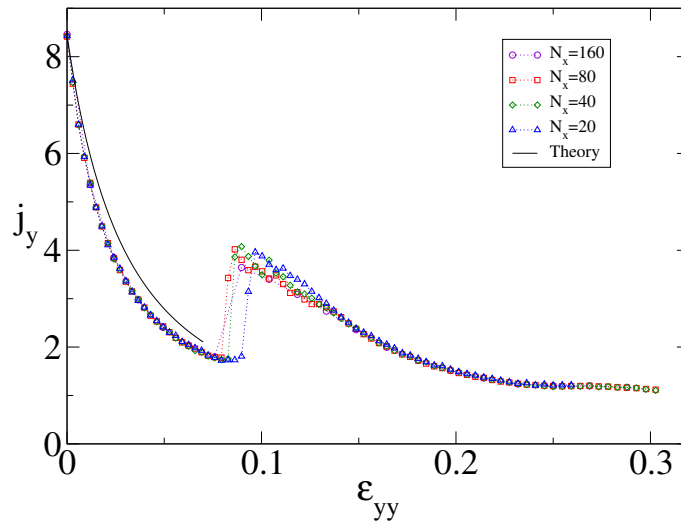
FIGURE 6.5: Plot of j_y (in units of $k_B T/\tau_s d$) versus ϵ_{yy} for different channel lengths. The channel width is $N_y = 10$ layers. The starting packing fraction is $\eta = 0.85$. The jump in current occurs at the strain value where the number of layers in the $y-$direction increases by one and the system goes to a smectic phase. The solid line shows the theoretical prediction of dependence of the heat current on strain [see Sec. (6.2)].

$N_y = 11$ layered solid and $N_y = 10$ layered highly fluctuating smectic like regions. At even higher strains ($\epsilon_{yy} \sim 0.2$) the whole system eventually melts to a $N_y = 11$ layered smectic phase. The phase behavior of this system is interesting and will be discussed in detail elsewhere[166]. Unlike in the case with applied strain in the $x-$direction, in the present case the buckling-layering transition is very sharp. Even though the overall density has *decreased*, due to buckling and increase in number of layers in the conducting direction, there is an increase in the energy transferring collisions and hence the heat current. The plots in Fig. 6.6 show the structural changes that occur in the system as one goes through the transition.

We find in general that the heat current along any direction within the solid follows the same qualitative features as the stress component along the same direction. This can be seen in Fig.6.7 where we have plotted j_y versus ϵ_{xx} for two starting densities of solids $\eta = 0.85, \ 0.89$. In the inset we show the corresponding $-\sigma_{yy}$ versus ϵ_{xx} curves and see that they follow the same qualitative behavior as the heat current curves. The reason for this is that microscopically they both originate from interparticle collisions. Infact the microscopic expressions for the total heat current [see Eq. (6.11) in Sec. (6.2)] is very similar to that for the stress tensor component,

(a)

(b)

(c)
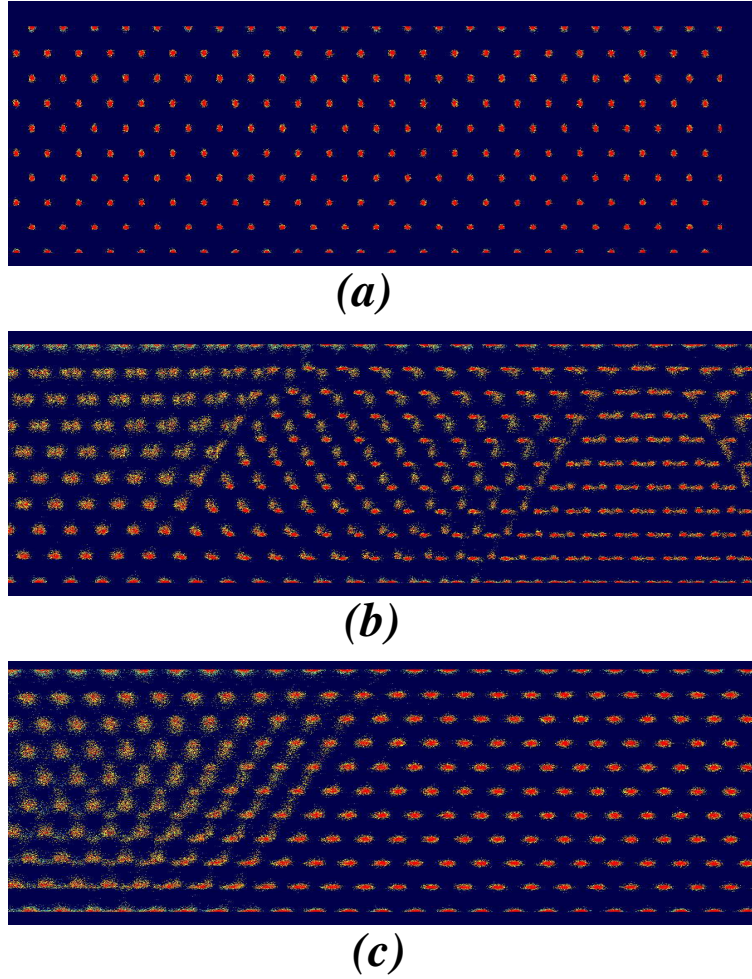
FIGURE 6.6: Plots obtained by superposition of 500 steady state configurations of a portion of 40×10 system taken at equal time intervals. Starting from $\eta = 0.85$ imposition of strains (a) $\epsilon_{yy} = 0.05$, (b) $\epsilon_{yy} = 0.1$, (c) $\epsilon_{yy} = 0.12$ gives rise to these structures. The colors code local density of points from red/dark (high) to blue/light (low). (a) Solid phase. (b) A mixture of 10-layered solid and a buckling phase. (c) An 11-layered solid in contact with 10-layered smectic like region.

with an extra velocity factor. The stress tensor is given by:

$$\mathcal{A}\sigma_{\alpha\beta} \quad = \quad -\sum_i \langle m u_i^\alpha u_i^\beta \rangle + \sum_{i<j} \left\langle \frac{\partial \phi(r_{ij})}{\partial r_{ij}} \frac{x_{ij}^\alpha x_{ij}^\beta}{r_{ij}} \right\rangle , \tag{6.3}$$

where $\{x_i^\alpha, u_i^\alpha\}$ refer to the α-th component of position and velocity of the ith particle, $r_{ij}^2 = \sum_\alpha (x_{ij}^\alpha)^2$ and $\phi(r_{ij})$ is the interparticle potential. For a hard disk system, $\frac{\partial \phi(r_{ij})}{\partial r_{ij}}$ can be replaced by $-k_B T \delta(r_{ij} - \text{d})$. Also in equilibrium we have $\langle m u_i^\alpha u_i^\beta \rangle = k_B T \delta_{\alpha\beta}$ and hence the stress tensor
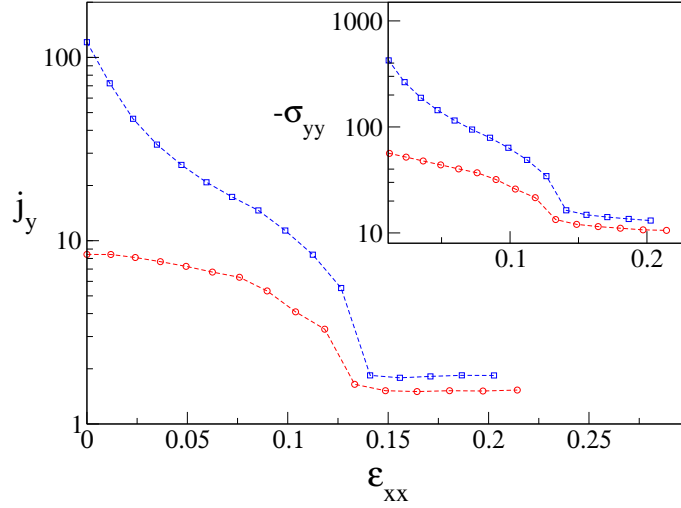
FIGURE 6.7: Plot of j_y (in units of $k_B T/\tau_s d$) versus ϵ_{xx} for two different starting values of the packing fraction. $\Diamond$ corresponds to a starting value of $\eta = 0.89$ while $+$ is for $\eta = 0.85$. In both the cases the initial solid size was 80×10. The inset shows corresponding plots of $-\sigma_{yy}$ (in units of $k_B T/d^2$) versus ϵ_{xx}. Notice that stress-strain curve has the same qualitative profile as the j_y versus ϵ_{xx} curve.

becomes:

$$\mathcal{A}\sigma_{\alpha\beta} = -k_B T \left[N\delta_{\alpha\beta} + \left\langle \sum_{i<j} \frac{x_{ij}^\alpha x_{ij}^\beta}{r_{ij}} \delta(r_{ij}(t) - d) \right\rangle \right] .$$

Using collision time simulation it is easier to evaluate the stress tensor in the following way. We can rewrite Eq. (6.3) as

$$\mathcal{A}\sigma_{\alpha\beta} = -N k_B T \delta_{\alpha\beta} - \sum_{i<j} \left\langle x_{ij}^\alpha f_{ij}^\beta \right\rangle .$$

We use the idea that $\langle \ldots \rangle$ can be replaced by a time average so that from Eq. (6.3) we have

$$\left\langle x_{ij}^\alpha f_{ij}^\beta \right\rangle = - \lim_{\tau \to \infty} \frac{1}{\tau} \int_0^\tau dt x_{ij}^\alpha f_{ij}^\beta .$$

Now note that during a collision we have $\int dt f_{ij}^\beta = \Delta p_{ij}^\beta$ where $\Delta \vec{p}_{ij}$ is the change in momentum of ith particle due to collision with j^{th} particle. It can be shown that $\Delta \vec{p}_{ij} = -(\vec{u}_{ij}.\hat{r}_{ij})\hat{r}_{ij}$ where $\hat{r}_{ij} = \vec{r}_{ij}/r_{ij}$ and $\vec{u}_{ij} = \vec{u}_i - \vec{u}_j$ and $\vec{r}_i,\ \vec{u}_i$ are evaluated just before a collision. This change in momentum occurs for a single pair of particle during one collision event. To get the stress tensor we sum over all the collision events in the time interval τ between all pairs of particles. Therefore in collision time dynamics we get the following expression for the stress tensor,

$$\mathcal{A}\sigma_{\alpha\beta} = -N k_B T \delta_{\alpha\beta} + \lim_{\tau \to \infty} \frac{1}{\tau} \sum_{\tau_c} \sum_{i<j} \Delta p_{ij}^\alpha x_{ij}^\beta , \tag{6.4}$$

where $\sum_{\tau_c}$ denotes a summation over all collisions in time τ.

6.2 Analysis of Qualitative Features

We briefly outline a derivation of the expression for the heat flux. For the special case of a hard disk system this simplifies somewhat. We will show that starting from this expression and making rather simple minded approximations we can explain some of the observed results for heat flux as a function of imposed external strain.

We consider a system with a general Hamiltonian given by:

$$H = \sum_i [\frac{m\mathbf{u}_i^2}{2} + V(\mathbf{r}_i)] + \frac{1}{2}\sum_{i,j\neq i}\phi(r_{ij}) , \qquad (6.5)$$

where $V(\mathbf{r}_i)$ is an onsite potential which also includes the wall. To define the heat current density we need to write a continuity equation of the form: $\partial\epsilon(\mathbf{r},t)/\partial t + \partial j_\alpha(\mathbf{r},t)/\partial x_\alpha = 0$. The local energy density is given by:

$$\epsilon(\mathbf{r}, t) = \sum_i \delta(\mathbf{r} - \mathbf{r}_i)h_i \quad \text{where}$$

$$h_i = \frac{m\mathbf{u}_i^2}{2} + V(\mathbf{r}_i) + \frac{1}{2}\sum_{j\neq i}\phi(r_{ij})$$

Taking a derivative with respect to time gives

$$\frac{\partial\epsilon}{\partial t} = -\frac{\partial}{\partial x_\alpha}\sum_i \delta(\mathbf{r} - \mathbf{r}_i)h_i u_i^\alpha + \sum_i \delta(\mathbf{r} - \mathbf{r}_i)\dot{h}_i \qquad (6.6)$$

$$= -\frac{\partial}{\partial x^\alpha}j_\alpha^K + W^U \qquad (6.7)$$

where $\mathbf{j}^K = \sum_i \delta(\mathbf{r} - \mathbf{r}_i)h_i\mathbf{u}_i$ is the convective part of the energy current. We will now try to write the remaining part given by W^U as a divergence term. We have

$$W^U = \sum_i \delta(\mathbf{r} - \mathbf{r}_i)\dot{h}_i$$

$$= \sum_i \delta(\mathbf{r} - \mathbf{r}_i)[mu_i^\alpha \dot{u}_i^\alpha + \frac{\partial V(\mathbf{r}_i)}{\partial x_i^\alpha}u_i^\alpha$$

$$- \frac{1}{2}\sum_{j\neq i}(f_{ij}^\alpha u_i^\alpha + f_{ji}^\alpha u_j^\alpha)] ,$$

where $f_{ij}^\alpha = -\partial\phi(r_{ij})/\partial x_i^\alpha$. Using the equation of motion $m\dot{u}_i^\alpha = -\partial V/\partial x_i^\alpha + \sum_{j\neq i}f_{ij}^\alpha$ we get

$$W^U = \frac{1}{2}\sum_{i,j\neq i}\delta(\mathbf{r} - \mathbf{r}_i)(\ f_{ij}^\alpha u_i^\alpha - f_{ji}^\alpha u_j^\alpha\ ) . \qquad (6.8)$$

With the identification $W^U = -\partial j_\alpha^U / \partial x^\alpha$ and using $\mathbf{f}_{ij} = -\mathbf{f}_{ji}$ we finally get:

$$j_\alpha^U(\mathbf{r}) = \frac{1}{2} \sum_{i,j \neq i} \theta(x_i^\alpha - x^\alpha) \prod_{\nu \neq \alpha} \delta(x^\nu - x_i^\nu) f_{ij}^\beta (u_i^\beta + u_j^\beta) \tag{6.9}$$

where $\theta(x)$ is the Heaviside step function. This formula has a simple physical interpretation. First note that we need to sum over only those i for which $x_i^\alpha > x^\alpha$. Then the formula basically gives us the net rate at which work is done by particles on the left of x^α on the particles on the right which is thus the rate at which energy flows from left to right. The other part, j_α^K, gives the energy flow as a result of physical motion of particles across x^α. Let us look at the total current in the system. Integrating the current density j_α^U over all space we get:

$$
\begin{aligned}
I_\alpha^U &= \frac{1}{2} \sum_{i,j \neq i} x_i^\alpha f_{ij}^\beta (u_i^\beta + u_j^\beta) \\
&= -\frac{1}{2} \sum_{i,j \neq i} x_i^\alpha \frac{\partial \phi(r_{ij})}{\partial r_{ij}} \frac{x_{ij}^\beta}{r_{ij}} (u_i^\beta + u_j^\beta) \\
&= -\frac{1}{4} \sum_{i,j \neq i} \frac{\partial \phi(r_{ij})}{\partial r_{ij}} \frac{x_{ij}^\alpha x_{ij}^\beta}{r_{ij}} (u_i^\beta + u_j^\beta) \, .
\end{aligned}
\tag{6.10}
$$

Including the convective part and taking an average over the steady state we finally get:

$$
\begin{aligned}
\langle I_\alpha \rangle &= \langle I_\alpha^K \rangle + \langle I_\alpha^U \rangle = \sum_i \langle\, h_i u_i^\alpha \rangle \\
&\quad - \frac{1}{4} \sum_{i,j \neq i} \langle\, \frac{\partial \phi(r_{ij})}{\partial r_{ij}} \frac{x_{ij}^\alpha x_{ij}^\beta}{r_{ij}} (u_i^\beta + u_j^\beta) \,\rangle \, .
\end{aligned}
\tag{6.11}
$$

We note that for a general phase space variable $A(\{x_i, u_i\})$ the average $\langle A \rangle$ is the time average $\lim_{\tau \to \infty} (1/\tau) \int_0^\tau dt A(\{x_i(t), u_i(t)\})$.

Finding the energy current for hard disk system: The energy current expression involves the velocities of the colliding particles which change during a collision so we have to be careful. We use the following expression for $\langle I_\alpha^U \rangle$:

$$
\begin{aligned}
\langle\, I_\alpha^U \,\rangle &= \frac{1}{4} \sum_{i,j \neq i} \langle\, x_{ij}^\alpha (f_{ij}^\beta u_i^\beta - f_{ji}^\beta u_j^\beta) \,\rangle \\
&= \lim_{\tau \to \infty} \frac{1}{\tau} \int_0^\tau dt \frac{1}{4} \sum_{i,j \neq i} x_{ij}^\alpha (f_{ij}^\beta u_i^\beta - f_{ji}^\beta u_j^\beta)
\end{aligned}
\tag{6.12}
$$

Now if we integrate across a collision we see that $\int dt (\mathbf{f}_{ij} . \mathbf{u}_i)$ gives the change in kinetic energy of the ith particle during the collision while $\int dt (\mathbf{f}_{ji} . \mathbf{u}_j)$ gives the change in kinetic energy of the

j^{th} particle. Hence we get

$$
\begin{aligned}
\langle\, I_\alpha^U \,\rangle &= \sum_{i,j\neq i} \lim_{\tau\to\infty} \frac{1}{\tau} \sum_{t_c} \frac{1}{4} x_{ij}^\alpha (\Delta K_i - \Delta K_j) \\
&= \sum_{i<j} \frac{\langle\, x_{ij}^\alpha \Delta K_i \,\rangle_c}{\langle\, \tau_{ij} \,\rangle_c}
\end{aligned} \tag{6.13}
$$

where we have used the fact that for elastic collisions $\Delta K_i = -\Delta K_j$ and $\sum_{t_c}$ denotes a summation over all collisions, in the time interval τ, between pairs $\{ij\}$. The time interval between successive collisions between i^{th} and j^{th} particles is denoted by τ_{ij} and the average $\langle\,...\,\rangle_c$ in the last line denotes a *collisional* average. Thus $\langle\tau_{ij}\rangle_c = \lim_{\tau\to\infty} \tau/N_{ij}(\tau)$, where $N_{ij}(\tau)$ is the number of collisions between i^{th} and j^{th} particles in time τ. For hard spheres the convective part of the current involves only the kinetic energy and is given by $\langle\, I_\alpha^K \,\rangle = \sum_i \langle\, (m\mathbf{u}_i^2/2)u_i^\alpha \,\rangle$. Using these expressions we now try to obtain estimates of the heat current and its dependence on strain in the close packed limit where the system looks like a solid with the structure of a strained triangular lattice.

In the close packed limit the convection current can be neglected and we focus only on the conductive part given by $\langle I^U \rangle = \langle I_2^U \rangle$ (for conduction along the $y-$direction). At this point we assume local thermal equilibrium (LTE) which we prove from our simulation data at the end of this section. Assuming LTE we write the following approximate form for the energy change ΔK_i during a collision:

$$
\Delta K_i = k_B(T(y_j) - T(y_i)) = -k_B \frac{dT}{dy} y_{ij} = y_{ij} \frac{k_B \Delta T}{L_y} \ ,
$$

where we have denoted $x_i^{(\alpha=2)} = y_i$ and $\Delta T = T_1 - T_2$. The temperature gradient has been assumed to be small and constant. Further we assume that in the close packed limit that we are considering, only nearest neighbor pairs $\{<ij>\}$ contribute to the current in Eq. (6.13) and that they contribute equally. We then get the following approximate form for the total current:

$$
\langle I_y \rangle \approx \frac{3N k_B \Delta T}{L_y} \frac{y_c^2}{\tau_c} \ , \tag{6.14}
$$

where τ_c is the average time between successive collisions between two particles while y_c^2 is the mean square separation along the $y-$axis of the colliding particles. Finally, denoting the density of particles by $\rho = N/\mathcal{A}$ we get for the current density:

$$
j_y = \frac{\langle I_y \rangle}{\mathcal{A}} \approx \frac{3\rho k_B \Delta T}{L_y} \frac{y_c^2}{\tau_c} \ . \tag{6.15}
$$

For strains ϵ_{xx} and ϵ_{yy} in the x and y directions we have $\rho = \rho_0/[(1 + \epsilon_{xx})\,(1 + \epsilon_{yy})]$. We estimate y_c^2 and τ_c from a simple equilibrium free-volume theory, known as fixed neighbour free
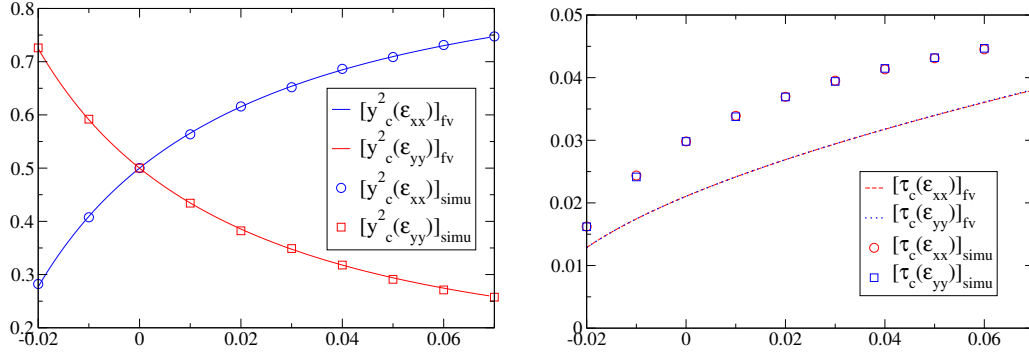
FIGURE 6.8: Plots showing comparision of the analytically calculated values of $[y_c^2]_{fv}$ and $[\tau_c]_{fv}$ with those obtained from a free volume simulation of a single disk moving within the free volume cage. The free volume corresponds to a starting unstrained triangular lattice at $\eta = 0.85$ which is then strained along x or y directions.

volume theory (FNFVT) [See Sec.5.3 of chapter-5]. In this picture we think of a single disk moving in a fixed cage formed by taking the average positions of its six nearest neighbor disks [see Fig.5.10]. For different values of the strains we then evaluate the average values $[y_c^2]_{fv}$ and $[\tau_c]_{fv}$ for the moving particle from FNFVT. We assume that the position of the center of the moving disk $P_0(x, y)$, at the time of collision with any one of the six fixed disks, is uniformly distributed on the boundary $\mathcal{B}$ of the free-volume. Hence $[y_c^2]_{fv}$ is easily calculated using the expression:

$$[y_c^2]_{fv} = \frac{\sum_i \int_{\mathcal{B}_i} ds(y - y_i)^2}{L_{\mathcal{B}}} \ , \tag{6.16}$$

where $\mathcal{B}_i$ is the part of the boundary $\mathcal{B}$ of the free volume when the middle disk is in contact with the ith fixed disk, ds is the infintesimal length element on $\mathcal{B}$ while $L_{\mathcal{B}}$ is the total length of $\mathcal{B}$. Let the unstrained lattice parameters be a_x^0, $a_y^0 = \sqrt{3}a_x^0/2$. Under strain we have $a_x = a_x^0(1 + \epsilon_{xx})$ and $a_y = a_y^0(1 + \epsilon_{yy})$. Using elementary geometry we can then evaluate $[y_c^2]_{fv}$ from Eq. (6.16) in terms of ϵ_{xx}, ϵ_{yy} and the unstrained lattice parameter a_x^0. An exact calculation of $[\tau_c]_{fv}$ is nontrivial. However we expect $[\tau_c]_{fv} = c \, V_{fv}^{1/2}/T^{1/2}$ where V_{fv} is the "free volume" [see Fig. 5.10] and c is a constant factor of $O(1)$ which we will use as a fitting parameter. The calculated values for $[y_c^2]_{fv}$ and $[\tau_c]_{fv}$ are shown in Fig. 6.8. Also shown are their values obtained from an equilibrium simulation of a single disk moving inside the free volume cage. Thus we obtain the following estimate for the heat current:

$$[j_y]_{fv} = \frac{3\rho k_B T^{1/2} \Delta T}{L_y} \frac{[y_c^2]_{fv}}{c \, V_{fv}^{1/2}} \ . \tag{6.17}$$

We plot in Fig. (6.3,6.5) the above estimate of $[j_y]_{fv}$ along with the results from simulations. We find that the overall features of the simulation are reproduced with $c = 0.42$.
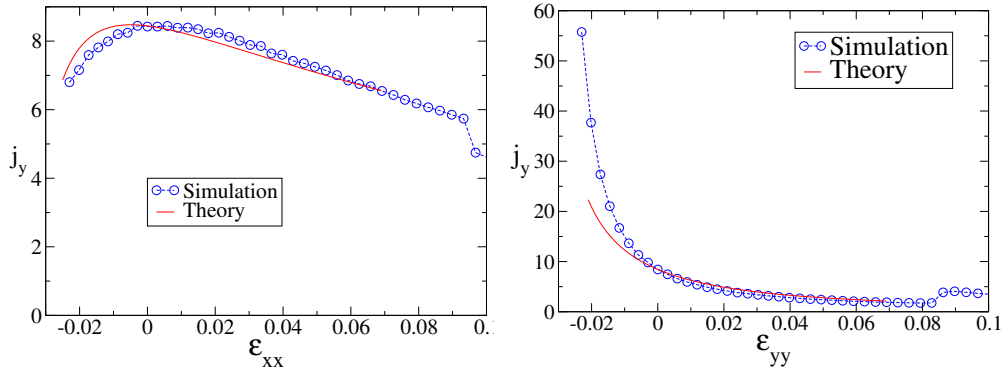
FIGURE 6.9: Plot showing effect on j_y of negative strains applied in the x and y directions. The system is prepared initially in a triangular lattice at $\eta = 0.85$. Note that negative ϵ_{xx} reduces j_y whereas negative ϵ_{yy} increases j_y.
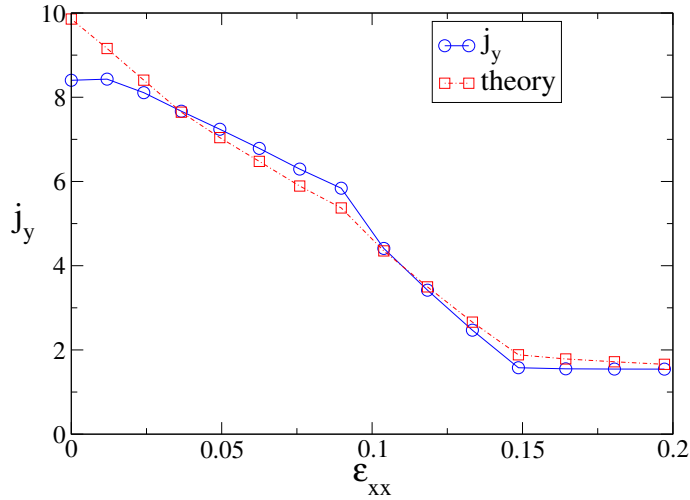
FIGURE 6.10: Comparison of simulation results for j_y with the approximate formula in Eq. (6.15) where τ_c and y_c^2 are also calculated directly from the same simulation. The results are for a 40×10 system with starting value of $\eta = 0.85$ and strained along $x-$direction.

For small strain $[y_c^2(\epsilon_{xx})]_{fv} \sim 0.5 + \alpha\epsilon_{xx} - \beta_1\epsilon_{xx}^2$, $[y_c^2(\epsilon_{yy})]_{fv} \sim 0.5 - \alpha\epsilon_{yy} + \beta_2\epsilon_{yy}^2$ and $[\tau_c]_{fv} \sim (\gamma_1 + \gamma_2\epsilon - \gamma_3\epsilon^2)$ where ϵ stands for either ϵ_{xx} or ϵ_{yy} and α, β_1, β_2, $\gamma_1, \gamma_2, \gamma_3$ are all positive constants that depend only on a_x^0 (we do not write them explicitly since the expressions are messy and unilluminating). For $\eta = 0.85$ we have $\alpha = 7.62$, $\beta_1 = 121.77$, $\beta_2 = 124.37$ and $\gamma_1 = 0.02$, $\gamma_2 = 0.33$, $\gamma_3 = 1.125$. From these small strain scaling forms we find that $j_y(\epsilon_{yy})$ always decreases with positive ϵ_{yy} and increases with negative or compressive ϵ_{yy} (note that
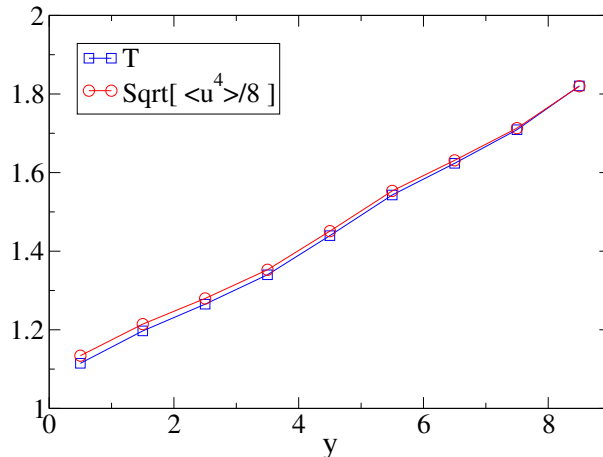
FIGURE 6.11: Plot of temperature profile and fourth moment of velocity for a strained 40×10 lattice. The unstrained packing fraction was $\eta = 0.85$ and the system was strained to $\epsilon_{xx} = 0.0625$.

we always consider starting configurations of a triangular solid of any density). On the other hand the sign of the change in $j_y(\epsilon_{xx})$ will depend on the relative magnitudes of α, β_1 and γ. For starting density $\eta = 0.85$, $j_y(\epsilon_{xx})$ decreases both for positive and negative ϵ_{xx}. In Fig. 6.9 we show the effect of compressive strains ϵ_{xx} and ϵ_{yy} on the heat current j_y and compare the simulation results with the free volume theory.

It is possible to calculate y_c^2 and τ_c directly from our nonequilibrium collision time dynamics simulation. The mean collision time τ_c is obtained by dividing the total simulation time by the total number of collisions per colliding pair. Similarly y_c^2 is evaluated at every collision and we then obtain its average. Inserting these values of τ_c and $\langle y_c^2 \rangle$ into the right hand side of Eq. (6.15) we get an estimate of the current as given by our theory (without making use of free-volume theory). In Fig. 6.10 we compare this value of the current j_y, for strain $\epsilon = \epsilon_{xx}$, and compare it with the simulation results. The excellent agreement between the two indicates that our simple theory is quite accurate.

We have also tested the assumptions of a linear temperature profile and the assumption of local thermal equilibrium (LTE) that we have used in our theory. In our simulations the local temperature is defined from the local kinetic energy density, *i.e.* $k_B T = \langle m\vec{u}^2/2 \rangle$. Local thermal equilibrium requires a close to Gaussian distribution of the local velocity with a width given by the same temperarture. The assumption of LTE can thus be tested by looking at higher moments of the velocity, evaluated locally. Thus we should have $\langle \vec{u}^4 \rangle = 8(k_B T/m)^2$. From our simulation we find out $\langle \vec{u}^4(y) \rangle$ and $k_B T(y)$ as functions of the distance y from the cold to hot reservoir. The plot in Fig. 6.11 shows that the temperature profile is appoximately linear and LTE is approximately valid. We use our theory only in the solid phase and in this case there is
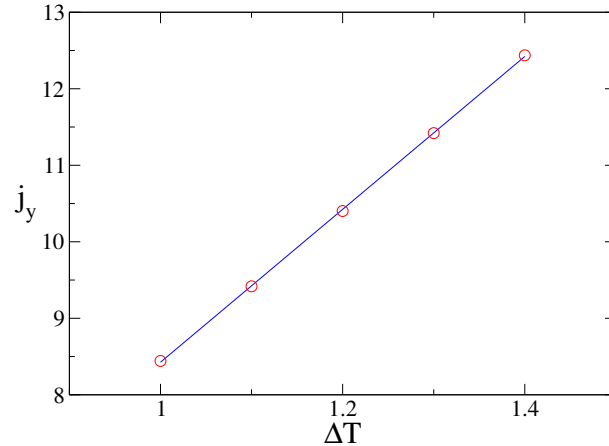
FIGURE 6.12: Plot of j_y versus $\Delta T = T_2 - T_1$ for a 40×10 triangular lattice at $\eta = 0.85$. We see that the current increases linearly with the applied gradient.

not much variation in the direction transverse to heat flow ($x-$direction).

Finally we find that the heat conduction in the small confined lattice under small strains shows a linear response behaviour. This can be seen in Fig. 6.12 where we plot j_y versus $\Delta T = T_2 - T_1$ for a 40×10 triangular lattice at $\eta = 0.85$. Note that, as mentioned in the introduction, the bulk thermal conductivity of a two-dimensional system is expected to be divergent and the linear response behaviour observed here is only relevant for a finite system in certain regimes (solid under small strains).

6.3 Summary and Conclusion

In this chapter we have studied heat conduction in a two-dimensional solid formed from hard disks confined in a narrow structureless channel. The channel has a small width (~ 10 particle layers) and is long (~ 100 particles). Thus our system is in the nanoscale regime. We have shown that structural changes that occur when this solid is strained can lead to sudden jumps in the heat current.   From the system sizes that we have studied it is not possible to conclude that these jumps will persist in the limit that the channel length becomes infinite. However the finite size results are interesting and relevant since real nano-sized solids *are* small. We have also proposed a free volume theory type calculation of the heat current. While being heuristic it gives correct order of magnitude estimates and also reproduces qualitative trends in the current-strain graph. This simple approach should be useful in calculating the heat conductivity of a hard sphere solid in the high density limit.

The property of large change of heat current could be utilized to make a system perform as a mechanically controlled switch of heat current. Similar results are also expected for the electrical

conductance and this is shown to be true at least following one protocol of straining in Ref.[167]. From this point of view it seems worthwhile to perform similar studies on transport in confined nano-systems in three dimensions and also with different interparticle interactions.

Index

References

[1] R. B. Griffiths, in *Phase Transitions and Critical Phenomena*, edited by C. Domb and M. S. Green (Academic Press, New York, 1972), Vol. 1, p. 7.

[2] M. E. Fisher, Rev. Mod. Phys. **46**, 597 (1974).

[3] M. E. Fisher, Rev. Mod. Phys. **70**, 653 (1998).

[4] H. E. Stanley, Rev. Mod. Phys. **71**, S358 (1999).

[5] K. Binder, Phys. Rev. Lett. **47**, 693 (1981).

[6] K. Binder, Rep. Prog. Phys. **50**, 783 (1987).

[7] K. G. Wilson and M. E. Fisher, Phys. Rev. Lett. **28**, 240 (1972).

[8] M. E. Fisher and M. N. Barber, Phys. Rev. Lett. **28**, 1516 (1972).

[9] M. E. Fisher and A. Aharony, Phys. Rev. Lett. **31**, 1537 (1973).

[10] D. R. Nelson, J. M. Kosterlitz, and M. E. Fisher, Phys. Rev. Lett. **33**, 813 (1974).

[11] K. G. Wilson and J. Kogut, Phys. Rep. **12C**, 75 (1974).

[12] N. Goldenfeld, *Lectures on Phase Transitions and the Renormalization Group* (Perseus Publishing, ADDRESS, 1992).

[13] A. P. Sutton and R. W. Balluffi, *Interfaces in crystalline materials* (Oxford Science Pub., New York, 1995).

[14] S. A. Safran, *Statistical Thermodynamics of Surfaces. Interfaces, and Membranes* (Addison Wesley, MA, 1994).

[15] A. Ott, M. Magnasco, A. Simon, and A. Libchaber, Phys. Rev. E **48**, R1642 (1993).

[16] F. Gittes, B. Mickey, J. Nettleton, and J. Howard, J. Cell Biol **120**, 923 (1993).

[17] B. Alberts *et al.*, *Molecular Biology of The Cell*, 4th ed. (Garland Science, Taylor and Francis Group, New York, 2002).

[18] C. Bustamante, Z. Bryant, and S. B. Smith, Nature **42**, 423 (2003).

[19] C. Bustamante, Z. Bryant, and S. B. Smith, Nat. Rev. Mol. Cell Biol. **1**, 130 (2000).

[20] V. Balzani, M. Venturi, and A. Credi, *Molecular devices and machines: a journey into the nano world* (Wiley-VCH, Weinhem, 2003).

[21] M. Doi and S. F. Edwards, *The theory of Polymer Dynamics* (Clarendon, Oxford, 1992).

[22] N. Saito, K. Takahashi, and Y. Yunoki, J. Phys. Soc. Japan **22**, 219 (1967).

[23] E. Frey, K. Kroy, J. Wilhelm, and E. Sackmann, (1997), arXiv:cond-mat/9707021.

[24] H. J. Kreuzer and S. H. Payne, Phys. Rev. E **63**, 021906 (2001).

[25] J. F. Marko and E. D. Siggia, Macromolecules **28**, 8759 (1995).

[26] S. B. Smith, L. Finzi, and C. Bustamante, Science **258**, 1122 (1992).

[27] H. E. Daniels, Proc. Roy. Soc. Edinb. **63A**, 290 (1952).

[28] W. Gobush, H. Yamakawa, W. H. Stockmayer, and W. S. Magee, J. Chem. Phys. **57**, 2839 (1972).

[29] T. Norisuye, H. Murakama, and H. Fujita, Macromolecules **11**, 966 (1978).

[30] J. Wilhelm and E. Frey, Phys. Rev. Lett. **77**, 2581 (1996).

[31] D. Thirumalai and B. Y. Ha, J. Chem. Phys. **103**, 9408 (1995), condmat/9705200/.

[32] J. J. Hermans and R. Ullman, Physica **18**, 951 (1952).

[33] J.-C. Meiners and S. R. Quake, Phys. Rev. Lett. **84**, 5014 (2000).

[34] M. Geanacopoulos, G. Vasmatzis, V. B. Zhurkin, and S. Adhya, Nat. Struct. Biol. **8**, 432 (2001).

[35] J. Plumbridge and A. Kolb, Nucleic Acids Res. **26**, 1254 (1998).

[36] M. Brenowitz, A. Pickar, and E. Jamison, Biochemistry **30**, 5986 (1991).

[37] C. Bustamante, S. B. Smith, J. Liphardt, and D. Smith, Curr. Opin. Struct. Biol. **10**, 279 (2000).

[38] C. Gosse and V. Croquette, Biophysical Journal **82**, 3314 (2002).

[39] M. Rief, F. Oesterhelt, B. Heymann, and H. E. Gaub, Science **275**, 1295 (1997).

[40] S. Sinha and J. Samuel, Phys. Rev. E **71**, 021104 (2005).

[41] J. Samuel and S. Sinha, Phys. Rev. E **66**, 050801(R) (2002), arXiv:cond-mat/0203483/.

[42] A. Dhar and D. Chaudhuri, Phys. Rev. Lett. **89**, 065502 (2002).

[43] G. Lattanzi, T. Munk, and E. Frey, Phys. Rev. E **69**, 021801 (2004).

[44] O. Kratky and G. Porod, Rec. Trav. Chim. **68**, 1106 (1949).

[45] C. Bustamante, J. F. Marko, E. D. Siggia, and S. Smith, Science **265**, 1599 (1994).

[46] M. Rief, M. Gautel, F. Westerhelt, and J. M. Fernandez, Science **276**, 1109 (1997).

[47] M. Rief, J. M. Fernandez, and H. E. Gaub, Phys. Rev. Lett. **81**, 4764 (1998).

[48] H. Li, M. Rief, F. Westerhelt, and H. E. Gaub, Applied Physics A **68**, 407 (1999).

[49] J. K. Bhattacharjee, D. Thirumalai, and J. D. Bryngelson, , cond-mat/9709345.

[50] B. Hamprecht, W. Janke, and H. Kleinert, , cond-mat/0307530.

[51] B. Hamprecht and H. Kleinert, Phys. Rev. E **71**, 031803 (2005).

[52] S. A. Stepanow, The European Physical Journal B-Condensed Matter **39**, 499 (2004).

[53] K. Kroy and E. Frey, Phys. Rev. Lett. **77**, 306 (1996).

[54] P. Benetatos, T. Munk, and E. Frey, Phys. Rev. E **72**, 030801(R) (2005).

[55] A. J. Spakowitz and Z.-G. Wang, Phys. Rev. E **72**, 041802 (2005).

[56] P. Ranjith, P. B. S. Kumar, and G. I. Menon, Phys. Rev. Lett. **94**, 138102 (2005).

[57] J. F. Marko and E. D. Siggia, Macromolecules **27**, 981 (1994).

[58] C. Bouchiat and M. Mezard, Phys. Rev. Lett. **80**, 1556 (1998).

[59] S. Panyukov and Y. Rabin, Phys. Rev. Lett. **85**, 2404 (2000).

[60] S. Wolfram, *The Mathematica Book*, 3rd ed. (Wolfram media, Cambridge, 1996).

[61] J. M. Kosterlitz and Thouless, J. Phys. C **6**, 1181 (1973).

[62] D. R. Nelson and B. I. Halperin, Phys. Rev. B **19**, 2457 (1979).

[63] A. P. Young, Phys. Rev. B **19**, 1855 (1979).

[64] J. Tobochnik and G. V. Chester, Phys. Rev. B **20**, 3761 (1979).

[65] J. Fernández, M. F. Ferreira, and J. Stankiewicz, Phys. Rev. B **34**, 292 (1986).

[66] R. Gupta, J. DeLapp, and G. G. Batrouni, Phys. Rev. Lett. **61**, 1996 (1988).

[67] P. Minnhagen, Rev. Mod. Phys. **59**, 1001 (1987).

[68] S. Sengupta, P. Nielaba, and K. Binder, Europhys. Lett. **50**, 668 (2000).

[69] R. H. Morf, Phys. Rev. Lett. **43**, 931 (1979).

[70] K. J. Strandburg, Rev. Mod. Phys. **60**, 161 (1988).

[71] S. Sengupta, P. Nielaba, and K. Binder, Phys. Rev. E **61**, 6294 (2000).

[72] M. S. Rzchowski, S. P. Benz, M. Tinkham, and C. J. Lobb, Phys. Rev. B **42**, 2041 (1990).

[73] S. N. Coppersmith *et al.*, Phys. Rev. Lett. **46**, 549 (1981).

[74] A. Chowdhury, B. J. Ackerson, and N. A. Clark, Phys. Rev. Lett. **55**, 833 (1985).

[75] Q.-H. Wei, C. Bechinger, D. Rudhardt, and P. Leiderer, Phys. Rev. Lett. **81**, 2606 (1998).

[76] F. Huang, M. T. Kief, G. J. Mankey, and R. F. Willis, Phys. Rev. B **49**, 3962 (1994).

[77] W. Dürr *et al.*, Phys. Rev. Lett. **62**, 206 (1989).

[78] *Ordering in Two Dimensions*, edited by S. K. Sinha (North-Holland, Amsterdam, 1980).

[79] K. J. Strandburg, Phys. Rev. B **34**, 3536 (1986).

[80] D. R. Nelson, in *Phase Transitions and Critical Phenomena*, edited by C. Domb and J. Lebowitz (Academic Press, New York, 1983), Vol. 7, p. 1.

[81] M. S. S. Challa and D. P. Landau, Phys. Rev. B **33**, 437 (1986).

[82] A. Zippelius, B. I. Halperin, and D. R. Nelson, Phys. Rev. B **22**, 2514 (1980).

[83] D. Chaudhuri and S. Sengupta, Europhys. Lett. **67**, 814 (2004).

[84] D. Chaudhuri and S. Sengupta, Europhys. Lett. **68**, 160 (2004).

[85] J. Chakraborti, H. R. Krishnamurthy, A. K. Sood, and S. Sengupta, Phys. Rev. Lett. **75**, 2232 (1995).

[86] C. Das and H. R. Krishnamurthy, Phys. Rev. B **58**, R5889 (1998).

[87] C. Das, A. K. Sood, and H. R. Krishnamurthy, Physica **A 270**, 237 (1999).

[88] C. Das, P. Chaudhuri, A. K. Sood, and H. R. Krishnamurthy, Current Science **80**, 959 (2001).

[89] W. Strepp, S. Sengupta, and P. Nielaba, Phys. Rev. E **63**, 046106 (2001).

[90] W. Strepp, S. Sengupta, and P. Nielaba, Phys. Rev. E **66**, 056109 (2002).

[91] W. Strepp, S. Sengupta, M. Lohrer, and P. Nielaba, Computer Physics Communications **147**, 370 (2002).

[92] W. Strepp, S. Sengupta, M. Lohrer, and P. Nielaba, Mathematics and Computers in Simulation **62**, 519 (2003).

[93] J. Chakraborti, H. R. Krishnamurthy, and A. K. Sood, Phys. Rev. Lett. **73**, 2923 (1994).

[94] E. Frey, D. R. Nelson, and L. Radzihovsky, Phys. Rev. Lett. **83**, 2977 (1999).

[95] L. Radzihovsky, E. Frey, and D. R. Nelson, Phys. Rev. E **63**, 031503 (2000).

[96] I. W. Hamley, *Introduction to Soft Matter: polymer, colloids, amphiphiles and liquid crystals* (Wiley, Cluchester, 2000).

[97] D. P. Landau and K. Binder, *A Guide to Monte Carlo Simulations in Statistical Physics* (Cambridge University Press,, Cambridge, UK, 2000).

[98] D. S. Fisher, B. I. Halperin, and R. Morf, Phys. Rev. B **20**, 4692 (1979).

[99] A. Jaster, Physica A **277**, 106 (2000).

[100] D. J. Amit, Y. Y. Goldschmidt, and G. Grinstein, J. Phys. A: Math. Gen. **13**, 585 (1980).

[101] H. A. Kramers, Physica **7**, 284 (1940).

[102] O. Farago and Y. Kantor, Phys. Rev. E **61**, 2478 (2000).

[103] E. J. W. Verwey and Overbeek, *Theory of Stability of Lyophobic Colloids* (Elsevier, Netherlands, 1948).

[104] Derjaguin, B. V., Landau, and L. D., Acta Phys. Chim., USSR **14**, 633 (1941).

[105] B. Alder and T. Wainwright, Phys. Rev. **127**, 359 (1962).

[106] J. Zollweg, G. Chester, and P. Leung, Phys. Rev. B **39**, 9518 (1989).

[107] H. Weber and D. Marx, Europhys. Lett. **27**, 593 (1994).

[108] V. Ryzhov and E. Tareyeva, Phys. Rev. B **51**, 8789 (1995).

[109] J. P. Hansen and I. R. MacDonald, *Theory of simple liquids* (Wiley, Cluchester, 1989).

[110] D. Frenkel and B. Smith, *Understanding Molecular Simulation*, 2nd ed. (Academic Press, New York, 2002).

[111] http://www.pi6.fernuni-hagen.de/GeomLab/VoroGlide/index.html.en .

[112] C. Bechinger and E. Frey, J. Phys.: Condens. Matter **13**, R321 (2001).

[113] R. Giao *et al.*, Phys. Rev. Lett. **85**, 622 (2000).

[114] A. N. Cleland and M. L. Roukes, Appl. Phys. Lett. **69**, 2653 (1996).

[115] I. Goldhirsh and C. Goldenberg, European Physical Journal **E 9**, 245 (2002).

[116] P. Pieranski, L. Strzelecki, and B. Pansu, Phys. Rev. Lett. **50**, 900 (1983).

[117] S. Neser, C. Bechinger, and P. Leiderer, Phys. Rev. Lett. **79**, 2348 (1997).

[118] M. Schmidt and H. Lowen, Phys. Rev. Lett. **76**, 4552 (1996).

[119] T. Chou and D. R. Nelson, Phys. Rev. E **48**, 4611 (1993).

[120] M. Schmidt and H. Lowen, Phys. Rev. E **55**, 7228 (1997).

[121] A. Fortini and M. Dijkstra, , cond-mat/0604169.

[122] R. P. A. Dullens and W. K. Kegel, Phys. Rev. Lett. **92**, 195702 (2004).

[123] G. Piacente, I. V. Schweigert, J. J. Betouras, and F. M. Peeters, Phys. Rev. B **69**, 045324 (2004).

[124] R. Haghgooie and P. S. Doyle, Phys. Rev. B **70**, 061408 (2004).

[125] R. Haghgooie and P. S. Doyle, Phys. Rev. E **72**, 011405 (2005).

[126] P.-S. T. L.-W. Teng and L. I, Phys. Rev. Lett. **90**, 245004 (2003).

[127] V. M. Bedanov and F. M. Peeters, Phys. Rev. B **49**, 2667 (1994).

[128] R. Bubeck, C. Bechinger, S. Neser, and P. Leiderer, Phys. Rev. Lett. **82**, 3364 (1999).

[129] Y.-J. Lai and L. I, Phys. Rev. E **64**, 015601 (2001).

[130] R. Bubeck, P. Leiderer, and C. Bechinger, Europhys. Lett. **60**, 474 (2002).

[131] M. Kong, B. Partoens, and F. M. Peeters, Phys. Rev. E **67**, 021608 (2003).

[132] P. G. de Gennes, Langmuir **6**, 1448 (1990).

[133] J. Gao, W. D. Luedtke, and U. Landman, Phys. Rev. Lett. **79**, 705 (1997).

[134] P. Pieranski, J. Malecki, and K. Wojciechowski, Molecular Physics **40**, 225 (1980).

[135] R. A. McMillan *et al.*, Nature Materials **1**, 247 (2002).

[136] K. W. Wojciechowski and A. C. Brańka, Phys. Lett. A **134**, 314 (1988).

[137] M. Heni and H. Löwen, Phys. Rev. E **60**, 7057 (1999).

[138] A. A. Griffith, Philos. Trans. Roy. Soc. **A 221**, 163 (1920).

[139] J. A. Hauch, D. Holland, M. P. Marder, and H. L. Swinney, Phys. Rev. Lett. **82**, 3823 (1999).

[140] D. Holland and M. Marder, Phys. Rev. Lett. **80**, 746 (1998).

[141] J. S. Langer, Phys. Rev. E **62**, 1351 (2000).

[142] R. Lofstedt, Phys. Rev. E **55**, 6726 (1997).

[143] T. B. *et. al.*, Phys. Rev. B **65**, 235430 (2002).

[144] M. F. Y. *et. al.*, Science **287**, 637 (2000).

[145] H. I. *et. al.*, Phys. Rev. Lett. **82**, 2900 (1999).

[146] P. S. Branicio and J.-P. Rino, Phys. Rev. B **62**, 16950 (2000).

[147] K. Zahn, R. Lenke, and G. Maret, Phys. Rev. Lett. **82**, 2721 (1999).

[148] P. M. Chaikin and T. C. Lubensky, *Principles of Condensed Matter Physics* (Cambridge University Press, Cambridge, 1995).

[149] J. S. Langer, in *Solids far from equilibrium*, edited by C. Godréche (Cambridge University Press, Cambridge, 1992), Vol. III, p. 169.

[150] T. Roopa and G. V. Shivashankar, Appl. Phys. Lett. **82**, 1631 (2003).

[151] T. V. Ramakrishnan and M. Youssuf, Phys. Rev. B **19**, 2775 (1979).

[152] D. Chaudhuri and S. Sengupta, Phys. Rev. Lett. **93**, 115702 (2004).

[153] D. Chaudhuri and S. Sengupta, Indian Journal of Physics **79**, 941 (2005).

[154] A. Santos, M. L. de Haro, and S. B. Yuste, J. Chem. Phys. **103**, 4622 (1995).

[155] A.Ricci, P.Nielaba, S.Sengupta, and K.Binder, in *COMPUTER SIMULATION STUDIES IN CONDENSED MATTER PHYSICS*, edited by D.P.Landau, S.P.Lewis, and H.B.Schuettler (Springer, Berlin-Heidelberg, 2006), Vol. XIX, in press.

[156] A. Ricci, P. Nielaba, S. Sengupta, and K. Binder, , personal communication.

[157] D. Chaudhuri and S. Sengupta, Phys. Rev. E **73**, 011507 (2006).

[158] A. Bid, A. Bora, and A. K. Raychaudhuri, Phys. Rev. B **72**, 113415 (2005).

[159] S. Datta, *Electronic transport in mesoscopic systems* (Cambridge University press, Cambridge, 1997).

[160] C. P. Poole and F. J. Owens, *Introduction to nanotechnology* (Wiley, New Jersey, 2003).

[161] F. Bonetto, J. Lebowitz, and L. Rey-Bellet, in *Mathematical Physics 2000*, edited by A. F. et al (Imperial College Pres, London, 2000), p. 128.

[162] S. Lepri, R. Livi, and A. Polit, Phys. Rep. **377**, 1 (2003).

[163] A. Lippi and R. Livi, J. Stat Phys. **100**, 1147 (2000).

[164] P. Grassberger and L. Yang, (2002), arXiv:cond-mat/0204247.

[165] M. P. Allen and D. J. Tildesley, *Computer Simulation of Liquids* (Oxford University Press, New York, 1987).

[166] D. Chaudhuri and S. Sengupta, in preparation (unpublished).

[167] S. Datta, D. Chaudhuri, T. Saha-Dasgupta, and S. Sengupta, Europhys. Lett. **73**, 765 (2006).